



HAL
open science

Conformation, morphology and self-assembly of colloidal semiconducting nanoplatelets

Lilian Guillemeney

► **To cite this version:**

Lilian Guillemeney. Conformation, morphology and self-assembly of colloidal semiconducting nanoplatelets. Materials. Université de Lyon, 2021. English. NNT : 2021LYSEN034 . tel-04213641

HAL Id: tel-04213641

<https://theses.hal.science/tel-04213641v1>

Submitted on 21 Sep 2023

HAL is a multi-disciplinary open access archive for the deposit and dissemination of scientific research documents, whether they are published or not. The documents may come from teaching and research institutions in France or abroad, or from public or private research centers.

L'archive ouverte pluridisciplinaire **HAL**, est destinée au dépôt et à la diffusion de documents scientifiques de niveau recherche, publiés ou non, émanant des établissements d'enseignement et de recherche français ou étrangers, des laboratoires publics ou privés.



Numéro National de Thèse : 2021LYSEN034

THÈSE de DOCTORAT DE L'UNIVERSITÉ DE LYON

opérée par

l'École Normale Supérieure de Lyon

École Doctorale N° 206

École Doctorale de Chimie (Chimie, Procédés, Environnement)

Discipline : Chimie

Soutenue publiquement le 06 juillet 2021, par :

Lilian GUILLEMENEY

Conformation, morphology and self-assembly of colloidal semiconducting nanoplatelets

*Conformation, morphologie et auto-assemblage
de nanoplaquettes semi-conductrices en solution colloïdale*

Devant le jury composé de :

ABÉCASSIS Benjamin	Chargé de recherche HDR	ENS de Lyon	Directeur de thèse
CARENCO Sophie	Chargée de recherche HDR	LCMCP Paris	Rapporteuse
DUGUET Étienne	Professeur des Universités	ICMCB Bordeaux	Président du jury
PAROLA Stéphane	Professeur des Universités	ENS de Lyon	Examineur
VIAU Guillaume	Professeur des Universités	INSA Toulouse	Rapporteur



Thesis

submitted for the degree of

DOCTOR OF THE UNIVERSITY OF LYON

issued by the

ÉCOLE NORMALE SUPÉRIEURE DE LYON

SPECIALITY : Chemistry

Conformation, morphology and self-assembly of colloidal semiconducting nanoplatelets

LILIAN GUILLEMENEY

*Laboratoire de Chimie de l'ENS de Lyon, UMR 5182
École Doctorale de Chimie de Lyon, ED n° 206*

Thesis supervised by: Dr. Benjamin ABÉCASSIS

To defend publicly on 6th July 2021 before the following committee:

Benjamin ABÉCASSIS	CNRS researcher	ENS de Lyon	PhD supervisor
Sophie CARENCO	CNRS researcher	LCMCP, Paris	Rapporteur
Etienne DUGUET	Professor	ICMCB, Bordeaux	Examiner
Stéphane PAROLA	Professor	ENS de Lyon	Examiner
Guillaume VIAU	Professor	INSA, Toulouse	Rapporteur

“ La science n’atteint jamais son but parce que le but n’en finit pas de se dérober - et qu’en vérité, il n’y a pas de but : la science est une tâche infinie. Sa grandeur est de se présenter comme un rêve toujours inassouvi.”

Jean d’Ormesson

Abstract

*** English version ***

We report in this thesis the morphological and conformational control of colloidal semiconducting nanoplatelets, as well as their self-assembly into larger superstructures. The first chapter describes important concepts about semiconducting nanomaterials from the literature.

We then present the shape-controlled solvothermal synthesis of γ - In_2S_3 nanomaterials. The geometry of these nanomaterials varies from hexagonal nanoplatelets to long nanoribbons. A very fine tuning of the lateral extension is achieved using a single experimental parameter. The composition, crystallographic structure and orientations of γ - In_2S_3 nanoribbons are investigated by Rutherford backscattering spectrometry, X-Ray photoelectron spectroscopy, X-Ray diffraction and high-angle annular dark field scanning transmission electron microscopy experiments. Their morphology and colloidal stability is investigated by transmission electron microscopy. We show that nanoribbons tend to form bundles in solution whose dimensions and aspect depend on the solvent. Besides, we suggest a growth mechanism for γ - In_2S_3 nanomaterials from time-resolved in-situ Small-Angle and Wide-Angle X-Ray Scattering experiments.

In a third chapter, we report the conformational control of initially coiled orthorhombic $Pnmm$ InS nanoplatelets. We determine by the same techniques as listed above their composition and their crystallographic structure and orientations. The uncoiling of the nanoplatelets is achieved by surface ligand exchange and their conformation is investigated by transmission electron microscopy.

Finally, we focus on the synthesis and the self-assembly of four- and five-monolayer CdSe nanoplatelets. Twisted threads of face-to-face distorted nanoplatelets are obtained and can reach several micrometers in length in the case of five-monolayer CdSe nanoplatelets assemblies. In collaboration with the Institut des nanosciences de Paris, we have evidenced by microphotoluminescence strong homo-FRET within self-assemblies of five-monolayer CdSe nanoplatelets, with an exciton migration over 500 nm (90 nanoplatelets).

*** French version ***

Cette thèse porte sur le contrôle de la conformation et de la morphologie de nanoplaquettes semi-conductrices en suspension colloïdale, ainsi que sur leur auto-assemblage en structures micrométriques. Le premier chapitre dresse un état de l'art sur les nanoplaquettes et décrit les principaux concepts associés.

Dans un second temps, nous présentons la synthèse par voie solvothermale de nanoplaquettes de γ - In_2S_3 . Les dimensions latérales de ces matériaux sont précisément contrôlées par la variation d'un unique paramètre expérimental, conduisant soit à la formation de nanoplaquettes hexagonales, soit à la formation de longs nanorubans. La composition, la structure et les orientations cristallographiques de ces objets sont déterminées par des expériences de rétrodiffusion d'ions, de spectroscopie de photoélectrons, de diffraction de rayons X et de microscopie à transmission électronique à haute-résolution. En outre, le mécanisme de croissance de ces objets est étudié par diffusion de rayons X aux petits et grands angles résolue en temps. Une étude sur la stabilité colloïdale des nanorubans dans différents solvants est menée. Nous montrons que dans la plupart des cas les nanorubans se regroupent en fagots, dont l'aspect et les dimensions dépendent du solvant de redispersion.

Nous décrivons ensuite le contrôle de la conformation de nanoplaquettes de InS orthorhombiques. A l'issue de leur synthèse, ces nanoplaquettes sont enroulées sur elles-mêmes. Nous élucidons leur composition, leur structure et orientations cristallographiques ainsi que leur chimie de surface par les mêmes techniques d'analyse que celles mentionnées précédemment. Leur rayon de courbure est déterminé par microscopie électronique à transmission. Nous montrons qu'un échange de ligand de surface permet le dépliement des nanoplaquettes.

Enfin, nous détaillons la synthèse et l'auto-assemblage de nanoplaquettes de CdSe de quatre et cinq monocouches d'épaisseur. Leurs assemblages se présentent sous la forme de long fils torsadés de nanoplaquettes distordues et alignées face-à-face, pouvant dépasser le micromètre dans le cas des assemblages de nanoplaquettes de cinq monocouches d'épaisseur. En collaboration avec l'Institut des Nanosciences de Paris, nous montrons par microscopie de fluorescence l'existence de homo-FRET au sein de ces derniers, avec une migration d'exciton sur 500 nm, soit entre 90 nanoplaquettes.

Acknowledgments

Avant d'entrer dans les détails scientifiques de mes travaux de thèse, j'aimerais adresser quelques mots de remerciements en français à toutes les personnes que j'ai eu le plaisir de côtoyer durant ces trois dernières années à l'ENS de Lyon, qui furent riches pour moi, tant humainement que scientifiquement.

Je pense en premier lieu à Benjamin Abécassis, que je souhaite remercier ici chaleureusement pour son encadrement précieux et sans faille, son soutien amical et ses conseils avisés apportés tout au long de ces trois dernières années. Je n'aurais pu rêver mieux comme conditions d'encadrement, qui m'ont toujours permis de trouver un parfait épanouissement scientifique, autour d'une thématique de recherche qui a toujours su attiser ma curiosité et susciter un grand intérêt en moi. Je suis donc plus que reconnaissant d'avoir pu effectuer mes travaux de recherche au sein de son équipe et suis heureux de pouvoir encore continuer quelques temps l'aventure avec elle après cette thèse.

Je remercie donc également tous ses membres, collègues de paillasse comme collègues de bureau, avec en premier lieu mes italiens favoris Chiara Moretti et Antonio Carone, qui ont toujours su apporter le soleil et la bonne humeur partout où ils étaient, aussi bien autour d'une synthèse de nanoparticules que d'un atelier de conception de gnocchis. Merci également à Austin Hubley, Benoit Wagnon, Guillaume Landaburu, Yige Yan, Adriaan Van der Bruinhorst, Fernando Lepré et Jocasta Avila avec lesquels j'ai eu le plaisir de partager de belles discussions scientifiques et amicales que ce soit au sein du même laboratoire ou bien de notre bureau commun.

Merci à Denis Chateau, Frédéric Chaput et Frédéric Lerouge pour leur aide précieuse et conseils scientifiques éclairés à la paillasse. C'est aussi le moment de remercier tous les membres de ce laboratoire, et notamment Delphine Pitrat et Jean-Christophe Mulatier, qui participent grandement au bon fonctionnement de ce laboratoire. Merci bien entendu à la direction du laboratoire, assurée par Chantal Andraud puis désormais Stéphane Parola : merci de leur soutien, de leur grande sympathie et sur le fait que l'on puisse toujours compter sur eux, tout comme sur Damien Séon et le pôle gestion.

Je souhaite ensuite remercier très particulièrement Sophie Carencu, Etienne Duguet, Stéphane Parola et Guillaume Viau qui m'ont fait l'honneur d'examiner mon travail et de participer à mon jury de thèse. Merci à Etienne Duguet pour l'avoir présidé, ainsi qu'à Sophie Carencu et Guillaume Viau pour avoir accepté de rapporter mon travail. Les discussions et échanges scientifiques que nous avons eus à l'occasion de

ma soutenance de thèse furent très intéressants, enrichissants et porteurs d'une multitude d'idées pour la suite du projet, je ne saurais assez les en remercier.

Cette thèse ne serait pas ce qu'elle est scientifiquement sans l'aide de collaborateurs précieux. Laurent Lermusiaux et Benoit Mahler auront en ce sens grandement contribué aux avancées scientifiques apportées autour de mes thématiques de thèse, que ce soit respectivement par la réalisation d'expériences de diffusion de rayons X aux petits angles que par la réalisation de microscopie électronique à transmission à haute résolution. Merci à eux deux pour leur grande contribution, leur aide et toutes les discussions scientifiques très stimulantes, poussées et enrichissantes que nous avons pu avoir ensemble.

Elisabeth Errazuriz et Bruno Chapuis tiennent également une place particulière dans ces remerciements, comme responsables du microscope électronique à transmission que j'ai pu utiliser toutes ces années durant à la plateforme CIQLE de Lyon. Merci pour leur amitié et l'aide technique apportée au MET lorsque ce dernier était d'humeur capricieuse.

Un grand merci à Brunot Canut pour nous avoir permis de réaliser des expériences de RBS à l'INL de Lyon, le tout dans un cadre très convivial, sympathique mais aussi très pédagogique en ce qui concerne la découverte pour moi de cette nouvelle technique expérimentale d'analyse.

Je remercie Gilles Patriarche pour les très importantes informations qu'il a pu nous fournir sur la structure cristallographique de nos nanorubans de sulfure d'indium, grâce à la réalisation d'expériences de microscopie électronique à transmission à haute résolution, de diffraction électronique en aire sélectionnée et de spectroscopie à rayons X à dispersion d'énergie au C2N de Palaiseau. Dans cette même optique, je remercie Marta de Frutos et Patrick Davidson, pour les discussions scientifiques que l'on a eues ensemble et quant à l'accueil chaleureux qu'ils m'ont apporté lors de sessions d'expériences de microscopie électronique à transmission à haute résolution au LPS de Orsay.

Les expériences de dichroïsme circulaire se sont déroulées sur la plateforme de l'IBCP de Lyon, et je remercie donc Roland Montserret et Eric Diesis qui étaient responsables de cette plateforme.

Enfin, mes pensées vont également envers nos collaborateurs de l'INSP de Paris, Laurent Coolen et Jiawen Liu, avec qui nous avons pu obtenir de très beaux résultats scientifiques en ce qui concerne les propriétés optiques d'auto-assemblages de nanoplaquettes de CdSe.

Lors de cette thèse, j'aurai eu le plaisir d'enseigner la chimie à nombre d'étudiants, de la licence Sciences de la Matière au master Féadep préparant les étudiants de l'ENS de Lyon au concours de l'agrégation de sciences physique et chimique. Je tiens à glisser un mot ici à leur rencontre, c'est grâce à eux que j'ai pu faire mes premières armes en tant que professeur agrégé et à goûter aux plaisirs de l'enseignement, face à des étudiants toujours plus curieux et motivés. Je pense également aux stagiaires que j'ai pu aider scientifiquement de près ou de loin, et notamment à Marie-Aliénor Zaretti que j'ai eu le plaisir de coencadrer lors de son stage de L3 ici au laboratoire. Merci à tous pour leurs agréables retours qui m'encouragent à continuer cet exercice de transmission des connaissances et d'aiguillage de nos esprits par la physique et la chimie, cette science qui nous permet de mieux comprendre le monde qui nous entoure et de combattre l'obscurantisme malheureusement grandissant au sein de nos sociétés.

Le département de chimie de l'ENS ne fonctionnant pas tout seul, j'adresse en ce sens un grand merci à ses directrices, Elise Dumont et Belen Albela : merci pour votre confiance. Merci également à Clément Courtin, Benjamin Neveux et le pôle tech-

nique en général du département de physique et de chimie de l'ENS pour leur aide et grande efficacité pour tout ce qui concerne l'aspect expérimental de l'enseignement de la chimie à l'ENS. Enfin, un grand merci à Martin Vérot, mon ancien professeur et désormais collègue en chimie orbitale, sans qui la qualité des enseignements à l'ENS ne pourrait être ce qu'elle est. De ces personnes qui font tourner la machine éducative de l'ENS, je remercie bien entendu tout le reste de l'équipe éducative, et plus particulièrement mes collègues et amis Thibault Fogeron et Vincent Wieczny.

Car humainement parlant, mener une thèse ne consiste pas seulement à partager de beaux moments scientifiques, mais également de beaux moments de vie et d'amitiés. Je dédie donc mes prochains remerciements tout particulièrement et chaleureusement à Margaux Roux, mon amie et complice de thèse et d'enseignements. Merci à toi d'avoir toujours été là pour moi, reste telle que tu es avec ton enthousiasme et ta belle énergie, je suis fier de te compter parmi mes amis proches. Et de ceux-ci bien évidemment, je remercie et embrasse également mes amis de promotion de l'ENS, ma chère Alina Cristian, notre monsieur suisse Eliott Le Du, la team geyser Nathan Wybo et Arthur Saintier, mesdemoiselles Pauline Colinet et Madleen Rivat, Jean Lepers-Rouillon, mes bichettes Emma Van Elslande et Loïc Cuau et mon sublime patou alpin Martin Doll.

Je garde enfin mes plus sincères remerciements à mon cercle très proche qui m'ont soutenu dans ma thèse ces trois dernières années, à commencer par mes amis d'enfance et de musique : François Villette, merci vieux frère d'avoir aussi toujours été là pour moi, pour tout ces perniflards partagés ensemble et ces voyages, tant de chemin parcouru depuis cette échange de gomme en cours de FM... Merci à toi Virginie Bois, pour nous avoir rejoint en amitié avec François, de nos soirées lycéennes à Lons-le-Saunier à nos époques universitaires entre Besançon et Dijon. A ce propos, mon époque dijonnaise n'aurait pas été la même sans toi Roman Brönimann, *partner in crime* à la fac, on a encore de nombreux coins à fondue à visiter ensemble à travers la Suisse. Je pense enfin à mes amis de musique irlandaise et de bals folk ; à Thierry Bellenoue et Maryline Bonin, mes partenaires de toujours à la flûte traversière, à Esther Peyronel pour ces deux magnifiques années que nous avons vécues ensemble au début de ma thèse, et aussi à Paul Fermé et Régis Marlaud pour toutes ces heures musicales qui ont rythmé mes semaines de thèse. Nous en avons écumées des scènes ensemble avec Hoctomoz, merci à vous pour cette belle complicité musicale qui nous aura fait voyager et qui est partie pour perdurer encore un bon bout de temps !

Enfin, je termine par le plus important, ma famille, qui a toujours su être là pour me soutenir et m'aider, tant dans mes études que dans ma vie en général. En particulier, merci à ma soeurette et mon frangin, Laurie et Josselin Guillemeney, il s'en sera passé du chemin depuis notre enfance à la Grange Bedey ! Même si ce mot ne suffit pas à décrire ma reconnaissance envers eux, un immense merci à mes parents Monique Guyennot et Jean-Marie Guillemeney, pour leur amour, leur soutien sans faille de tout instant et leur réelle inspiration. Je leur dédicace cette thèse.

Et merci à tous ceux que j'aurai malencontreusement oubliés : ne le prenez pas mal, mais il faut bien finir ce manuscrit et cette section un jour !

Lilian

Contents

Introduction	xiii
1 State of the Art and motivations	1
1.1 Generalities on semiconducting nanomaterials	1
1.1.1 Electronic description of a semiconductor	1
1.1.2 Brief overview on Quantum Dots	3
1.1.3 Anisotropic semiconducting nanomaterials	6
1.2 Syntheses of colloidal nanoplatelets	11
1.2.1 Generalities about the growth of nanocrystals	11
1.2.2 Importance and roles of surface surfactants	12
1.2.3 Growth of 2D-nanomaterials	13
1.3 Conformation of colloidal nanoplatelets	16
1.3.1 Principal curvatures	16
1.3.2 Polymorphism of nanoplatelets	17
1.3.3 Ligand-induced surface stress effects on the NPL shape	19
1.3.4 Ligand-induced surface stress effects on the optical properties of NPL	20
1.3.5 Shape effect on the chiroptical properties of NPL	21
1.4 Assemblies of colloidal nanoplatelets	23
1.4.1 Colloidal stability and interactions in solution	23
1.4.2 Liquid-liquid interfacial assemblies	25
1.4.3 Assemblies in solution	28
1.4.4 Optical properties of assembled nanoplatelets	30
2 Shape-control and formation mechanism of ultra-thin In₂S₃ nanoribbons	33
2.1 A quick overlook on indium sulfide in literature	34
2.2 Synthesis of indium sulfide nanoribbons	37
2.3 Composition and crystallographic structure	38
2.4 Shape control and synthesis optimization	45
2.4.1 Morphological control: from hexagons to nanoribbons	45
2.4.2 Synthesis optimization of NR	48
2.5 Insights into formation mechanism of In ₂ S ₃ NR	52
2.6 Colloidal stability and bundling in solution	56
2.7 Outlooks	61

2.8	Materials and experimental methods	62
2.8.1	Starting Materials and chemicals	62
2.8.2	Instrumentation	62
2.8.3	Solvothermal synthesis of In_2S_3 NPL	63
2.8.4	Growth kinetics: Time-resolved in-situ synchrotron SAXS / WAXS	63
2.8.5	Bundling of In_2S_3 nanoribbons	63
3	Conformation control of indium sulfide nanoribbons by ligand ex- change	65
3.1	Synthesis and characterization	66
3.2	Conformation control by ligand exchange	74
3.3	Induction of chirality in InS nanoribbons	84
3.4	Outlooks	86
3.5	Materials and experimental methods	87
3.5.1	Starting Materials and chemicals	87
3.5.2	Instrumentation	87
3.5.3	Solvothermal synthesis of indium sulfide nanoribbons	88
3.5.4	Unfolding of indium sulfide nanoribbons by ligand exchange	88
3.5.5	Functionalization of indium sulfide nanoribbons by L- or D- Penicillamine using a phase transfer method	89
4	Self-assemblies of CdSe nanoplatelets	91
4.1	Syntheses and assemblies of 4ML-CdSe NPL	92
4.1.1	Synthesis of 4ML-CdSe NPL	92
4.1.2	Self-assembly of 4ML-CdSe NPL	94
4.2	Syntheses and assemblies of 5ML-CdSe NPL	97
4.2.1	Synthesis of 5ML-CdSe NPL	97
4.2.2	Self-assembly of 5ML-CdSe NPL	98
4.2.3	Optical properties of nanoplatelets assemblies	99
4.3	Outlooks	104
4.4	Materials and experimental methods	105
4.4.1	Starting Materials	105
4.4.2	Instrumentation	105
4.4.3	Synthesis of cadmium myristate	105
4.4.4	Synthesis of cadmium oleate	106
4.4.5	Synthesis of 4ML-CdSe NPL	106
4.4.6	Synthesis of 5ML-CdSe NPL	107
4.4.7	Self-assembly of 4ML-CdSe NPL	107
4.4.8	Self-assembly of 5ML-CdSe NPL	108
	Conclusion	109
	Bibliography	117
	List of Figures	127
	List of Tables	129
	Nomenclature	131

Introduction

Nanomaterials represent a topic of growing interest inside the scientific community as well as in the general public, owing to the large number of potential applications they could offer in our daily life. The recent ability to probe matter at a nanoscale level - thanks to electron or atomic force microscopies for instance - has paved way to the design and the synthesis of new nanomaterials with novel and outstanding properties. Indeed, properties of material structured at the nanoscale level may differ greatly from the ones of their bulk equivalent. By way of illustration and as regards mechanical properties, the widespread assertion "smaller is stronger" is illustrated on numerous nanomaterials: for example, it was reported that gold nanowires feature a yield strength which is at least two orders of magnitude higher than its bulk equivalent [1]. A same trend is reported for nickel nanoparticles that exhibits ultrahigh compressive strength unprecedentedly reported for metallic material [2].

Moreover, nanomaterials were used fortuitously by glass-makers since the dawn of time for their amazing behaviour with light: the oldest example known is the Lycurgus cup from the 4th century B.C. that presents a different colour whether light is transmitted or reflected by it. This behaviour is related to silver and gold nanoparticles that are dispersed in a colloidal form throughout the cup. Latter, from the 4th century A.C. to the 17th century, Murano's glass-blowers kept secret the fabrication of the "ruby glass", a deep red glass that owes its colour also from gold nanoparticles.

More recently, in the last decades, a lots of research were achieved on semiconducting spherical nanoparticles, also named quantum dots (QD) for their remarkable optical properties. Actually, QD exhibit an absorption and an emission which are size dependent. Their diameter can accurately be tuned experimentally along an excellent size-dispersion of the particles. That makes QD great candidates for photonics devices and display. As an illustration, Samsung has already launched few years ago televisions based on quantum dots in place of traditional luminophores. The potential of QD in terms of sensing and bio-imaging also makes them an attractive field of research even if their biocompatibility is limited for the moment [3].

We focus in this thesis on anisotropic 2D-semiconducting nanomaterials, named also nanoplatelets (NPL). As 2D counterparts of QD, such materials present in the same way amazing properties that may even outperform the ones of QD. The attraction NPL create within the scientific community is reflected in the literature: the number of publications per year with the key-word "nanoplatelets" has grown exponentially since 2003 (Figure 1).

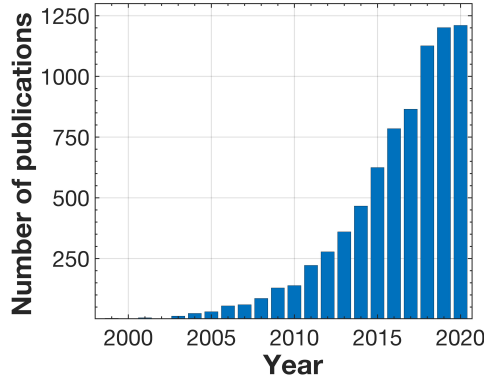


Figure 1 – Number of publications with the key-word "nanoplatelets" per year, from ISI Web of Knowledge in May 2021, on a total of 8033 records since 1995.

Colloidal semiconducting nanoplatelets are particularly promising materials for photonics and optoelectronics applications, as they generally display outstanding optical properties due to the strong quantum confinement that occurs along their thickness. These properties may be accurately controlled by a fine tuning of their morphology - i.e. their size and shape - or their geometric conformation.

For instance, cadmium selenide NPL exhibit absorption and emission spectra which depend on their thickness [4]. A lots of reports state the experimental tuning of their thickness with reaction parameters (such as the cadmium precursor or the temperature of injection of precursors) [4, 5, 6].

As regards the conformation of semiconducting NPL, only few works in the literature describe a direct interplay between their optical properties and their conformation. For instance, it was reported that the folding of CdTe nanoplatelets occurs along a red shift of their excitonic energy [7].

Finally, reaching micrometric superstructures of assembled NPL is of great interest as it may give rise to new interesting collective properties (such as FRET [8]) and may pave way to the conception of new optoelectronics devices.

The aim of our thesis was then to control these parameters (i.e. morphology, conformation and self-assembly) and shed light on the mechanisms involved in their control through the study of two main nanomaterials: indium sulfide and cadmium selenide.

In a first chapter, we describe the general framework of this thesis and the stakes related to it. We draw a quick overview on QD in the literature. We then focus more precisely on 2D-nanomaterials and especially cadmium selenide nanoplatelets which represent a model system as their synthesis and properties are abundantly described in the literature. Some concepts about the growth mechanism of nanocrystals are then given, from LaMer's model to recent suggestions of mechanisms for anisotropic nanomaterials. We then set a framework to the study of NPL conformation, by introducing principal curvatures and their link with NPL properties. Finally, we describe the interactions NPL may have in solution and from which NPL assemblies may originate.

In the second chapter, we report the shape-control and the formation mechanism of ultra-thin γ -In₂S₃ nanoribbons. The combination of Rutherford backscattering spectrometry, X-Ray photoelectron spectroscopy, X-Ray diffraction and high-angle annular dark field scanning transmission electron microscopy experiments allows us

to determine non ambiguously the composition and the crystallographic structure of the nanomaterial, whereas its morphology is investigated by transmission electron microscopy. We show that a very fine tuning of the lateral dimensions can be achieved through the control of the water content in the synthesis. Indeed, in anhydrous condition, hexagonal nanoplatelets are obtained. When the amount of water is increased, a shape-evolution of the nano-objects towards long nanoribbons is observed. We propose a growth mechanism for this synthesis from in-situ time resolved small-angles X-ray scattering experiments.

The third chapter is related to the conformational control of indium sulfide nanoribbons by ligand exchange. We show how initially coiled orthorhombic InS NR can be uncoiled by the exchange of their native octylamine surface ligand by a longer carbon-chain amine. The NR curvature depends on the carbon chain length: the longer the chain of the amine, the greater the unfolding. Our hypothesis is that the tuning of the stress imposed at the surface of the NPL can be achieved from the appropriate choice of surface ligands. Even the smallest change in low-energy interactions between alkyl chains within the ligand shell might be sufficient to tune this surface stress. The characterization of the nanoribbons and of their curvature is realized with the same set of experimental techniques as the one mentioned above.

Finally, we describe in a last chapter the syntheses and the self-assembly of four-monolayer and five-monolayer CdSe NPL. Twisted threads of individually distorted NPL are obtained, with an average length which can reach the micrometer. In collaboration with Laurent Coolen from the institut des nanosciences de Paris during Jiawen Liu's PhD, we evidenced by microphotoluminescence homo-FRET within the assembly of five-monolayer Cdse NPL, with an exciton migration over up to 90 NPL (500 nm).

CHAPTER 1

State of the Art and motivations

Chapter abstract

This part describes the general framework of this thesis, from generalities about semiconductors to colloidal semiconducting nanoplatelets.

We will first discuss quantum dots and describe the common properties of every semiconducting nanomaterial (size-dependent band gap, applications). Secondly, we will deal with 2D-semiconducting nanomaterials, mainly nanoplatelets, and give a brief overview on what is reported in the literature about their synthesis. Finally, we will focus on the conformation and the self-assembly of such nanoplatelets, topics which represent the focus of this thesis.

1.1 Generalities on semiconducting nanomaterials

1.1.1 Electronic description of a semiconductor

A solid is electronically described according to band theory. This theory is a corollary of the molecular orbitals theory that allows the representation in space of electron density at a given energy level inside a molecule, or in other words, molecular orbitals. These molecular orbitals (MO) are deduced from atomic orbitals (AO)^a, thanks to the Linear Combination of Atomic Orbitals method (L.C.A.O.).

If we consider two atoms nearby in space, their atomic orbitals can interact if their energies are close and if their overlap is not null. Thus, the interaction of N AO leads to $N/2$ bonding MO and $N/2$ antibonding MO, represented in an energy diagram as discrete levels (Figure 1.1). In a crystal, the number of atoms that interact is so important (typically in the order of 10^{23} atoms) that these levels of energy are very close and form one or several energy bands, similar to a continuum of energy whose width (around 1 eV generally) depends on the nature of the atoms and the overlap between their AO (Figure 1.1).

a. One might define what is after all an atomic orbital: without getting into details, an atomic orbital is a mono-electronic wave function solution of the Schrödinger's atomic and mono-electronic equation. The square of this wave function gives the probability density of finding an electron in space, whereas the representation of its angular part leads to the known representations of atomic orbitals (s, p, d, f...).

The energy bands are filled according to Fermi-Dirac statistics. At 0 K, all levels whose energies are below the Fermi energy E_F are filled with electrons. E_F is characteristic of the studied solid. We call valence band the last band partially or totally occupied at 0 K. We call conduction band the first empty band at 0 K.

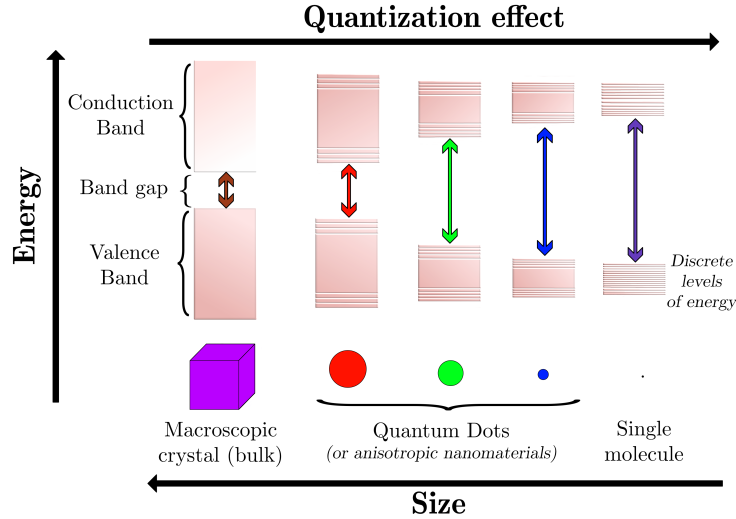


Figure 1.1 – Conversion of molecular orbitals (right) into bands (left) and size-dependence of the band-gap for a nanomaterial, here quantum dots (middle).

We are then able to classify the different solid in terms of conductivity (Figure 1.2):

- If the valence band is partially filled at 0 K (i.e the Fermi level is inside this band) or if the completely filled valence band overlaps with the conduction band, then the electrons can easily access to vacant levels: the material is a conductor. Its conductivity decreases with the temperature.

- If the completely filled valence band of the material is separated at 0 K from the conduction band by an energy gap of more than 4 eV, no electron can make a transition between these two bands: the material is an insulator. Its conductivity increases with the temperature as enough energy can be supplied to promote a little bit this transition.

- If the band gap is between 0 and 4 eV, this last phenomenon is amplified : when the temperature is increased or a photon absorbed, some electrons of highest levels of the valence band may be promoted to the conduction band. The freed levels in the valence band can be occupied by electrons of weaker energy levels of this same band. These vacant sites define what we call a hole, a fictive and positively charged particle that also ensures the conductivity inside the material: such a material is a semiconductor. The semiconductor is qualified as intrinsic if the number n of negative charge carriers (electrons) is the same as the one of positive p charge carriers (holes), contrary to the case of n - or p -doped semiconductors.

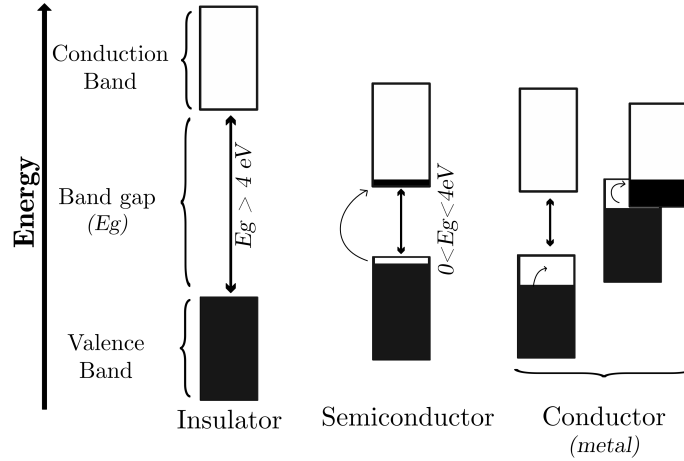


Figure 1.2 – Band structures of insulator, conductor and semiconductor.

The electron-hole pair generated inside a semiconductor material is called an exciton: the excited electron and the positive hole it generates are held together by a Coulombic attraction. The distance between them is known as the Bohr excitonic radius r_B and is given by :

$$r_B = \frac{\hbar^2 \epsilon}{e^2} \left(\frac{1}{m_e} + \frac{1}{m_h} \right) \quad (1.1)$$

where e is the charge of the particle, \hbar the reduced Planck constant, m_e and m_h are the effective masses of the electron and hole respectively depending on the material as for ϵ , its dielectric constant.

We will focus in this work on semiconducting nanomaterials: these materials present electronic properties that are intermediate between those of a bulk semiconductor and those of discrete atoms or molecules. The first materials reported in the literature with this kind of behaviour are spherical nanoparticles, called quantum dots (Figure 1.1).

1.1.2 Brief overview on Quantum Dots

Quantum Dots (QD) are spherical semiconductor clusters of hundreds to thousands of atoms whose interior is structurally identical to the corresponding bulk solid but with a substantial fraction of the total number of atoms at the surface [9]. The size of such semiconductor nanocrystals is smaller than the Bohr excitonic radius of the material: that leads to a quantum confinement and a number of interesting property changes as a size-dependent energy band gap [9] (Figure 1.1). This band gap $\Delta E(r)$ can be quantified by the Brus equation [10, 11] below :

$$\Delta E(r) = E_{gap} + \frac{\hbar^2}{8 \times R^2} \left(\frac{1}{m_e} + \frac{1}{m_h} \right) - \frac{1.8 \times e^2}{4\pi \cdot \epsilon_0 \cdot \epsilon \cdot R} \quad (1.2)$$

where $\Delta E(r)$ is the energy gap of the QD, E_{gap} is the band gap of the bulk material, R is the QD radius and m_e and m_h are the effective masses of the electron and hole respectively. \hbar is the Planck constant, e the elementary charge, ϵ_0 and ϵ

the vacuum and relative permittivities of the material. A QD can be seen as a good example of a "particle-in-a-box" as introduced in quantum mechanics lectures.

Thanks to this size-dependent band gap feature, it is experimentally possible to achieve a very fine tuning of the optical properties of QD: for instance, it was reported the synthesis of CdSe QD whose size increases with temperature and reaction time, leading to a redshift of the absorption and emission spectra of the QD [12] (Figure 1.3.E.). CdSe QD represents a popular choice for chemists as these QD have a narrow photoemission and a broad absorption [13], with a band gap which can be tuned from deep red (bulk band gap of 1.7 eV) to green (2.4 eV) by reducing the cluster diameter from 200 to 20 Å [9] (Figure 1.3.D.).

Moreover, it is possible with the good set of experimental parameters (temperature and reaction time, precursors of metals, length and nature of the ligands [14, 15] or stoichiometry of reagents [13]) to obtain nanocrystals with a very small dispersity and homogeneous shape, composition and crystal structure [4].

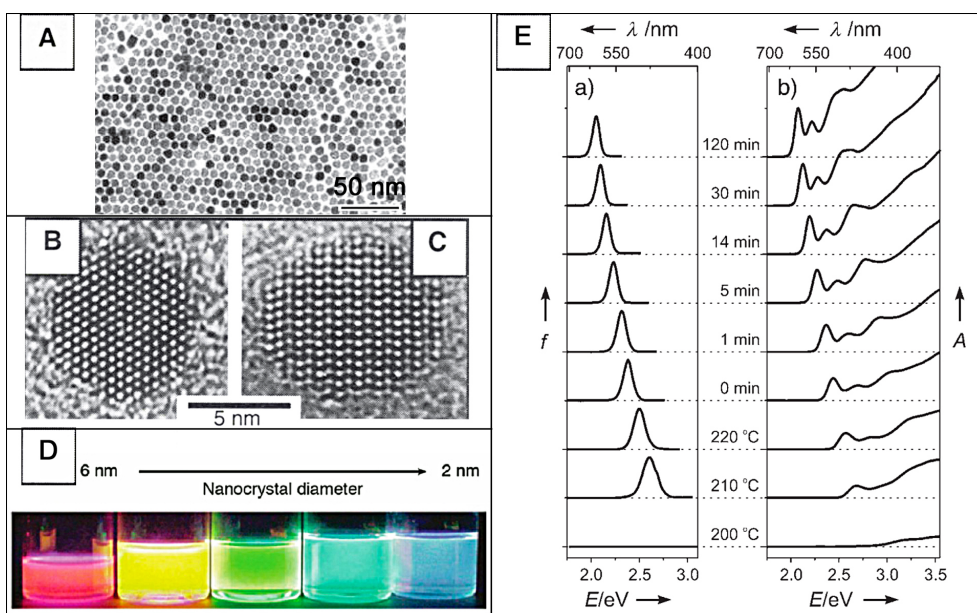


Figure 1.3 – (A.) Transmission electron microscopy (TEM) image of CdSe nanocrystals from [16] - (B., C.) Transmission electron images of CdSe nanocrystals with hexagonal structure viewed down different crystallographic axes. From [9] - (D.) Colloidal suspension of CdSe QD with different sizes under UV illumination. The NC size decreases from left to right (6 to 2 nm) and the corresponding increase in the bandgap is reflected in the change of the photoluminescence color from red to blue. From [17] - (E.) Evolution of the fluorescence (left, f) and absorption (right, A) properties of CdSe nanocrystals with the reaction temperature and time. From reference [12].

There are several ways to synthesize colloidal QD. In general, precursors of the material react in the presence of a stabilizing agent (e.g. a fatty acid) that will stabilize the growth of the particle and keep it within the quantum confinement limits [11, 12, 16]. Two approaches are generally used for the syntheses of QD : the heat-up approach (equivalent to a one-pot reaction) and the hot-injection process, where the precursors are injected separately in the reaction medium at high temperature [18]. Both approaches lead to inorganic nanoparticles capped and stabilized with a layer of surfactants/organic ligands coordinated at their surface and generally with a narrow size distribution. The general synthesis scheme of nanocrystals and the role of surfactants in the synthesis are discussed in more details in section 1.2.1.

If the size of the QD determines its optical properties, the nature of the surface of the QD is also critical for photoluminescence properties [14, 19]. Reconstructions in the atomic positions at the surface can occur and are caused by defects (such as vacancies, local lattice mismatches, dangling bonds) or adsorbates at the surface (i.e. ligands). All these chemical modifications at the surface create energy levels, called mid-gap states, within the energetically forbidden gap of the material [20]. The exciton created after excitation might be trapped inside these local energy minima states (i.e. trap states), degrading the electrical and optical properties of the material [9]. Radiative recombinations of the trapped charge carriers then produce luminescence that is substantially red-shifted from the absorbed light [11] (Figure 1.4).

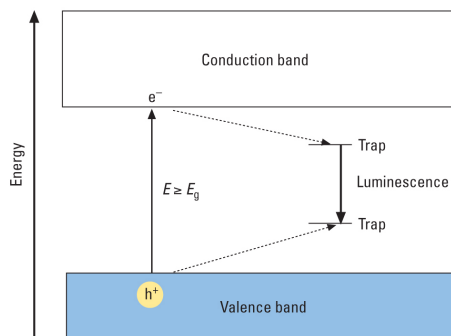


Figure 1.4 – Energy-level diagram showing promotion of an electron from the valence band to the conduction band and the existence of trap levels within the material, from [11].

To avoid the alteration of the optical properties of the QD, a passivation of its surface can be realized: the surface atoms are generally bonded to another material that eliminate the mid-gap states and so decrease the possibility of electrons to be trapped in these states. Such a passivation is achieved by overcoating the quantum dot (e.g. CdSe QD) with a higher-band gap semiconductor (e.g. ZnS) which constitutes a "quantum shell" (e.g. ZnS:CdSe QD). Eliminating the traps by growing such a different material around the nanocrystal in a core shell structure has a tremendous impact on its optical properties, as its photoluminescence quantum yields can for instance be increased up to 90% [20]^b. The passivation might play a role in other optical phenomena, such as fluorescence intermittency reported for CdSe nanocrystals which originates from Auger photoionization at the nanocrystal surface [21].

The tunability and the narrowness of their emission spectra make QD promising candidates for photonics applications and notably as light-emitting diode and display. Industrial applications of QD can already be found in this area, as Samsung currently sells TV made with QD replacing the traditional luminophores emitting in red, green and blue, in order to give "purest colors and 64 times more color variations than conventional TV".

Lasing can be achieved thanks to QD, in which population inversion and stimulated emission can be performed. The output color of the laser can be tuned easily by a control of the size and also of the surface of the QD as trap states may prevent the stimulated emission process [22]. Mid-infrared photodetectors can be based on QD [23] as well as photovoltaic material or dye-sensitized solar cells [24].

^b. As a comparison, 35 Å CdSe crystallites alone get a luminescence quantum yield of nearly 10% relative to Rhodamine 640 at room temperature [18].

The use of 3.0 nm oleate-capped CdSe QD as an efficient catalyst for different photoredox reactions is also reported (in particular C-C bond formation ; β -alkylation, β -amino-alkylation, dehalogenation, amine arylation, decarboxylative radical formation). CdSe QD are shown to be equivalent or superior in efficiencies to the native metal catalysts and that without any reoptimization of the reaction conditions [25].

Finally, QD could be of great importance in medicinal or biological applications, in the field of optical sensing and biological imaging [26], as fluorescent dyes, fluorescent probes or sensors. QD can indeed reach luminescent quantum yield of classical organic dyes but with a better resistance towards photo-bleaching: for example, whereas Rhodamine B, a classical tracer dye soluble in water, presents photo-degradation after 10 minutes of irradiation, a CdSe QD sample can be stable for 4 hours. That could be of potential interest in biological applications as biolabelling or imaging [11]. However, QD are generally synthesized in organic media and contain heavy metals (such as cadmium) and therefore do not reach standards regarding cyclotoxicity^c or water-solubility for biological applications^d.

The concepts introduced here on quantum dots are transposable to nanomaterials of other dimensionalities, such as nanowires (1 dimension (D)) or nanoplatelets (2D) which we will now present.

1.1.3 Anisotropic semiconducting nanomaterials

An anisotropic growth or a self-assembly of nanoparticles can lead to a huge variety of nanomaterials with reduced dimensionality.

Quantum Dots represent 0D nano-objects where excitons are confined in all direction of space, whereas nanowires or nanorods are 1D-nanomaterials with an exciton confined in the diameter direction. Size and shape control of such nanorods are also directly linked with a band-gap control, as emission of nanorods redshifts with an increase in either length or width [28, 29].

2D-nanomaterials as nanoplatelets (NPL) get their exciton confined only in the thickness dimension. The difference in dimensionality between these nanomaterials is correlated with a difference in their density of states [17]: as a corollary, it affects the electronic structure and the optical properties of the nanocrystals (Figure 1.5). We will now retain our attention on colloidal NPL.

Colloidal nanoplatelets are 2D nanocrystals covered on both sides with a monolayer of organic surfactant molecules bound to their surface by a functional group. These ligands provide stability to a structure that is normally not stable as a few layers form. Such semiconducting colloidal 2D-nanomaterials are classified under different names according to their aspect ratios and shapes (i.e. nanosheets (NS), nanoplatelets (NPL), nanoplates, nanoribbons (NR), quantum belts (QB)...), even if all might be registered semantically as nanoplatelets in a purely pragmatical point of view.

c. CdSe QD can undergo a photolysis under UV light that produce Cd(II) ions, highly toxic in vivo [27]. To reduce the toxicity of QD in vivo, several solutions were proposed : the first is to encapsulate the toxic, fluorescent core of the QD within a layer of biologically inert material (organic polymers, Si or Zn based semiconductors...) and so create a core-shell QD [3]. Another and safer way foreseen is to replace the toxic heavy metals by a biologically compatible one, as zinc for example.

d. A way to make QD water soluble is to realize a phase transfer, during which the organic capping ligands of the QD (i.e. myristic acid, decanoic acid, oleylamine...) are replaced by water-soluble ligands.

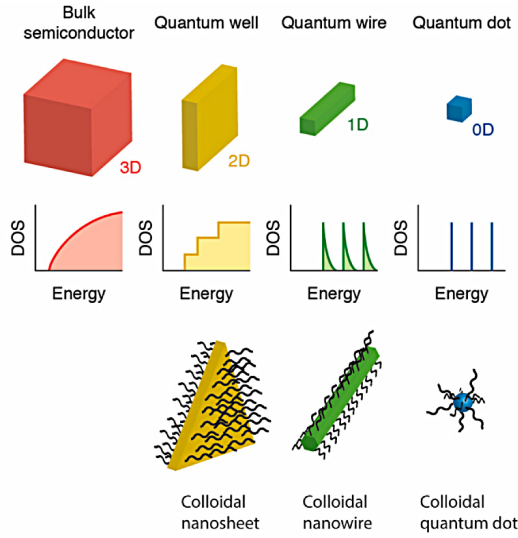


Figure 1.5 – Schematic representation of the density of states of a bulk semiconductor and of semiconductor nanostructures with reduced dimensionality, from 2D (step-like continuum) to 0D (discrete levels) by way of 1D (saw-like quasicontinuum). From [17].

Colloidal nanoplatelets differ from other types of 2D materials obtained for instance by exfoliation of a layered bulk sample in the sense they are usually synthesized from organo-metallic precursors in solution. We restrict ourselves to ultrathin NPL with a thickness in the range of the nanometer. A striking property of these objects is that their thickness can be controlled at the atomic level and hence their optical features.

A multiplicity of atomic composition in platelets has already been reported in the literature. We can mention for instance ZnS and ZnSe NPL [30, 31], PbS nanosheets [32, 33], Cu₂S metal sulfide NPL [34], or In₂Se₃ [35, 36] and In₂S₃ [37] NPL. NPL can adopt several main crystallographic structures and among others the wurtzite structure, the zinc-blende structure and the rock salt structure [38] (Figure 1.6). In order to modulate and enhance the optical properties of a single NPL (such as its quantum yield), complex structures can be engineered, such as core/crown or core/shell NPL [38] (Figure 1.6).

In the following, we focus on semi-conducting core-only nanoplatelets with an emphasis on II-VI nanoplatelets such as CdX (X=Se, Te or S) in the zinc blende [39, 4] or wurtzite [40] crystallographic phase (Figure 1.7). Wurtzite structures are generally obtained from cadmium acetate or halide precursors in long-chain amine solvents in a low temperature range (25-100°C), whereas zinc-blende structures are obtained from reaction of long-chain cadmium carboxylate precursors or in the presence of long-chain carboxylic acids within a higher temperature range (typically 130-240°C) [41] and with the injection of acetate. These structures are represented in Figure 1.7. In the case of zinc-blende NPL, as top and bottom surfaces are Cd terminated, an additional half non-stoichiometric ML of cadmium atoms is required.

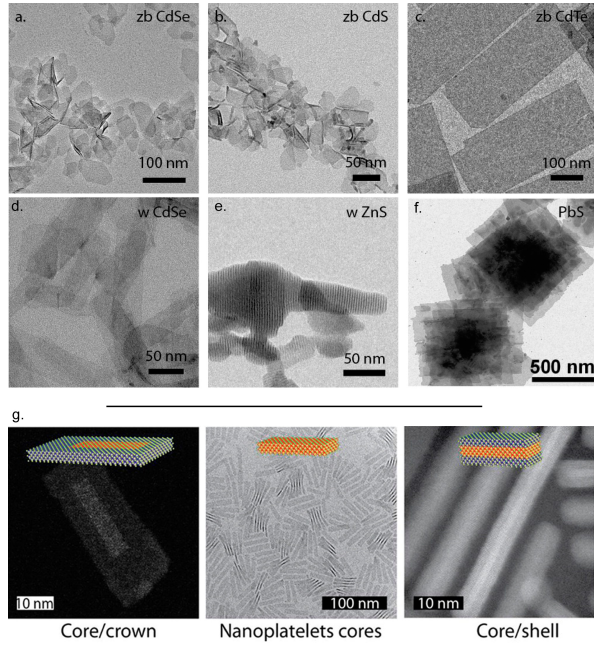


Figure 1.6 – TEM images of zinc blende (a.) CdSe, (b.) CdS, (c.) CdTe, wurtzite (d.) CdSe, and (e.) ZnS and rock salt (f.) PbS NPL - (g.) TEM images of (from left to right) CdSe/CdS core/crown NPL, core only CdSe NPL and core/shell CdSe/CdS NPL, from [38].

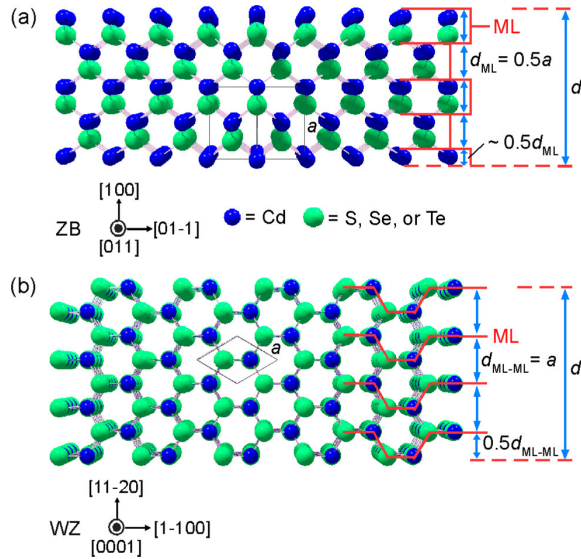


Figure 1.7 – Schematic representation of the atomic arrangements of the thin edge of 4.5 ML zinc-blende (a.) and 4ML wurtzite CdX (X=Se, Te or S) NPL (b.) from [41]. Red solid lines identify the biatomic (Cd-X) monolayers ML. d_{ML} (in a.) represents the thickness of a ML, d is the one of the nanocrystals. d_{ML-ML} (in b.) is defined as the inter-ML distance. a is the lattice parameter for the cubic (a.) or hexagonal (b.) unit cell.

Cd-based NPL are currently a hot spot of research, for the interesting electrical and optical properties they can offer [42], far superior to the ones of spherical QD.

Firstly, NPL exhibit extremely narrow and tunable absorption and emission spectra. As a result of a size-dependent quantum confinement effect, the optical properties of NPL vary strongly with their thickness. The thinner the platelet, the higher its absorption and emission energies [4]. No Stoke's shift is observed [38] (Figure 1.8).

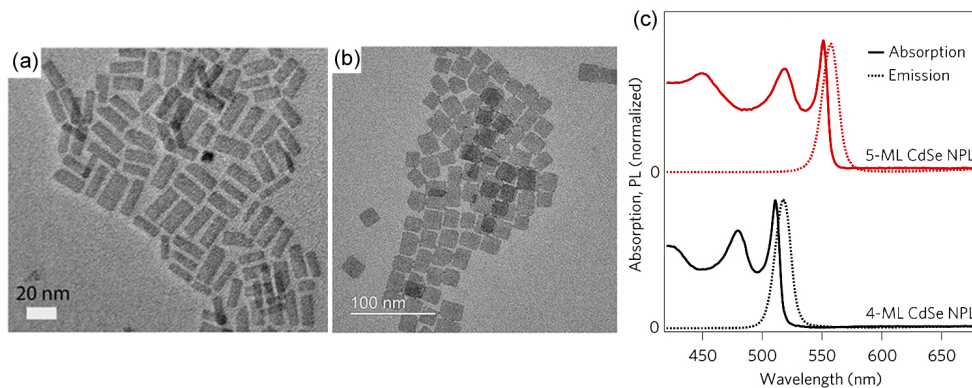


Figure 1.8 – (a) TEM image of rectangular (22 nm x 7 nm x 1.5 nm) zinc-blende 5.5 ML CdSe NPL, from [43] - (b) TEM image of 18 nm² square 4.5 ML zinc-blende CdSe NPL, from [44], of a thickness of 1.2 nm from [4] - (c). Absorption and emission spectra of 4- and 5-ML CdSe NPL illustrate the red-shifting of the spectra when the NPL get thicker. From [8]

Experimentally, NPL populations of different lateral dimensions and thicknesses can be obtained by an accurate control of the reaction temperature as well as the moment the precursors or the capping ligands are injected, or of the stoichiometry of the reaction [4, 39]. *Ithurria et al.* thus obtained different CdSe, CdS or CdTe NPL with lateral dimensions tuned from nanometers to a few of tens of nanometers and a thickness tuned to the monolayer [4].

Three main populations of CdSe NPL of different thicknesses are usually studied: 0.9 nm thick 3ML-CdSe NPL which emit at 463 nm, 1.2 nm thick 4ML-CdSe NPL which emit at 513 nm, and 1.5 nm thick 5ML-CdSe NPL which emit at 550 nm. The absorption spectrum is then an important feature to characterize the NPL: the first two excitonic features in energy are attributed to the heavy hole/electron (lowest energy) and light hole/electron transitions. A third broad one (highest energy) is attributed to the electron/spin orbit transition. Due to the strong confinement of the exciton inside these structures, NPL present a giant oscillator strength [38, 4]^e.

NPL have in general a high fluorescence quantum yield up to 50% [45, 4, 46]. Additionally, NPL exhibit a shorter fluorescence lifetime (of few nanoseconds) than the one measured for any other colloidal particles, making NPL the fastest colloidal fluorescent emitters. Compared to spherical CdSe nanoparticles at a same temperature and for similar quantum yield and emission wavelength, it is inferior by two orders of magnitude [4]. CdSe NPL can be described by an incoherent sum of two large orthogonal in-plane emission dipoles [47], strongly emitting an in-plane polarized light in its perpendicular direction [48]. Their absorption dipole at the excitation energy is nevertheless isotropic [49]. Works on core-shell CdSe/CdS show the aspect ratio of

^e. The oscillator strength is a dimensionless measure of the intensity of an electronic transition from one energy level to another inside the electronic system considered.

lateral dimensions has a great impact on the emission polarization of the NPL. Rectangular NPL feature a polarized emission and anisotropic emission patterns, whereas square NPL feature nonpolarized and isotropic emission [49, 50]. This can be appropriately described by the dielectric antenna effect induced by the elongated shape of the rectangular platelets.

Finally very low lasing thresholds for CdSe NPL have been reported. Values as low as a few $\mu\text{J}/\text{cm}^2$ have for example been measured for CdSe NPL [51, 52, 53] which is 5 times smaller than any previous threshold for colloidal NC, showing that NPL are excellent materials for optical gain and lasing. Moreover, NPL of different thicknesses can produce amplified stimulated emission in the red, yellow, green, and blue regions of the visible spectrum with low thresholds and high gains.

1.2 Syntheses of colloidal nanoplatelets

The general scheme of a colloidal nanocrystals synthesis consists in the reaction between molecular precursors, in presence of organic surfactants in an organic solvent. Organic surfactants can sometimes play also the role of solvent and cap the surface of the resulting nanoparticles. Nanoparticles syntheses are remarkable in the way they can produce dispersions of nano-objects with very narrow size and shape distributions.

We will describe in this section the general growth mechanism retained by the scientific community to understand the formation of such monodispersed particles (i.e. the LaMer-Dinegar model). We will then move on the different roles surface ligands may adopt with respect to the growth, the stability and the properties of nanocrystals. Finally, we will discuss the main phenomena responsible for the anisotropic growth of nanocrystals, the example of CdSe nanoplatelets representing a model study in the field of semiconducting nanomaterials.

1.2.1 Generalities about the growth of nanocrystals

In 1950, LaMer and Dinegar interpreted the formation of monodispersed sulfur colloids from the decomposition of sodium hydrogen thiosulfate in dilute hydrochloric acid in an organic solvent [54]. Since then, their model has remained for nearly 50 years the only explanation of how narrow dispersions of particles can be formed. LaMer's model states the formation of colloidal particles consists in three stages [55, 56], summed-up in the graphical representation of the concentration of monomers through time (Figure 1.9):

- **Step I:** The first stage is the formation of soluble monomers in solution from decomposition of precursors, until reaching and exceeding the limit of monomers solubility C_S (saturation concentration).

- **Step II:** When a minimum supersaturation concentration in monomers C_{min} is reached, an instantaneous and homogeneous self-nucleation (a burst) occurs. Nucleation depends exponentially on the monomer concentration [16] which reaches a critical supersaturation level C_{max} before decreasing.

- **Step III:** This step is followed by a growth by diffusion when the supersaturation concentration is between C_S and C_{min} . As the nucleation event has depleted a large part of the monomers, growth follows without further nucleation [16]. If the overall monomers concentration remains high during this step, the model postulates that particle growth will be favoured over dissolution back into monomers: remaining monomers are assumed to preferentially absorb onto small crystallites, as these present a higher surface free energy than larger crystallites which make the former less stable in solution [57, 16]. This growth kinetics results in a decrease in the particle-size distribution with time (i.e. a size-distribution focusing) and hence the production of highly monodisperse colloidal dispersions. Nevertheless, if the monomers concentration is or becomes too low, small particle dissolution back into monomers is favoured over monomer absorption. The slow diffusion of material onto the surface of larger particles (i.e. Ostwald ripening) preferentially happens and broadens the particle-size distribution (i.e. size-distribution defocusing). It is then important to follow and control the reaction parameters in order to stay in the focusing regime which leads to monodisperse nanocrystals dispersion [16].

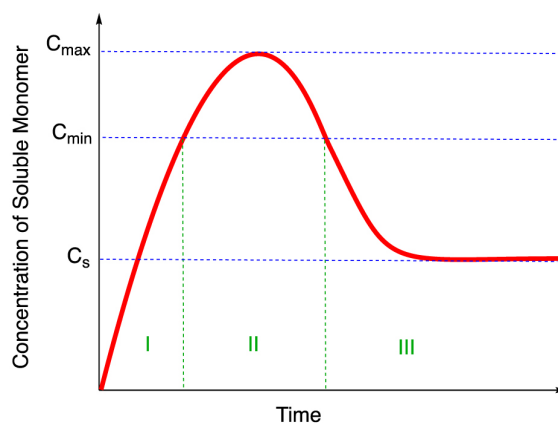


Figure 1.9 – Schematic illustration of the LaMer model, plotting the monomer concentration through the reaction time. Step I, II and III are described in the text above. Graph from ref [55].

This model applies to *Murray et. al's* hot-injection synthesis of CdE nanocrystals [18]: injection of reagents into the hot reaction pot leads to a short burst of homogeneous nucleation. The drop in temperature due to injection combined with the depletion of reagents through nucleation prevents any further nucleation. The reheating allows slow growth and annealing of crystallites as described in step III.

The growth temperature plays an important role on the average size and size distribution of crystallites. Moreover, to get a high monodispersity, nucleation and growth have generally to be temporally separated: nucleation has then to occur on a short time scale, but that does not mean it has always to be the case. Very recent alternative models [55, 58] show it could be possible to get narrow nanoparticle-size distributions despite a continuous nucleation in the medium, without doing the LaMer's hypothesis of an instantaneous nucleation, which was originally required to elaborate this model. Finally, the crystal growth may be dramatically influenced by surfactant molecules and we will now deal with this point.

1.2.2 Importance and roles of surface surfactants

Surfactants play significant roles during the nanocrystal synthesis, but also post-synthesis. Alkyl phosphine oxide, alkyl phosphonic acids, alkyl phosphines, fatty acids and amines, nitrogen-containing aromatics are classical organic ligands used to capped nanocrystals [16]. All these molecules contain an electron-donating metal coordinating group and a solvophilic group.

From a post-synthesis point of view first, the surfactant monolayer at the surface of the crystal allows them to gain in colloidal stability (see section 1.4.1 for details), according to the interaction alkyl groups of surfactants might have with the solvent. Adding a nonsolvent as ethanol or methanol [18] in the colloidal solution weakens these interactions and leads to a loss of stability of nanocrystals. Centrifuging the solution allows then to isolate nanocrystal from the rest of the solution and to obtain purified redispersion of nanocrystals. Moreover, as larger particles flocculate first, adding a small volume of nonsolvent may be performed to realized size-selective precipitation and so to enhance the dispersity of the sample. To a lesser extent, surfactants also prevent the nanocrystal from further chemical degradations. Moreover, we will see all along this thesis and the works it contains that surface ligands have a crucial role in

the final properties of nanomaterials, in terms of optics (absorption and emission, see section 1.3 page 16), conformation (chapter 3) and self-assembly (section 1.4.1 and chapter 4), and that exchanging them allows to control these properties.

During the synthesis, surfactants act on both stages of nucleation and growth. They can first modify the solubility and reactivity of precursors and so the overall reaction kinetics. During the nucleation, they can form complexes with reactive monomers [18] and play on the monomer's solubility and therefore on the nucleation rate. Moreover, during the growth process, surfactants can bind onto the surface of growing crystallites, lowering or preventing the addition of monomers onto it: in that way they affect directly the growth kinetics [18]. Indeed, regions of the nanocrystal surface are transiently accessible for growth only if surfactants are able to exchange on and off the surface, while they globally prevent the crystals to aggregate during the growth process thanks to their monolayered-coordination [16].

Finally, if surfactants allow to tune the growth kinetics and therefore the size of the resulting nanocrystals, they can also allow a shape-tuning of nanocrystals, from isotropic to anisotropic forms.

1.2.3 Growth of 2D-nanomaterials

We will restrict our discussion to the case of cadmium chalcogenide NPL as these anisotropic nano-objects represent a model of study abundantly described in the literature because of their outstanding optical properties.

CdSe and CdTe zinc-blende NPL are synthesized from cadmium carboxylates (e.g. cadmium myristate or cadmium oleate) and selenium precursors (e.g. selenium mesh, Se-ODE or trioctylphosphine-Se). A common feature in most of the syntheses of 4ML- and 5ML-CdSe NPL is the presence of cadmium acetate which is injected during the synthesis. Recent studies have shown that though it is used in most of current protocols, it is not mandatory and NPL can be obtained without it [59, 60]. CdSe NPL in the wurtzite crystallographic phase can also be obtained, mainly with the use of amine ligands [61]. In all the synthetic protocols reviewed, the thickness of the NPL increases with the synthesis temperature, from few monolayered NPL appearing between 100 and 150° C [62, 63] to 5 or 7 monolayered NPL at temperatures between 240 and 280°. The thickness can also be tuned with the choice of precursors: for example, chlorine precursors afford thick NPL [64, 6].

Compared to isotropic nanomaterials, highly anisotropic shaped nanomaterials as nanoplatelets get larger surface areas and are metastable high-energy forms: their growth is not thermodynamically favoured and happens in a kinetically controlled regime [16]. An anisotropic growth can firstly be explained if there exists an initial anisotropy in the crystal structure of the nanocrystal or defects that lead to a symmetry breaking of the system during growth [65]. This can not be the case for cadmium chalcogenide nanoplatelets as they have a symmetric crystallographic structure. To explain such an anisotropic growth from isotropic crystal structured materials, different pathways have been put forward and depend each on the synthesis conditions adopted. In all cases, there must be necessarily a symmetry breaking during the nucleation and growth which does not pre-exist in the crystallographic structure of the material.

A first approach relies on the fact that high-energy facets of a crystal grow faster than low-energy facets. Indeed, the growth of a crystal facet depends exponentially on the surface energy [16]. Reactive monomers would attach selectively on facets of the crystallite and thus induce an anisotropic growth (path n°2 of Figure 1.10, used to explain the formation of 3ML-CdSe NPL [5]).

Indeed, Riedinger et al. show the nucleation barriers on narrow facets of zinc-blende CdSe crystallites are smaller than the ones on wide facets, after interpretations of experimental results, kinetic modelling, DFT and kinetic Monte-Carlo simulations [59]. This phenomenon results in a three-times faster growth on narrow facets (i.e. a lateral growth) and hence the obtaining of zinc-blende CdSe NPL. Such an anisotropic growth is energetically preferred over isotropic growth only if the concentration in reactive monomers is high enough for the limiting process of the growth to be the reaction at the nanocrystal/solution interface (i.e. for an "island-nucleation-limited" growth regime. On the contrary, in a "diffusion-limited" growth regime, quantum dots are preferred). Their model, based on this kinetic growth instability, also explains why CdSe NPL with a thickness below 2ML do not form as the low stacking probability of monomers onto thin facets cause nanocrystals to dissolve.

Let us note that, to enhance the anisotropic growth process, it may be possible to lower the energy and so the growth rate of a facet compared to others by selectively bonding organic surfactant molecules to this facet [16]: this might be the case when cadmium acetate is injected. Moreover, still by selective adsorption, ligands might make some facets more available for incorporation of monomers and so change the facet nucleation kinetics.

Such a growth scenario is also likely to occur in the synthesis of large CdSe NPL [45] where NPL seeds are first synthesized and growth occurs gradually via the slow external addition of monomers. In this case, the concentration in monomers is low enough during the growth to avoid the nucleation of new seeds. Recent in-situ Small-angle X-ray scattering (SAXS) experiments confirmed growth from monomers in solution is the case of a heat-up synthesis of 3 ML CdSe NPL [66].

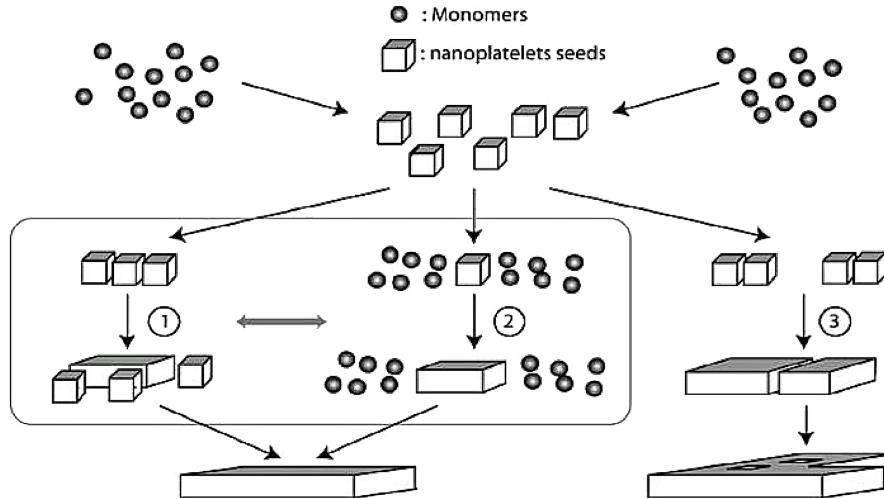


Figure 1.10 – Possible mechanisms for CdSe NPL lateral extension, from [5]. Initially, isotropic seeds with dimensions < 2 nm are formed from reaction between Cd and Se precursors - *Path 1 and path 3* : Self-organization of seeds (oriented attachments) at seed level (path 1) or in patches (path 3) - *Path 2*: Anisotropic growth through the continuous incorporation of soluble monomers onto existing NPL.

Oriented attachment (path n°1 and path n°3 of Figure 1.10) can be a second mechanism leading to the formation of anisotropic nanomaterials. It consists in the coalescence of faceted nanocrystals that eliminates two of their high-energy facets. Here again, surfactants can favour or prevent the attachment [16]. This oriented ripening pathway has been put forwards for the synthesis of 5ML-CdSe zinc-blende NPL [67] but also of PbS nanoplates [32].

Finally, Son et al. suggest a soft-template method to synthesize CdSe wurtzite nanosheets from a lamellar complex of cadmium with oleic acid, chloride and oleylamine [40]. This templating complex acts as a mold to guide the nucleation and the growth of the nanomaterial within limited regions of space. The mechanism is described below in Figure 1.11.

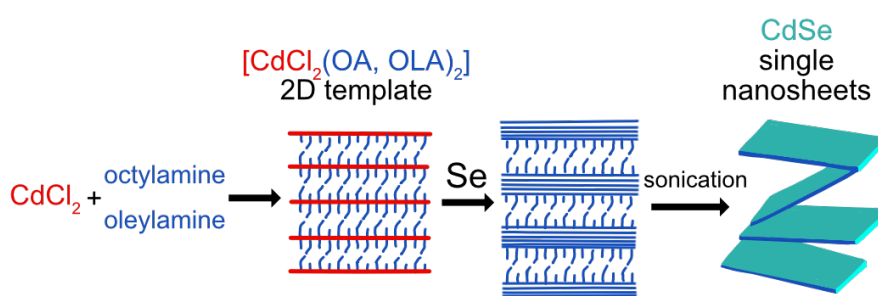


Figure 1.11 – Procedure to synthesize CdSe nanoplatelets from a templating method, from [40].

These three mechanisms are not establishing an exhaustive list and no universal mechanism can be given for such anisotropic growth. A combination of several of these mechanisms might occur, as it was reported for example for wurtzite CdSe NPL [68] where small clusters ripen anisotropically in lamellar mesophases, though magic-size clusters and small NPL are difficult to distinguish experimentally. Indeed, they have the same spectroscopic signature and their unambiguous distinction using Transmission Electron Microscopy (TEM) is not possible [5].

In any cases, the shape and size of NPL can be accurately tuned with the reaction conditions (temperature, solvent, surface ligands). For instance, on ZnSe material and for a same experimental protocol, increasing the reaction temperature lead to ZnSe long quantum belt (Figure 1.13H) instead of ZnSe small sticks [31] (Figure 1.13G). 3ML-CdSe NPL lateral dimensions can also be tuned by the reaction conditions: they increase with the reaction temperature or the carboxylic acid chain length, whereas they decrease with the rate of precursor injection [45]. Moreover, 3ML-CdSe NPL present generally larger lateral dimensions than 4ML- or 5ML-CdSe NPL [5].

1.3 Conformation of colloidal nanoplatelets

Among the wide variety of NPL shapes described in the literature (see also section 1.1.3), we will retain our attention on nanohelices, nanoribbons, nanoplatelets (strictly speaking) and nanotubes. The conformations and shapes of such 2D-nanomaterials depend on several factors such as the ligand at their surface [7, 69, 43, 70], their surface crystal lattice [71] or their lateral dimensions [72].

1.3.1 Principal curvatures

In order to describe, understand and compare the shape of these nanostructures, principal curvatures reveal to be pertinent parameters. Indeed, the preferred local curvature of NPL will dictate the way they bend and curl and eventually their 3D shape. Their spatial organisation, beyond the flat configuration, is crucial for several aspects such as their optical properties and their self-assembly.

Principal curvatures of a surface are the curvatures of this surface along two orthogonal directions, called principal directions. The product of the two principal curvatures is the Gaussian curvature, whereas their average is the mean curvature. Both are of interest to describe 2D-nanostructures. For instance, canonical shapes, represented in Figure 1.12.a., have different curvatures: a tube or an helicoid with an helical centerline have a finite mean curvature but a zero Gaussian curvature since one of their principal curvature is null. In contrast, an helicoid has a straight centerline, a zero mean curvature and non-zero Gaussian curvature. If we take the case of helicoid CdSe NPL [43] (Figure 1.13.a.), such an object is mathematically defined as a minimal surface, that is to say a surface that minimizes its area while being subjected to a stress. On such a surface, principal curvatures are equal in modulus but opposite at every point, leading to a zero mean curvature.

Gaussian curvature is relevant to describe 2D-nanostructure: a zero Gaussian curvature means the considered surface is a developable surface, in other words a surface that can be flattened onto a plane (by folding, bending...) without any distortion such as stretching or compression. Spiral CdSe ribbon (Figure 1.13.b.) can be characterized by their Gaussian curvature: indeed, such ribbon are isometric, i.e. they do not support elastic strain and therefore, according to the *Theorema Egregium* of Gauss, have a Gaussian curvature which must remain constant under smooth bending deformation [72]. This means that the Gaussian curvature is an invariant of the surface and that in order to change it we have to deform the surface and change the distances between the points within the surface.

Ghafouri et al. report the analytical description of the transition between a helicoid to a spiral ribbon [72], as regard the width of the nano-object. From the curvature tensor, the author introduce a parameter γ which is defined as the dimensionless ratio of the stretching energy per unit area of ribbon over the characteristic lateral bending energy per unit area. This parameter determines the ribbon morphology and depends on the ribbon width w as w^4 . By plotting the ribbon energy minimum as a function of their width (Figure 1.12.b.), the authors demonstrate ribbons can adopt only two stable states: a helicoid state for a small and finite width w^* and an isometric spiral shape when the width is increased to infinity. The transition between these two shapes is discontinuous and spiral ribbons of finite width are necessary unstable.

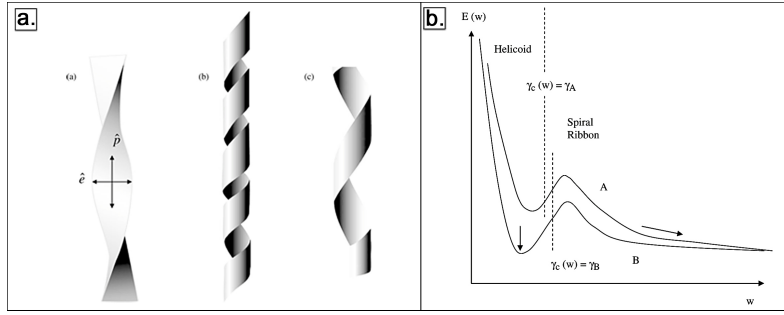


Figure 1.12 – (a.) Characteristic ribbon configuration, from left to right : helicoid, isometric spiral and intermediate configuration, from [72] - (b.) Ribbon energy minimum $E(w)$ as a function of the ribbon width w (schematic). The curve marked A corresponds to a larger value of the Foppl-von Karman γ and B to a lower value. From [72].

But if we want to rationalize all shapes, we need to find a theoretical framework in which to reason. The theory of thin plates has been an advanced topic in mechanics because of the complexity of shapes which can be formed from this simple unique shape. The shape of a thin NPL is dictated by an interplay between geometry and energy (which is function of the strain or the bending for example). In that sense, energy minimization is not the only condition that dictates the shape of a thin plate that must also fill geometrical constraints: the example above of isometric spiral CdSe ribbons that must respect the *Theorema Egregium* of Gauss is a good illustration of such geometrical constraints. If a NPL only satisfies the energy criterion (i.e. if the geometry adopted only corresponds to a local minimum in energy), that can potentially lead to frustrated systems and residual stresses that have to be taken into account in order to predict the shape of the NPL.

1.3.2 Polymorphism of nanoplatelets

A high diversity of nanoplatelets shapes can be found in the literature. A lot of semi-conducting NPL are flat (i.e. they have infinite curvatures at every point). For instance, CdSe NPL with thicknesses beyond 4 ML are in most cases flat. This is also the case for CdTe NPL which can retain this flat shape over large distances. Flat hexagonal InSe [35], In₂S₃ [37] or In₂Se₃ nanoplatelets [36] (Figure 1.13.d.) were reported as well as flat rectangular [33] (Figure 1.13.e.) and square [32] PbS nanosheets.

However, this infinite curvature configuration is not universal and multiple examples of curved NPL have been reported. Thin 3ML-CdSe NPL are curved most of the time [45, 70, 66, 73]. Depending on their lateral dimensions they can appear as folded sheets [45] or helices [69, 70, 73]. This last case was notably shown by cryo-TEM on rectangular 3ML-CdSe NPL coated with silica to fix the spiral shape conformation adopted in suspension which lower their total energy [70] (Figure 1.13.b.). In all cases, 3ML-CdSe NPL do not display any Gaussian curvature, as one of their principal curvatures is null. A preferred bending axis and a folding direction always along the [110] axis are adopted. The final geometry of 3ML-CdSe NPL depends then on the orientation of their edges and their lateral dimensions. Interestingly, the curvature does not appear after the synthesis but the NPL grow curved as shown by time-resolved SAXS. This enables the "closing" of the curved sheets into nanotubes in some cases [61].

Such cylindrical curvatures are also observed in In_2S_3 coiled nanoribbons [74] which close into In_2S_3 nanotubes as the reaction temperature is increased [75] (Figure 1.13.c). The shape and size of the nanoplatelet can thus be accurately tuned with the reaction conditions (see the example of temperature-dependent synthesis of ZnSe QB or small sticks [31] in section 1.2.3 and Figure 1.13.f.).

A same nano-object can then adopt different conformations according to various conditions: thicker CdSe NPL are usually flat but when an excess of oleic acid is added, they twist and undergo a transition from a flat to a helicoidal shape with a non-zero gaussian curvature [43] (See TEM images in Figure 1.13.a.). In this case, the centerline of the helicoid is also the [110] crystallographic axis but this geometry is distinct from the helicoidal ribbon described earlier. Finally, crumpled sheets have been observed in the case of In_2S_3 nanoplatelets synthesized at high temperature [76].

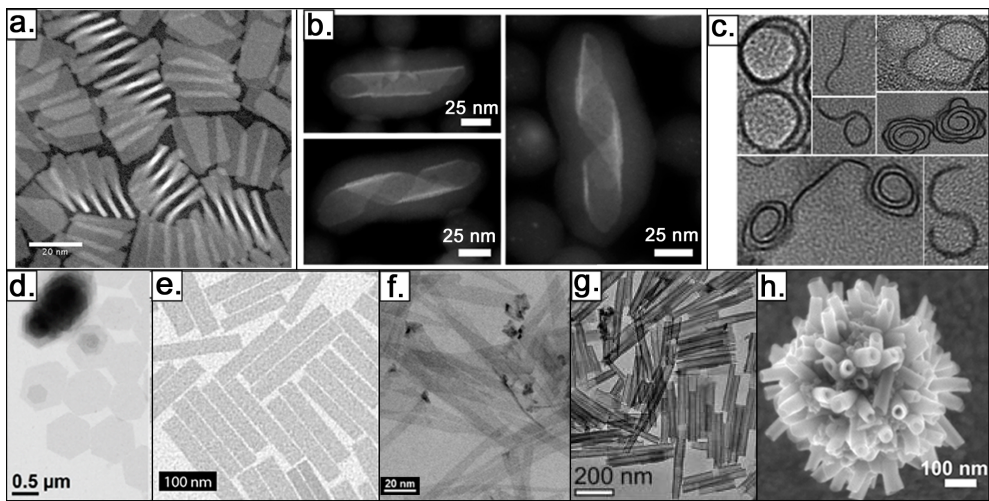


Figure 1.13 – (a.). HAADF-STEM images of twisted NPL (helicoid) after addition of oleic acid on a solution of flat NPL, from [43] - (b.) HAADF-STEM images of helical NPL (isometric spiral) which conformation in solution is fixed by a coating with silica, from [70] - TEM images of : (c.) In_2S_3 coiled nanoribbons [74] and (d.) Hexagonal In_2Se_3 NPL [36] - (e.) PbS rectangular nanosheets [33] - (f.) ZnSe quantum belts [31] - (g.) CdSe nanotubes [45] - (h.) SEM image of CdSe multiwalled nanotubes [61].

1.3.3 Ligand-induced surface stress effects on the NPL shape

An important feature of colloidal NPL is that the surfactant monolayer at their surface induces a surface stress. If we consider two crystals with different lattice parameters bonded together, the atomic arrangements at the interface will accommodate. The lattice parameter of the dense crystal will increase while the one of the less dense one will decrease. There will be a surface strain at the interface whose magnitude depends on the original mismatch between the two crystals. The same kind of phenomenon occurs with surface ligands. When they adsorb at the interface, organometallic bonds are created and deform the surface of the crystal.

Such surface stress was already reported for thiol self-assembled monolayers on gold cantilevers [77] and more broadly it is well known that surface adsorbates induce surface stress on crystalline surfaces. The alkanethiol ligands used by *Berger et al.* [77] were shown to self-assemble into a well-ordered densely packed film at the surface of the nanoparticle, each alkyl chain exhibiting a tilted orientation compared to the normal of the surface in order to optimize inter-chains interactions. This ligand monolayer imposes a compressive surface stress which strength increases linearly with the length of the alkyl chain and with the number of adsorbed molecules.

It was shown that ligand can induce surface stress on QD and that this stress can be tuned by the appropriate choice of surface ligand. By choosing a σ -donor or a π -acceptor ligand, the surface reconstruction of QD can be achieved accurately and so the exhibition of whether compressive or tensile stress [71]. Such a surface stress tuning should be possible on 2D-nanomaterials.

Let us consider again the case of flat CdSe NPL that twist upon the addition of oleic acid [43] (Figure 1.13.a.). The obtaining of a helicoid NPL is correlated with an elastic strain induced by the ligand adsorption at the surface of the NPL. Indeed, a twisting involves negative Gaussian curvature and thus a stretching of the crystalline lattice which experimentally can only originates from the oleic acid addition. Oleic acid ligands may self-assemble on the surface and thus induce a mechanical stress due to a mismatch between the crystalline and ligand lattices. As ligands close to the rim have more space to splay than ligands at the center of the NPL which got a higher neighbors density, a gradient of strain between the center and the edge of the NPL is expected to be at the origin of the twisting.

Another example is the spontaneous folding of CdTe nanosheets induced by the ligand exchange of native oleic acid ligand by thiol-containing ligands [7]. Thiol attachment on basal plane of the nanosheets leads to the formation of an external CdS monolayer. The lattice parameters of this CdS layer largely mismatch with the one of the CdTe lattice parameter (about 11.4%), resulting in a tensile strain in the CdS layer and a compression strain in the CdTe core layer. These strains leads to a spontaneous relaxation of the nanosheets by bending and rolling. The folding direction of the nanosheets may also depends on the orientation of thiol molecules on the surface and the elastic intrinsic properties of zinc-blende CdTe structure^f.

Inversely, a ligand exchange of native-carboxylate ligands by halide ligands reduces the surface stress imposed on 3ML-CdSe NPL and leads to their unfolding [69]. Indeed, these carboxylate-capped NPL initially fold into helices in order to release their internal elastic energy, as carboxylate ligands impose a tensile stress on the top and bottom facets of the NPLs which are oriented at 90° from each other (Figure 1.14).

^f. This is consistent with the work of *Berger et al.* described previously, about compressive surface stress caused by thiol ligands surface attachment on gold nanoparticles.

The same behaviour was mathematically modelled after observation of chiral seed pods opening [78] (Figure 1.14.f), showing that the shrinkage of two layers in perpendicular directions is sufficient to turn an initial flat pod into a helix. Considering the metric tensor and curvature tensor of the pod and in the framework of the theory of incompatible elasticity, the configuration of the minimal energy of the system is determined as a competition between stretching and bending energies and is dependent of the width w of the pod. The results are in agreement with the one announced previously for the description of the helicoid to spiral transition [72], i.e. narrow strips exhibit a pure twist (bending-dominated regime for small w) while wide strip adopt the shape of a cylindrical helix (stretching-dominated regime for large w).

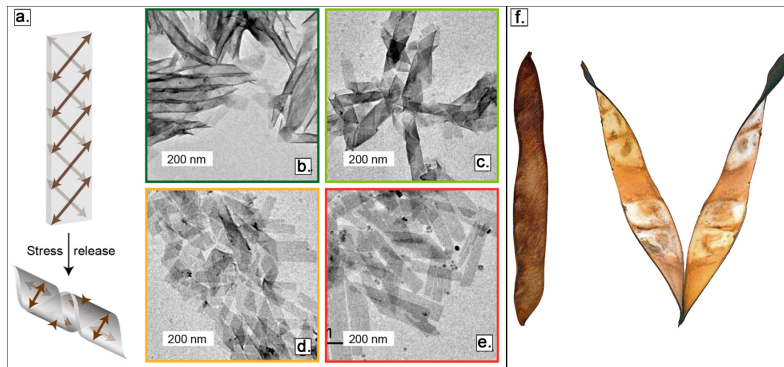


Figure 1.14 – (a.) Scheme of a NPL which undergoes a spontaneous folding to release stress imposed on its surfaces, symbolized by brown arrows - TEM images of 3ML-CdSe capped with (b.) oleic acid, (c.) chloride, (d.) bromide, (e.) iodide, from [69] - (f.) Closed and open seed pods, from [78].

1.3.4 Ligand-induced surface stress effects on the optical properties of NPL

If changing the ligand may change the curvature of the nano-object, it may also change its optical properties. Concerning CdTe nanosheets previously described [7], their folding occurs along a red shift of the excitonic transitions, due to a thickness increase of two additional sulfur planes and strain appearance under thiol attachment, whereas concerning CdSe NPL previously described [69], their unfolding occurs along an increase in the PLQY of up to 70% as a result of a better surface passivation of the NPL with halide ligands.

Antanovitch et al. reported a spectral shift directly linked to the structural change of CdSe NPL, after the exchange of native oleic acid ligand by hexadecanethiol or hexadecylphosphonic acid [79]. Again, ligand exchange leads to the onset of a strain that induces a tetragonal deformation of the NPL, i.e. a shrinkage in their lateral direction and an expansion in their thickness direction (Figure 1.15). Surface ligands thus directly affect the crystalline structure of the NPL and red-shift their excitonic band gap for up to 240 meV.

The interplay between ligand and induced surface stress (and thus curvature of nano-objects) opens a new way to tune the optical and even chiroptical properties of 2D-nanomaterials.

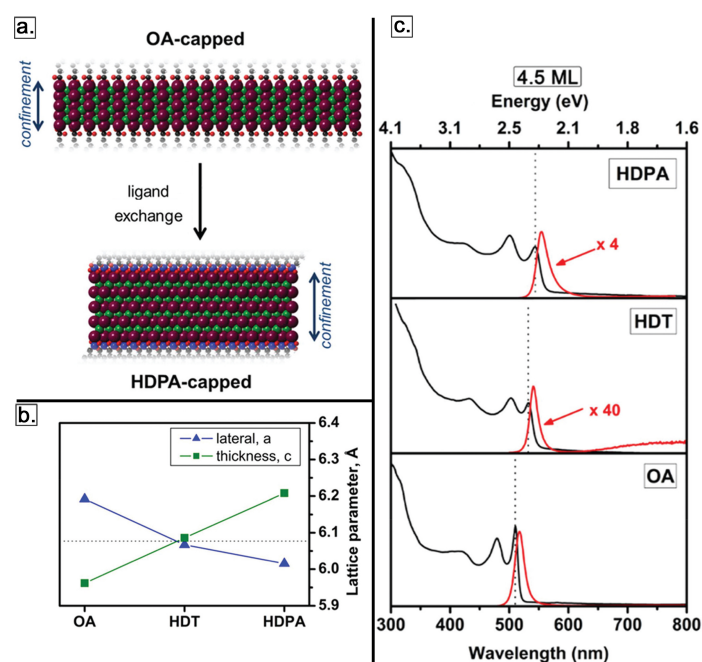


Figure 1.15 – a. Scheme of lattice transformation on 4ML-CdSe NPL upon ligand exchange of oleic acid (OA) by hexadecylphosphonic acid (HDPa) - b. Variation of lattice parameters of 4ML-CdSe NPL capped with OA, HDPa or hexadecanethiol (HDT) - c. Evolution of absorption and photoluminescence of 4ML-CdSe NPL with the surface ligand, from [79].

1.3.5 Shape effect on the chiroptical properties of NPL

In much general terms, focusing on the resulting curvature and morphology of nano-objects is crucial to understand, predict or even design these optical or chiroptical properties.

Compared to chiral molecules, chiral semiconductor nanocrystals interact with a circularly polarized light with a much stronger dissymmetry as they are composed of a large number of heavier atoms that interact stronger with light. As a consequence, their optical activity can be up to a thousand times higher than the one of chiral molecules.

Baimuratov, Tepliakov et al. have thus determined the origin of chirality in tapered CdSe nanoscrolls and its dependence towards the nature of the nanomaterial and its dimensions [80, 81]. Chiral nanoscrolls were modeled by taking into account their non-uniform rolling in terms of length and radius which make them chiral. This modeling allows to analytically calculate the intraband and interband rotatory strengths and the dissymmetry factors of optical transitions. As a result, the circular dichroism (CD) spectra are predicted [81] (Figure 1.16). The authors demonstrate the CD of nanoscroll is independent of the lateral size in the direction of winding and therefore is unaffected by the rolling up pattern of the nanoplatelet. Moreover, they succeed in explaining through this modeling the experimental redshift observed between the absorption and photoluminescence properties of CdSe nanoscroll towards the ones of regularly-flat dimensions-like CdSe nanoplatelets.

In the same manner, a theoretical model was established on the base of Rosenfeld's theory in order to predict the CD spectrum of semiconductor nanosprings [82]. It was theoretically predicted that CD signal of nanosprings can be dynamically tune in

sign and magnitude according to the strain (stretching or compression) applied on it (Figure 1.17).

This remarkable dynamic control of optical and chiroptical properties linked to the conformational control of the nano-object paves the way to new chiral optomechanical applications.

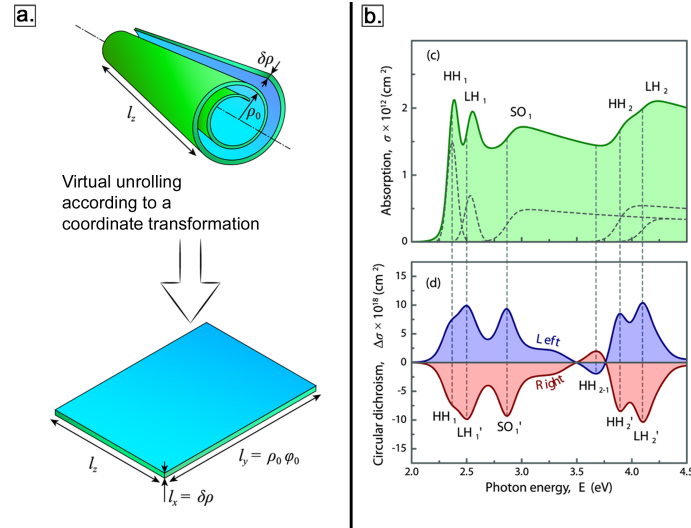


Figure 1.16 – (a.) Virtual unrolling of tapered nanoscroll into flat but topologically distorted NPL by a coordinate replacement and (b.) Absorption spectrum and CD spectra of the two optical isomers of the nanoscroll. Dashed curves in absorption spectrum feature the distinctive absorption bands of the transitions with the same quantum number of electron and hole. From [80].

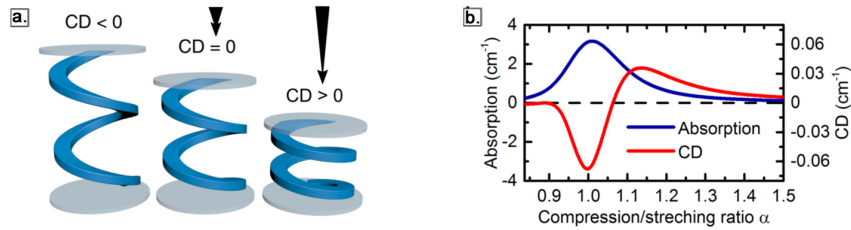


Figure 1.17 – (a.) Compression or stretching of CdSe nanosprings modifies their (b.) absorption and CD peaks at 260 meV, as well as the entire absorption, CD, and dissymmetry factor spectra. From [82].

1.4 Assemblies of colloidal nanoplatelets

The self-assembly of NPL can be done either in solution, possibly followed by a deposition of the large structures onto a substrate, or directly during particle deposition onto a substrate. Once deposited, we distinguish NPL assembled either side-by-side with their planes parallel to the substrate (face-down assemblies) or stacked face to face with their edge in contact with the substrate (edge-up assemblies) (Figure 1.19).

The main aim in organizing nanoparticles in a larger structure is to forge new collective properties from individual ones (e.g. size-dependent optical properties) through short-range interactions (such as exciton transfer). In order to design such assemblies, the interactions between particles and their medium are to be understood and tuned in an appropriate way. From this basis, the self-assembly of NPL can be reached using different experimental methods - e.g. using a liquid-liquid interface, directly in solution, or even by using an inkjet printing technique to create face-down assemblies as reported for instance on CdSe/CdS NPL [83] - that we will describe in a second time, before discussing the optical features reported for these assemblies.

1.4.1 Colloidal stability and interactions in solution

In order to understand how self-assembly emerges from a nanoparticle dispersion, one has to focus on the different kinds of interactions between particles in solution [84]. The most important that may drive NPL assemblies are: electrostatic interactions between nanoparticles, van der Waals forces (Keesom dipole-dipole interactions and London dispersion forces), surfactant layer interactions (surface ligand-solvent interactions, interpenetration of ligands chains, steric repulsions) and depletion interactions (i.e. the osmotic and attractive force between two colloids. This force results from the depletion of polymers or small micelles present in the solution and initially positioned between the two colloids in approach).

The classical colloidal theories developed for microparticles, such as the Derjaguin-Landau-Verwey-Overbeek (DLVO) theory, fail to describe colloidal stability of nanoparticles as several fundamental assumptions are not valid at this scale [85]. Above all, continuum approximations in the DLVO theory can not be satisfied as the sizes of surface ligand, solvent molecules and nanoparticles are within one order of magnitude of each others. The hypothesis of additivity of nanoparticle interactions to give a mean force potential for the interaction between two nanoparticles can therefore not be used, as these interactions are strongly interdependent in the case of nanoparticles. Particles interactions that drive self-assembly and colloidal stability must then be treated using large-scale molecular dynamics.

A first parameter that determines the colloidal stability of nanoparticles is their ligand shell and ligand density. *Widmer et al.* show the ligand monolayer is a crucial parameter that strongly mediates the interactions between inorganic nanoparticles, and that these interactions can be switched from repulsive to attractive in solution. By modelling CdS nanorods passivated with octadecyl ligands in n-hexane [86], the authors show the ligand shell undergoes a temperature-dependent order-disorder transition. At low temperature (300 K) a strong ligand ordering is modelled along an alignment of solvent molecules into layers nearby the ordered ligands (Figure 1.18). This compact ligand shell occupies less volume than a disordered situation and permits the rods to approach more closely and thus to self-assemble. The van der Waals forces are such that effective attractions between rods are predicted. In contrast, when the temperature is raised above 340 K, these interactions turn to be repulsive as a consequence of entropic repulsions between ligand chains: the interpenetration

of ligand shells from two rods reduces the number of free conformations possible, thus reducing entropy and leading to a global repulsion between rods.

The density of surface ligand and the facet dimensions affect the arrangement of surrounding solvent molecules and the interactions between rods: three ordered states are reported, differing in the manner ligands are packed together and resulting in different ligand shell thicknesses and ligand-solvent interface [87]. Intercapillary forces can then be dominated by microscopic factors, confirming that the description of nanoscale systems with continuous variables is inadequate.

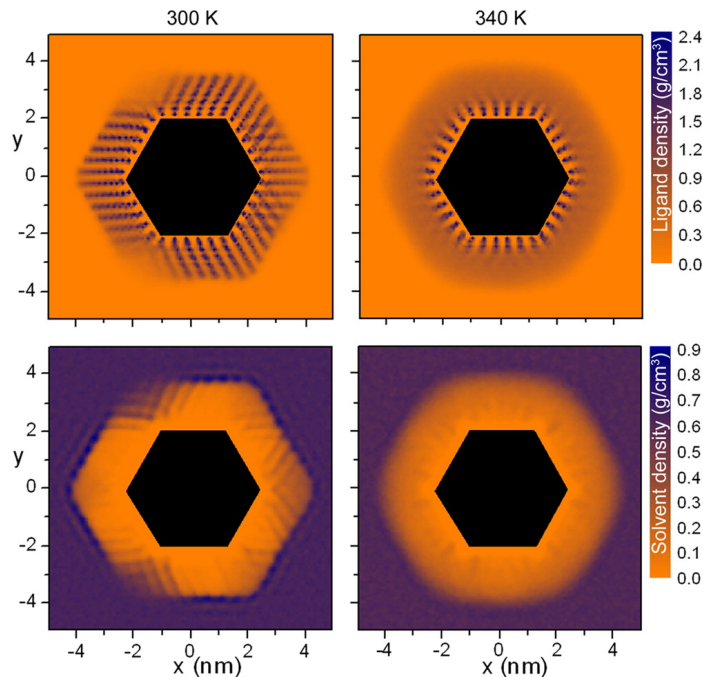


Figure 1.18 – Ligand density (top) and solvent density (bottom) around CdS core of isolated nanorods in hexane at 300 K (left) and 340 K (right). x and y scales are in nanometers, contour scale in g/cm^3 . The black hexagon indicates the position of the CdS core. Ligands order at low temperature, making the ligand-solvent interface more sharply and aligning the solvent molecules into layers: self-assembly between two rods is then favoured in this configuration. At higher temperature, the decrease in ligand ordering create entropic repulsions between ligand chains and disfavoured self-assembly. From [86].

The colloidal stability of nanoparticles also depends on the nature of the surface ligand used (functional group or carbon chain length) and their presence in a free form in solution [88]. *Jana et al.* show by SAXS that CdSe NPL capped with native oleic acid (OA) in a nonpolar solvent flocculate on a time scale ranging from minutes to hour and undergo a face-to-face stacking [89]. This stacking potentially originates from depletion attractions whose strength might be dependent on the surface ligand layer density [90]. The colloidal stability of the solution is reached for an optimum in OA concentration. The NPL concentration and the nature and the chain length of the ligands impact also the stability. For instance, exchanging native OA by a polystyrene with a carboxylic end group increases the stability of the dispersion [89], as the ligand carbon chain gets more affinity with the apolar solvent.

By exchanging surface native OA by alkylphosphonic acid at the surface of NPL, a face-to-face stacking is also observed whose length is dependent of the concentration of alkylphosphonic acid and the reaction time [91]. This stacking is explained

by strong van der Waals interactions that may occur between alkyl chains brushes on the surface of neighbouring NPL. On the contrary, a treatment with cadmium acetate of the OA-capped NPL allows a gain in colloidal stability, as acetate might replace and remove oleate surface ligand: van der Waals interactions between ligands that usually stabilize NPL stacks decrease in number and probability [91] and an increase in the conformational degree of freedom of the ligands allows a greater steric repulsion between platelets. As a result, the assembly of NPL is limited and their colloidal stability enhanced.

Surprisingly, if increasing the core size of particles leads to a decrease in colloidal stability, increasing the ligand length may either increase or decrease it depending on the size of the particle, as it was proven for gold and cadmium selenide nanoparticles passivated by alkanethiols [92, 93]. For large particles, agglomeration is dominated by van der Waals attractions. An increased ligand length results in an increased colloidal stability by extending the range of repulsion between the disordered ligand shells and reducing van der Waals attractions between cores more distant from each other. However, for small particles whose attraction originates from their ligand shell interactions, an increased ligand length results in a decreased colloidal stability as long ligands order in a way that favours agglomeration^g.

One might note the situation is different according to the shape of the nanoparticles: if coating large nanospheres with a long ligand may keep them separated far enough so that van der Waals forces are negligible (thus increasing the colloidal stability), it may not be the case for nanoplatelets. In this case, increasing the number and/or the length of ligands might result in their alignment at the surface into a crystalline form: this loss of entropy associated with the fact that no solvent molecules or reagents can interact with this ligand barrier could be responsible of a loss of colloidal stability and reactivity [90]. Moreover, van der Waals attractions between ligand layers of NPL might be more effective, inducing stacking [90].

The solvent has a role in the agglomeration of nanoparticles. It was shown that the agglomeration temperature of gold or cadmium selenide nanoparticles increases with the increase of the solvent chain length, according to enthalpic and entropic considerations [94] (i.e. the colloidal stability decreases as the length of the alkane solvent approached the one of the ligand tail, a result opposite to the well-known principle of "like dissolves like").

1.4.2 Liquid-liquid interfacial assemblies

A first way to perform assemblies of nanoparticles relies on the use of a liquid-liquid interface, as schematically illustrated in the left of Figure 1.19. This method was firstly employed for co-assembly of $\text{Fe}_3\text{O}_4/\text{FePt}$ nanocrystals [95] before being transposed for CdSe/CdZnS core/shell NPL [96] or CdSe core-only NPL [97]. In this last case, a small amount of CdSe NPL in hexane is dropped on a surface of diethylene glycol (DEG). After evaporation of hexane, a self-assembled monolayer of CdSe NPL remains on the DEG surface which can be removed in order to retrieve the self-assembled film on another more appropriate substrate [97].

By tuning the liquid-liquid interfacial energy thanks to the addition of oleic acid (OA) in the DEG phase, it is possible to obtain either a face-down assembly (with high concentration of OA in DEG), or a edge-up assembly (with a low concentration of OA in DEG). Indeed, intermolecular forces and van der Waals interactions between the capping ligand of NPL (which is also OA and myristate) and the subphase molecules

^g. This is then contradictory with traditional colloids theories. Besides, the ordering depends also on the temperature: longer chains order at higher temperature than short chains.

are tuned and influence the self-assembly process: a large amount of OA increases the interaction potential between NPL and DEG, leading to face-down assemblies, whereas without or with only a small amount of OA, inter-NPL interaction potential remains higher and edge-up assemblies are observed.

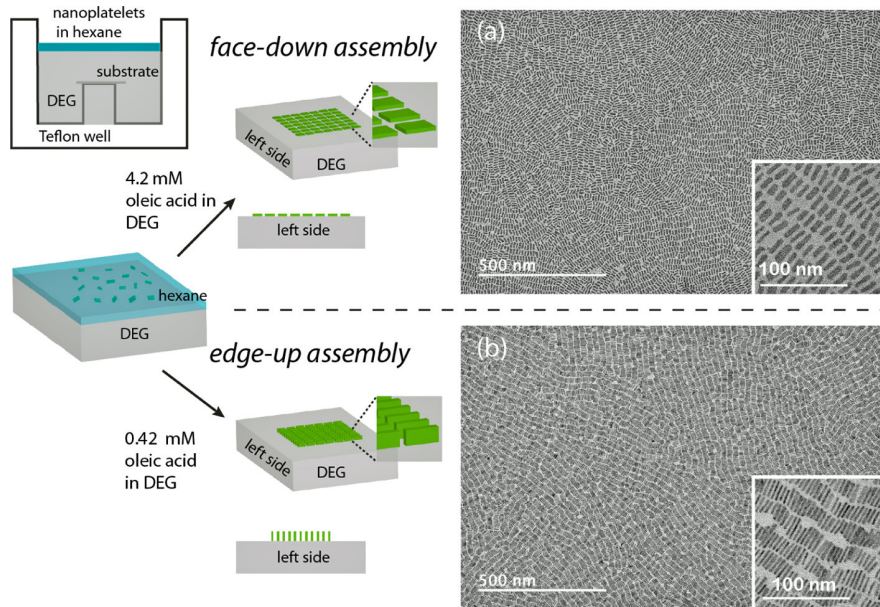


Figure 1.19 – Interfacial self-assembly of CdSe nanoplatelet monolayer films. Left panel: Illustration of the equipment used for self-assembly and schematic of the face-down and edge-up configurations. (a,b) TEM images of the face-down and edge-up assemblies, respectively. From [97]

Obtaining liquid-liquid interfacial assemblies depends on a lot of other parameters. Adjusting the polarity of the subphase with the one of the capping ligand of the NPL may lead preferentially to face-down assemblies, as it was proven when exchanging DEG with acetonitrile [98]. In the same way, the purity of NPL has a critical role: traces of ODE, used as the reaction solvent, favour inter-NPL interactions and then edge-up assemblies [98].

Finally, the orientation of the NPL within the assembly (i.e. face-down or edge-up configuration) can be controlled kinetically with the evaporation rate of the solvent used for the dispersion of NPL (Figure 1.20). Slow evaporation gives the system enough time to adopt the thermodynamically favoured edge-up configuration (energetically preferred toward a face-down configuration because of interpenetration of capping-ligand chains and hence energy gain in the edge-up configuration). In contrast, a fast evaporation kinetically traps the NPL in a face-down configuration [98].

The temperature has also a role in the assembly's configuration: a decrease in temperature reduces the evaporation rate of the NPL dispersion, leading preferentially to an edge-up configuration (Figure 1.20).

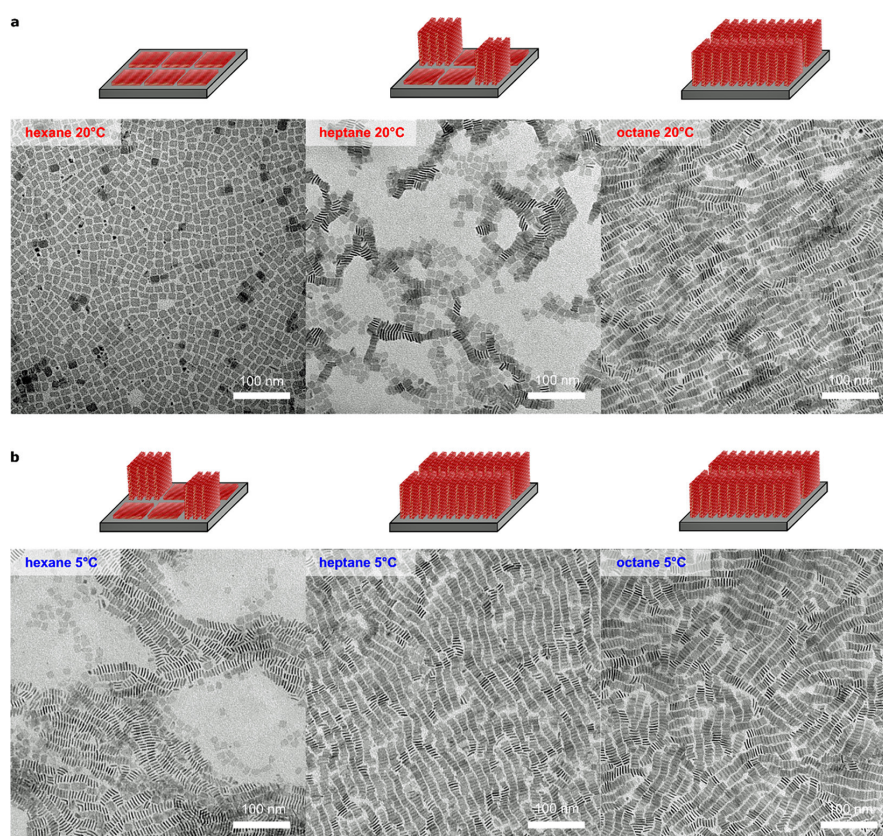


Figure 1.20 – Evaporation driven self-assembly of 4ML-CdSe NPL using a liquid-liquid interface. (a) TEM images illustrating the change of the dispersing solvent of the NPL on the assembly configuration: While reducing the vapor pressure (from hexane to heptane and octane at 20°C), the assembly configuration is tuned from a face-down (left) to an edge-up (right) configuration by way of a mixture of both (middle). (b) TEM images of assemblies realised at 5°C: edge-up assemblies are obtained in all cases. From [98].

1.4.3 Assemblies in solution

NPL assemblies (mainly edge-up assemblies) can be realized directly in colloidal solution on which we apply an external perturbation. Such a perturbation can be the addition of a non-solvent (typically ethanol) that destabilizes the colloidal solution. Needles of 10^6 square 4ML-CdSe NPL stacked face-to-face are obtained in this way with a length that can reach several micrometers [48]. In that case, ethanol molecules replace a part of the oleic acid at the surface of the NPL and therefore reduce the steric repulsion between NPL that can approach each other more closely and stack into superstructures. As an antisolvent, ethanol also favours the interdigitation of ligand brushes to reduce the surface energy of NPL, engendering the stacking of NPL.

A second kind of perturbation consists in the addition of a free surfactant in the dispersion which might exchange with the native capping ligand of the NPL or act as a depleting agent. Edge-up assemblies of square 4ML-CdSe NPL (Figure 1.21) are obtained by addition of a fixed amount of oleic acid into the colloidal suspension, followed by a slow drying and a redispersion [44]. The more OA added, the longer the length of CdSe NPL threads. The underlying mechanism behind this kind of assembly is comparable to a living polymerization mechanism and results from pairwise attractive interactions between NPL. As the thread length is dependent on the quantity of OA, this interaction might be a depletion interaction exerted by free OA molecules on the NPL.

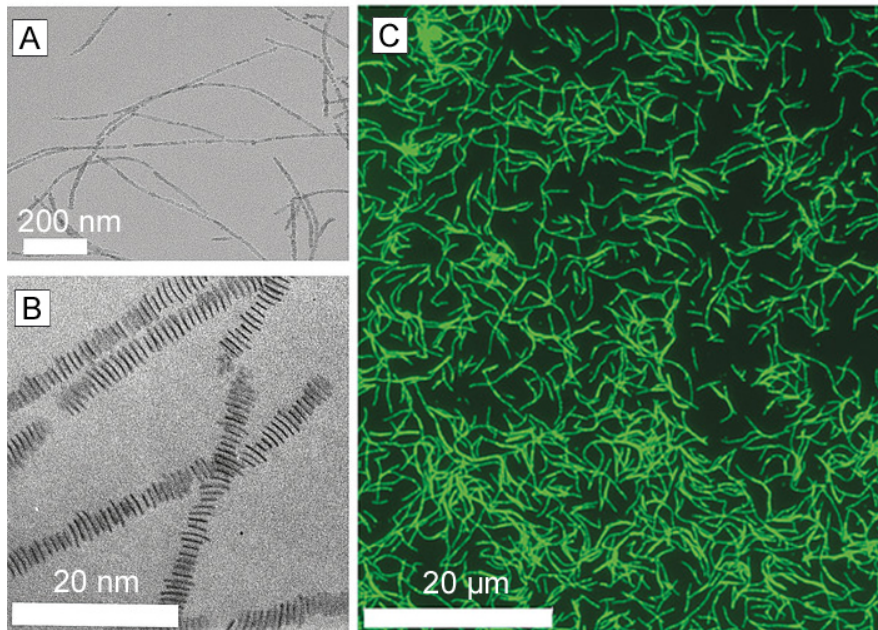


Figure 1.21 – Self-assembly of 4ML-CdSe NPL in solution. (A,B) TEM images of threads of face-to-face stacked CdSe NPL. (C) Fluorescence microscopy images of the same threads deposited from solution on a cover slip. From [44].

By injecting OA at regular intervals during the evaporation of a 5ML-CdSe NPL hexane solution, twisted ribbons of stacked NPL are obtained (Figure 1.22) with a typical length ranging from 1 to 4 μm and a pitch of 400 nm [43]. Again, the amount of OA in the medium affects the average length of threads. We showed in the previous section that such NPL undergo a twist upon the addition of OA that induce stress on the NPL surface: due to their close packing inside the thread, a frustration occurs and prevents NPL to completely twist as they would do if they were isolated in solution. That leads to a twist of the overall threads, in a racemic way.

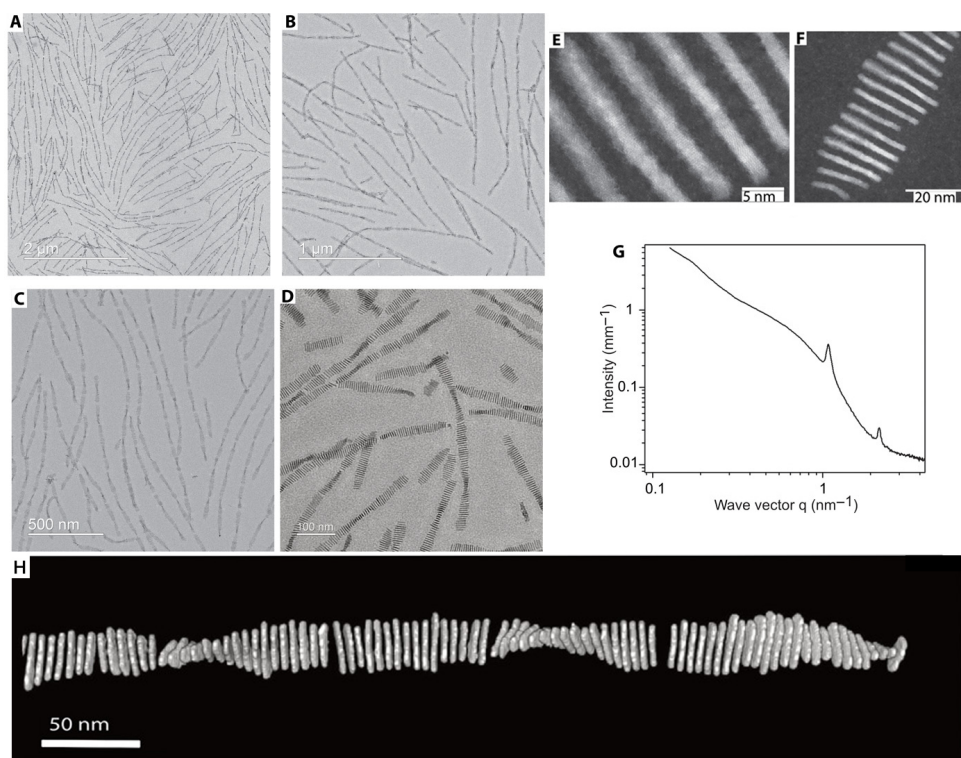


Figure 1.22 – (A to D) TEM images of twisted threads of CdSe NPL of various lengths. (E, F) HAADF-STEM images of the same threads. (G) SAXS pattern of a dispersion of twisted ribbons. The two scattering peaks, at 1.0075 and 2.0141 nm^{-1} , respectively, are the first and second orders of diffraction from the NPL stacking and give the stacking period $d = 5.84$ nm. From this period, it is deduced that there are around 70 NPLs within one pitch and that the mean rotation angle between two adjacent NPL is 5° . (H) Electron tomographic reconstruction of a twisted ribbon. From [43].

1.4.4 Optical properties of assembled nanoplatelets

Controlling the way NPL are oriented and coupled in space leads to novel and outstanding optical properties. For instance, the external quantum efficiency of LED of emissive entities can be improved by more than 50% if their transition dipole moment is parallel to the surface plane [97, 83]. Such a control is difficult to achieve with isotropic emitters such as QD for example, as the distribution of their transition dipole moment orientations is stochastic. However, the use of anisotropic nanomaterials such as NPL may help to achieve this goal. Indeed, transition dipole moments are aligned in the plane of NPL and their oriented assemblies in monolayer film exhibit long-range ordering of transition dipole moments [98].

For assemblies of CdSe NPL obtained from liquid-liquid interfacial assembly method [98, 97], both edge-up and face-down configurations preserve their dipole orientation over a large area of at least 5 mm². The face down configuration gets an in-plane isotropic dipole distribution whereas the edge-up configuration gets an out-of-plane anisotropic dipole distribution that gives rise to macroscopic linearly polarized light emission. Both configurations display a broader photoluminescence (PL) spectrum than isolated NPL in solution: this broadening is explained by an enhanced coupling strength in NPL assemblies. Indeed, the shorter the distance between NPL, the higher the electronic coupling. As the inter-NPL distance is shorter in the edge-up assembly than in the face-down assembly, this broadening is greater.

Moreover, this fact is also responsible of the higher photoconductivity in edge-up assemblies of NPL than the one of face-down assemblies. In both cases, the enhanced inter-NPL coupling strength leads to an enhanced inter-NPL charge transfer and an increased possibility of free charges generation by exciton dissociation compared to single isolated NPL, resulting in photoconductivity. That contrasts with isolated NPL that present only pure excitonic response.

Focusing on fluorescence, this difference in transition dipole orientation between the two assemblies configurations engenders differences in PL decay dynamics: slower decay times are reported for face-down assembly, as the exciton diffusion to quenching sites in these assemblies are less efficient. The light emitted is strongly polarized parallel to the nanoplatelet plane in the assembly [48]. Nevertheless, stacking between NPL increases exciton transfer and trapping, reducing the PL quantum yield and accelerating the transient fluorescence decay: this is corroborated with ultraefficient Homo-FRET (Förster Resonance Energy Transfer, see next paragraph) inside the assembly that can reach an efficiency of 99.9% [99], allowing excitons migration along long distance within the assembly before being trapped in quenching sites (i.e. nonemissive NPL) where they recombine nonradiatively (Figure 1.23.b.).

As regards temperature, whereas non-stacked NPL show their PL intensity increasing with the decrease of temperature, the PL intensity of stacked NPL slightly increase in contrary. Their PL decay time is also much shorter than the one of non-stacked NPL. These difference can again be explained by exciton trapping existing inside stacked NPL, that prevails over radiative recombination processes which is the only phenomenon existing for non-stacked NPL [100].

Finally, CdSe/CdZnS face-down assemblies were reported for their ability to display amplified spontaneous emission and are good candidate for lasing [96].

Another interesting properties with CdSe NPL relies on their capacity to realize ultra-fast Förster Resonance Energy Transfer (FRET) when organized in co-facial disposition [8, 46] (i.e. edge-up stacks of a hundred of nanometers). Hetero-FRET can take place from donors NPL with smaller thickness (e.g. 4ML-CdSe NPL) to acceptors with a larger thickness (5ML-CdSe NPL). The FRET efficiency is up to 60% thanks to near field dipole-dipole coupling as NPL of different thicknesses are stacked upon each others (Figure 1.23.a.). In the hypothesis of a perfect inter-stacking and an homogeneous mix between donors and acceptors (i.e. no experimental phase segregation that increases donors-acceptors distances), FRET efficiency may be able to reach 95% [46]. In that way NPL outperform QD in their capacity as FRET donors or acceptors: their near-perfect monodispersity and their extended plate geometry allow strong interactions between NPL and enhance FRET.

This non-radiative energy transfer occurs on a picosecond timescale (6-23 ps) because of small inter-NPL distance and large acceptor area. FRET is then faster than Auger recombination (150-500 ps) that annihilates the excitons and reduces the performances of traditional QD based devices. Fast FRET broadens the application of NPL to optoelectronics from lasers to solar cells involving multiexcitonic processes. Strong homo-FRET [99] inside NPL assemblies (i.e. between NPL of a same thickness) could then be possible, as we will show in details in section 4.2.3 on page 99.

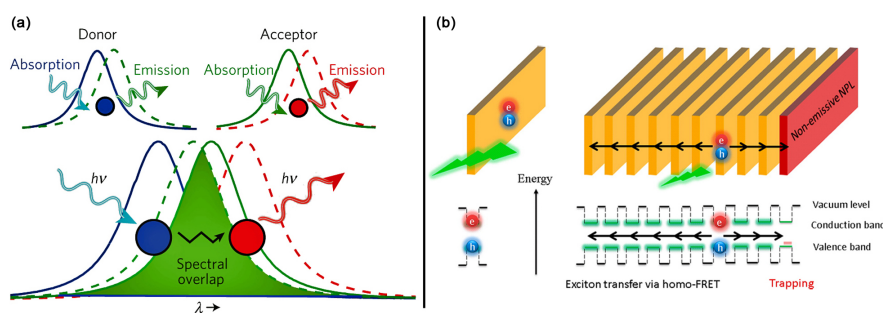


Figure 1.23 – (a) FRET principle. Among other factors, non-radiative FRET between donor (blue circle) and acceptor chromophores (red circle) requires non-zero spectral overlap between the donor emission spectrum and the acceptor absorption spectrum. The donor species absorbs at blue wavelengths (blue solid line) and emits in the green (green dashed line). It exhibits spectral overlap (shaded green) with an energy acceptor species that absorbs in the green (solid green line) and emits in the red (dashed red line). Absorption and emission spectra of 4ML- and 5ML-CdSe NPL reveal the potential for energy transfer from 4ML- to 5ML-NPL. From [8] - (b) Long range exciton hopping in stacked NPL through homo-FRET. The nonemissive NPL in the stack causes trapping of the excitons which recombine nonradiatively, resulting in a decrease on the overall quantum yield and on fluorescence lifetime. From [99].

Through this chapter, we have reviewed main concepts about the properties and growth of semiconducting 2D-nanomaterials, with an emphasis on CdSe NPL as a model system. We have focused on the role of surface ligands that can particularly tune the conformation and optical properties of semiconducting NPL as the result of surface stresses they induce. Finally, we have discussed about the forces ruling the colloidal stability and interactions between nanoparticles in solution and which can be tuned to self-assemble these nanoparticles into superstructures with interesting and innovative optical properties.

CHAPTER 2

Shape-control and formation mechanism of ultra-thin In_2S_3 nanoribbons

Chapter abstract

We report the synthesis of ultrathin indium sulfide nanoribbons (NR) from indium chloride and sulfur in oleylamine, using a simple and fast solvothermal method. The dimensions of these nano-objects are determined from TEM observations: the nanoribbons are (8.7 ± 0.1) nm in width, (0.71 ± 0.04) nm in thickness and up to several micrometers in length.

The nanoribbons composition is determined by Rutherford backscattering spectrometry (RBS) and X-Ray Photoelectron Spectroscopy (XPS). Their crystallographic structure is elucidated by X-Ray diffraction and high-resolution dark-field scanning TEM. Nanoribbons are thus made of trigonal $P\bar{3}m1$ γ - In_2S_3 .

Depending only on the quantity of water introduced in the reaction medium, a shape tuning of these nano-objects can be realized, from hexagonal nanoplates in anhydrous conditions to long nanoribbons when indium precursor is hydrated. An optimization of the synthesis parameters is then realized. The formation mechanism of these nano-objects is investigated by time-resolved in-situ synchrotron SAXS/WAXS.

Finally, colloidal stability of NR in different solvents is investigated by SAXS/WAXS and TEM. NR tend to form bundles in the majority of the solvents tested, except for the case of tetrahydrofuran that reveals to be an excellent solvent of redispersion for the NR.

Indium sulfide is an important wide band gap semiconductor material which bears potentially useful properties such as long term stability and low toxicity when compared to its cadmium or lead containing counter parts. It could have potential use in a variety of opto-electronic applications such as buffer in photovoltaics [101], in display devices and photodetectors [37, 102, 103, 104, 105] or water splitting [106].

We draw up in a first section of this chapter a brief state of the art around indium sulfide nanomaterials. In a second part, we present the solvothermal synthesis of ultrathin $\gamma\text{-In}_2\text{S}_3$ nanoribbons. In a third section, we show that the morphology of the as-synthesized In_2S_3 nano-objects can easily be controlled, from hexagonal nanoplates to long nanoribbons just by adding to the initial mixture of molecular precursors a fixed amount of water. We describe then the optimization of this new NR synthesis. In a last section, we discuss about the formation mechanism of NR and their bundling in colloidal solution.

2.1 A quick overlook on indium sulfide in literature

Research on indium sulfide colloidal nanoparticles has been active in the past years with several different morphologies and synthetic pathways explored. For example, *Park et al.* have reported the synthesis of In_2S_3 hexagonal nanoplates (Figure 2.1.a.) using InCl_3 and sulfur in oleylamine [37]. The same precursors were used to produce long nanotubes (Figure 2.1.c.) [107] while di-tert-butyl disulfide and indium acetylacetonate in oleylamine yield nanorods [108] (Figure 2.1.b.). Such $\beta\text{-In}_2\text{S}_3$ nanorods exhibit significant absorption in the UV and in the early visible region and photoluminescence.

The *Pradhan* group reported the synthesis of indium sulfide nanosheets (NS) obtained through the thermal decomposition of indium tris-diethyldithiocarbamate in hexadecylamine [76] (Figure 2.1.d.). Similar wrinkled NS have been observed to be transient intermediates towards smaller hexagonal In_2S_3 nanoplates when InCl_3 and thiourea are used as precursors in oleylamine [109].

Solvothermal syntheses have also been used to synthesize indium sulfide 2D nanoparticles, mainly with long chain amines as solvent. While indium chloride tetrahydrate and carbon disulfide react at 160°C for 24h in pyridine to yield long indium sulfide nanobelts [110] (Figure 2.1.h.), indium nitrate tetrahydrate and lauryl mercaptan react at 240°C for 24h in pyridine to yield indium sulfide nanotubes [111](Figure 2.1.e.). Both nano-objects presents photocatalytic performance in the degradation of organic pollutants.

Obtaining various shapes of indium sulfide nano-objects may result from other strategies than acting on precursor sources : *Ni et al.* got nanotubes from the self-assembling of ultrathin nanocoils synthesized from indium acetate and sulfur in octylamine [75, 74] (Figure 2.1.e., f.), whereas *Tian et al.* showed nanoflakes, nanoparticles or nanobelts can be obtained with the introduction of an appropriate and carefully chosen metallic ions in the initial mixture [112].

Finally, other materials with a different indium degree of oxidation can be obtained. For instance, InS material exist in four crystal systems (orthorhombic, monoclinic, cubic and tetragonal) where orthorhombic $Pn\bar{m}$ structure is predicted as the most stable one [113]. InS orthorhombic single crystal present an optical band gap of 2.09 eV alongside nonlinear refractive index and absorption coefficient [114]. 1D-InS nanomaterials are already reported in the form of wire or rod [115] whereas 2D-InS nanomaterials are obtained from a solvothermal synthesis between thioacetamide and indium metal in the resulting form of thin plates [116].

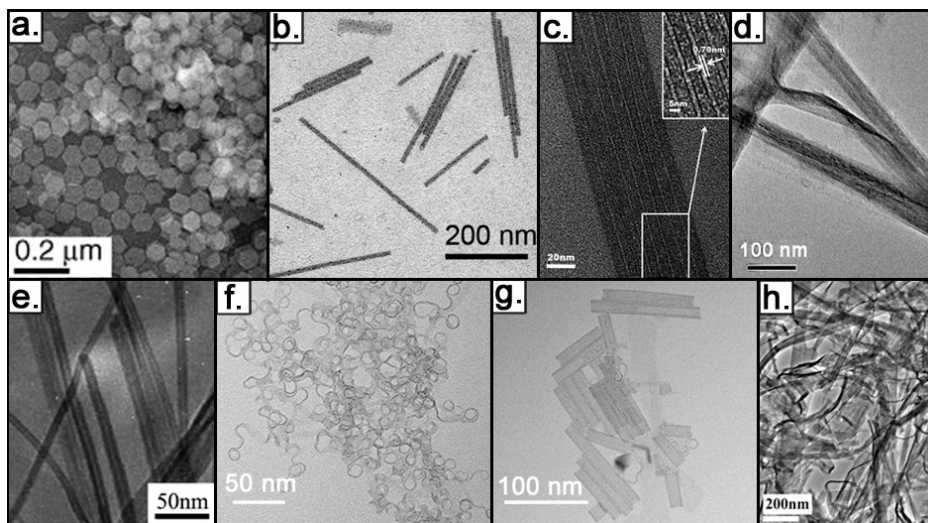


Figure 2.1 – TEM images of: (a.) 63 nm-hexagonal In_2S_3 nanoplates [37] - (b.) In_2S_3 nanorods [108] - (c.) In_2S_3 nanotubes, The inset shows a high-resolution TEM image of a nanotube with a wall thickness of 0.79 nm. [107] - (d.) In_2S_3 wrinkled sheets [76] - (e.) In_2S_3 nanotubes [111] - (f.) In_2S_3 nanocoils [75, 74] that assemble in (g.) single-walled nanotubes through oriented attachment [75] - (h.) In_2S_3 nanobelts [110].

Phase identification for indium sulfide has been ambiguous. Most of the reported syntheses are thought to yield In_2S_3 but definitive attribution of the crystal structure is often difficult because the X-ray diffraction pattern match the one of crystallographic databases only partially. These discrepancies were attributed to the anisotropy of the nanoparticles since reflections corresponding to small crystalline domains are expected to be broadened, as reflected in Scherrer's equation [117]. In the case of subnanometer dimensions, this broadening may be so important that these peaks might be experimentally difficult to observe.

In the Powder Diffraction Files of the International Centre for Diffraction Data (ICDD), four different In_2S_3 phases are reported. The cubic phase corresponding to the space group $Fd\bar{3}m$ ($n^\circ 227$) is often coined the α phase while the most common is the tetragonal β phase bearing the $I41/amd$ ($n^\circ 141$) space group. Two other phases with a trigonal crystal system have also been reported, one with a rhombohedral space group ($R\bar{3}c$) and the other with a hexagonal one ($P\bar{3}m1$). The latter is called the γ phase while the former the ϵ phase. *Pistor et al.* describe three different structures of In_2S_3 [118] (Figure 2.2): a low temperature tetragonal phase β , an intermediate temperature cubic phase α and a high temperature trigonal phase γ , also reported in [119]. In any case, the experimental distinction between tetragonal β and cubic α phases is difficult to make without high quality X-ray diffraction data.

We have to point out that an ambiguity exists on the designation of the different In_2S_3 phases [118]. Indeed, the low temperature cubic phase was initially coined α while the higher temperature tetragonal phase was called β . Later, it was shown that the initial report misidentified the low temperature phase as being cubic. In fact, the low temperature phase is tetragonal and a transition towards the cubic structure is observed as temperature increases. Hence some authors have renamed the cubic phase β for the names of the different phases to be consistent and follow the right alphabetical order as temperature increases. This has caused a lot of confusion. For instance, the cubic phase is named α in some files of the international crystallographic database and this notation is also present in publications. Here, we will stick with the notations of [118] and designate the different phases as described in the previous

paragraph.

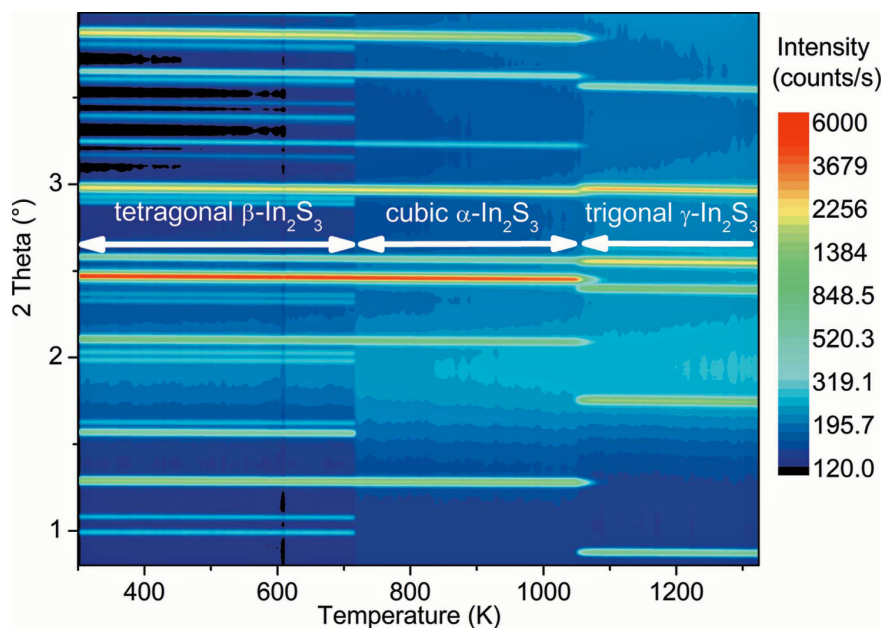


Figure 2.2 – Map of temperature-dependent X-ray diffractograms for In_2S_3 powder, from [118]. The colours indicate the XRD intensity in logarithmic scale (dark blue: low intensity, red: high density).

Finally, different values of optical band gaps are reported in the literature for In_2S_3 material, ranging from 1.65 eV to 3.7 eV [120, 121]. The band gap for $\beta\text{-In}_2\text{S}_3$ ranges generally from 2.0 to 2.54 eV according to different optical studies [103, 122], whereas the band gaps of $\alpha\text{-In}_2\text{S}_3$ and $\gamma\text{-In}_2\text{S}_3$ are respectively of 2.45 eV and 2.53 eV according to reference [122]. Photoluminescence is reported for $\beta\text{-In}_2\text{S}_3$ with an emission peak at 597 nm (2.08 eV) under excitation at 400 nm [103].

2.2 Synthesis of indium sulfide nanoribbons

The In_2S_3 NR reported in this work are synthesized from molecular precursors by a fast and simple solvothermal method. Anhydrous indium (III) chloride is mixed with sulfur powder, water and oleylamine in a Teflon-lined autoclave (Figure 2.3 - See the experimental section for more details). The autoclave is then sealed and heated two hours at 215°C in an oven. The resulting yellow viscous product is then washed from oleylamine with ethanol and toluene.

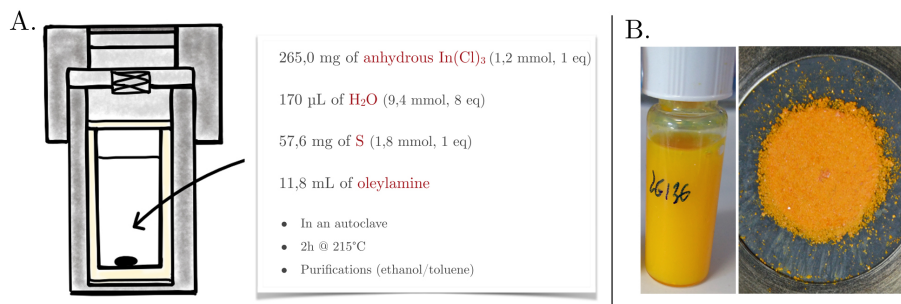


Figure 2.3 – (a.). Scheme of the experimental conditions - (b.). Left: Colloidal solution of nanoribbons dispersed in toluene, Right: Nanoribbons in the powder form.

Transmission Electron Microscopy (TEM) images and high-angle annular dark-field (HAADF) scanning TEM images (Fig. 2.4) of these NR show highly anisotropic objects which can reach several micrometers in length for (8.7 ± 0.1) nm in width and (0.71 ± 0.04) nm in thickness. These ultrathin NR have regular rectangular shapes that vary only in length, in average of (1162 ± 44) nm after measurements of an ensemble of 500 NR^a. That highlights a very large aspect ratio of respectively 10 and 100 between the length of NR and their width compared to their thickness. The uniform thickness of the NR is also clearly revealed by the uniform intensity contrast in TEM images of NR lying flat on the grid (Figure 2.4.a.).

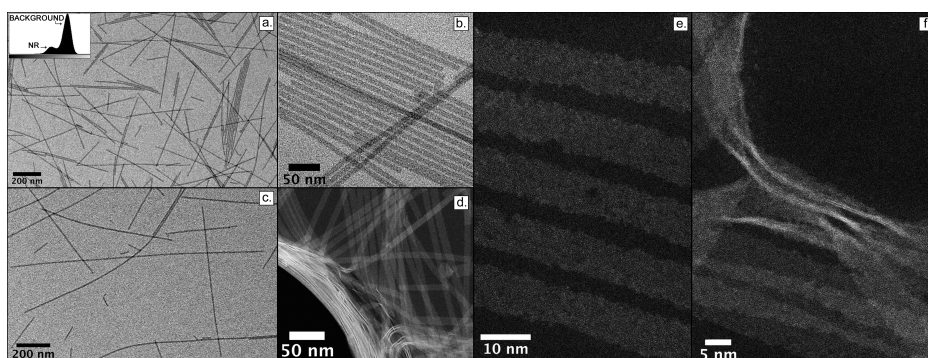


Figure 2.4 – (a., b., c.) TEM images of In_2S_3 NR lying flat. Insert in (a.) is a gray scale histogram of the underlying image, showing the uniform thickness of the NR as only two peaks are seen (background and NR) - (d., e., f.) HAADF-STEM images of the same NR, viewed both lying flat and on edge, acquired with the help of Benoit Mahler from the Institut Lumière Matière of Lyon.

^a. As regards uncertainties: The global uncertainty given for each dimension is $U = 2 \cdot \sqrt{U_A^2 + U_B^2}$ with $U_A = \frac{\sigma}{\sqrt{n}}$ the A-type uncertainty (σ is the square deviation of the statistical series and n the number of measurements, generally more than a hundred to be statistically relevant). B-type uncertainties are given by U_B which is evaluated on the repetition of a same measurement 50 times.

2.3 Composition and crystallographic structure

In order to identify the exact composition of the as-synthesized NR, we carried on Rutherford Backscattering Spectrometry (RBS) experiments.

About Rutherford Backscattering Spectrometry

RBS is a key-technique to access to the elemental composition of a sample. This technique has already been used for CdSe nanoplatelets [123] and is known to yield reliable and accurate results for the composition of inorganic materials, in particular for heavy elements.

The powder material is irradiated by α -particles which are backscattered after interaction with the nucleus of the atoms composing the material. The energy of each backscattered ion is proportional to the initial energy of the α -particles by a factor k named kinematical factor, which depends of the atomic number of the chemical element. This energy is also dependent on the length of penetration of the ions inside the sample. A simulation program [124] allows then to calculate the distribution of concentration in chemical elements on the sample.

For instance, Figure 2.5 shows RBS spectrum which exhibits two distinct plateaus: each plateau is associated with one chemical element, here sulfur and indium. The length of each plateau is correlated to the energy of ions which are backscattered by a same chemical element but at different depths (the energy of the backscattered ion decreases as it is backscattered deeper in the material). The relative height between plateaus gives information on the composition in chemical elements of the sample. Thus, simulations and fitting of the RBS experimental datas in Figure 2.5 assess that purified NR are composed at $(40 \pm 1) \%$ of indium and at $(60 \pm 1) \%$ of sulfur, thus determining the empiric formula of the NR as In_2S_3 .

This technique is very accurate. A peculiar attention has to be taken into account concerning the purification of the sample before any RBS analyses. Indeed, the NR composition can be biased if few precursors such as indium chloride or sulfur powder are still present in the final sample.

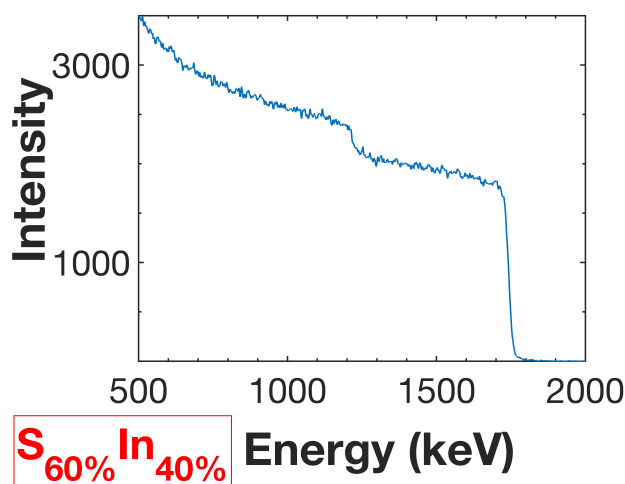


Figure 2.5 – RBS spectrum for In_2S_3 NR: the experimental data are fitted in order to obtain the chemical composition of the sample, written below the spectrum. The results leads to In_2S_3 empiric formula for NR. The spectrum and its interpretation were realized with the help of Bruno Canut from the Institute of Nanotechnologies of Lyon.

RBS analyses assess that NR are composed at (60 ± 1) % of sulfur and (40 ± 1) % of indium. The stoichiometric ratio between indium and sulfur is thus of 2:3, so that the empirical formula of the NR is In_2S_3 .

To get further insights on the composition of the NR we performed X-Ray diffraction (XRD) experiments and compared the pattern with computed diffraction patterns of indium sulfide (Figure 2.6).

We observe a broad peak at 19.5° , a low intensity peak at 24.6° , an intense thin peak at 27.3° followed by two broader reflections at 30.5° and 31.8° . Finally, we observe a triplet of peaks with an intense thin one centred at 48° and two lower intensity peaks situated at $\pm 1^\circ$ (i.e. 47° and 49°) from the center peak. A last, low intensity peaks can be seen at 56.1° , 75.2° and 78.3° .

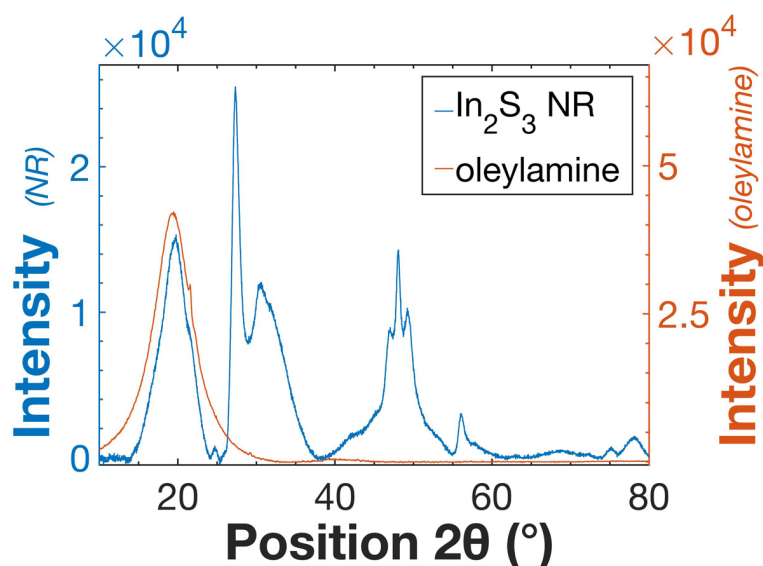


Figure 2.6 – X-ray diffractogram of In_2S_3 NR (blue) along the one of oleylamine (red) from which originates the peak at 19.5° .

Very similar diffraction patterns have been reported in several publications [125, 108, 37, 126, 104, 109, 127]. However, the indexation of the peaks were made differently. The thin peak at 27.3° has been attributed to the (311) reflection of the β phase in references [127, 126, 110, 108] but to the (109) peak of the same phase by references [37, 104] while references [109, 125] assign this peak to the (110) reflection of the ϵ phase. These seemingly contradictory findings can be explained by the fact that the α cubic phase has been relabelled by some authors the β phase because it appears at a higher temperature.

The peak at 19.5° has previously been attributed to impurities [104]. This is consistent with our observation of batch to batch variability in the respective intensity of this peak with respect to the others. In order to confirm and determine the origin of this peak, we acquired the X-ray diffractograms of indium chloride, sulfur powder, a mixture of indium chloride in oleylamine and oleylamine alone. We concluded oleylamine is responsible for the presence of this peak (Figure 2.6). This assertion is surprising as such a solution of organic molecules is not supposed to give a X-ray diffraction pattern. We suggest then the following interpretation. We observed that yellow-transparent oleylamine undergoes a transformation into a beige slurry when exposed few minutes to the air: we attribute this transformation to the carbonation

of oleylamine into the corresponding carbamic acid. We think that reaction might occur along a spatial rearrangement and alignment of the carbamic acid molecules in the same manner as in a lipid bilayer, as a result of energy maximization of the overall solution. This organization of molecules would then be able to give diffraction under a X-ray beam. Of course further investigations are needed to confirm that phenomenon, and in the first place infrared spectroscopy to confirm the carbonatation reaction.

In order to take into account the broadening of the peaks where the extension is smaller than the others, we simulated the X-ray diffraction patterns of different atomic models of In_2S_3 NR. Briefly, we generate an atomic model of In_2S_3 nanoparticle whose dimensions match the ones we observe with electron microscopy and compute the diffraction pattern from the atomic positions using the Debye formula. The orientation of the edges and the crystallographic phase is changed in order to evaluate their influence on the X-ray diffractogram. These simulations have been performed with the help of Benjamin Abécassis.

Simulating X-ray diffractograms of NR with known geometry and varying crystalline structures can be useful to assign the right structure. The width of the peaks will, in the simulations as well as experimentally, depend on the orientation of the crystalline lattice with respect to the edges of the NR. For example, let us consider a ribbon with dimensions $10 \times 100 \times 1$ nm along the three a, b, c principal crystallographic axes. All the (hkl) reflections with h or k different of 0 will be thin since the order along the a and b directions is reasonably long range. Similarly, (00l) reflections will be very broad or even not visible since one or a few unit cells are present along the c principal direction [117]. Thus if two thin peaks are present in the diffractogram they must be both of the (hk0) type.

We have simulated in total three different structures which are likely to match the experimental patterns: the α , β and γ phases. We observe that the peak at 19.5° is absent in all the theoretical models which confirm it is caused by impurities. An intense peak is visible around 27° in all the simulated structures but it can correspond to different reflections depending on the symmetry of the phase.

As electron microscopy experiments showed the presence of a ternary symmetry axis in the structure in the direction parallel to the thickness (Figure 2.7.a.), the crystallographic structure of the NR must contain this element of symmetry. Among the three different phases, the only phases where a ternary symmetry axis is present are the α and γ phase. Moreover, the likelihood that our nanocrystals belong to the β structure is decreased as it presents two intense peaks at 33.2° and 43.5° which are not present in the experimental diffractogram of NR.

To discriminate between α and γ possibilities, we compared crystallographic models from Crystal Maker and experimental observations from HAADF-STEM images (Figure 2.7). From these comparisons we have retained the trigonal $\gamma\text{-In}_2\text{S}_3$ $P\bar{3}m1$ structure to be the good crystallographic structure of the NR, with a thickness along the [001] direction.

Let us first consider NR that lies flat on TEM grids (Figures 2.4.d., 2.4.e., 2.4.f. and 2.7.a., 2.7.c.). Atoms are aligned in rows oriented at $(58 \pm 3)^\circ$ ^b from the edge of the NR (measurement n°3 in Figure 2.7.a.). Inside a row, atoms are distant from (0.39 ± 0.01) nm^c whereas two atoms vertically aligned (from different rows) are distant of (0.40 ± 0.01) nm^d (respectively measurements n°1 and 2 in Figure 2.7.a.).

b. averaged from 55 measurements

c. averaged from 155 measurements

d. averaged from 174 measurements

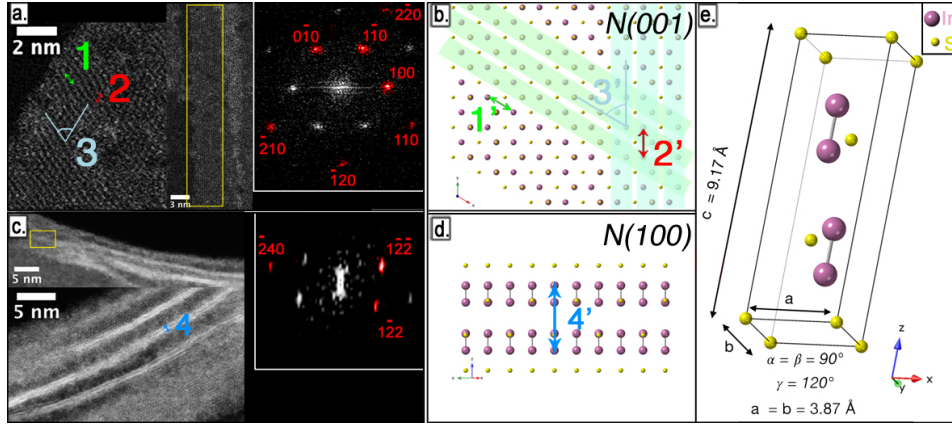


Figure 2.7 – (a., b.) HAADF-STEM images of In_2S_3 NR lying respectively flat and on edge, acquired with the help of Benoit Mahler from the ILM Lyon. Inserts are Fourier transforms of yellow boxes. These patterns match with computed electron diffractograms of $\gamma\text{-In}_2\text{S}_3$ for an observation of the modelled structure respectively along the normal vectors of (001) and (100) planes - (b., d.) Modelling of $\gamma\text{-In}_2\text{S}_3$ NR with a thickness along the c -axis of a single unit cell length. The crystallographic model is viewed along the normal to the (001) (b.) or (100) (d.) planes. The different figures are measurements realized on HAADF-STEM images and modelled NR, and are discussed in the main text - (e.) Trigononal ($P\bar{3}m1$) $\gamma\text{-In}_2\text{S}_3$ unit-cell crystallographic representation, along with cell parameters.

Computed distances on modelled $\gamma\text{-In}_2\text{S}_3$ NR viewed along the normal vector of their (001) plane (i.e. simulation of a NR viewed lying flat, with its thickness along the c axis) are in good agreement with these experimental observations: atoms are aligned in row oriented at 60° from the edges, whereas in-row atoms and vertically-aligned atoms are distant from 0.38 nm (resp. measurements $n^\circ 3'$, $1'$ and $2'$ in Figure 2.7.b.).

Finally, having the thickness in the c -direction imposes to have a unit-cell thick NR. NR viewed in HAADF-STEM lying on their edge show a lamellar pattern of two superimposed layers: this structure is well reflected in modelled $\gamma\text{-In}_2\text{S}_3$ structure, strengthening the hypothesis of this structure to be the good experimental one for NR. The experimental thickness of this double layer ((0.71 ± 0.04) nm^e, measurement $n^\circ 4$ in Figure 2.7.c.) is close in value to the one given in our model (0.64 nm, measurement $n^\circ 4$ in Figure 2.7.d.).

Moreover, the theoretical diffractogram of the γ phase for a $100 \times 10 \times 1$ NPL is in agreement with the experimental one, as shown in Figure 2.8. The diffraction peak at 27° is attributed to the (010) reflection, whereas the peak at 47° is attributed to the (110) reflection. Finally, the peak at 55° is attributed to the (020) reflection.

e. averaged from 30 measurements

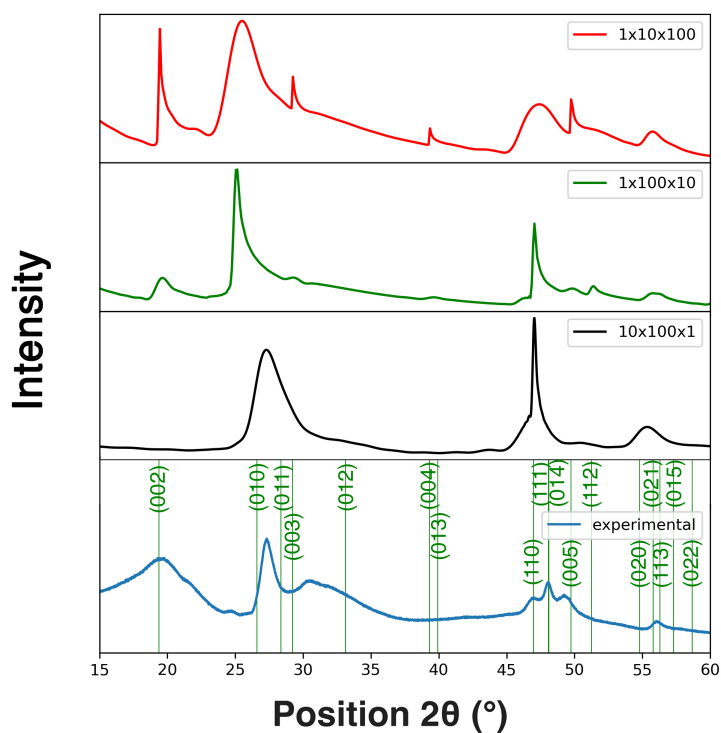


Figure 2.8 – X-ray diffractogram of In_2S_3 NR along computed ones for γ -trigonal In_2S_3 . We have firstly simulated NPL with the γ phase (green lines) and the theoretical diffractogram looks in agreement with the experimental one (blue curve), but the orientation needs to be sorted out. We thus generate NPL with a 1, 10, 100 aspect ratios in the three crystallographic orientations. Over those six possibilities, only three yield a different diffraction pattern since the a and b axis are equivalent. For example, the $1 \times 10 \times 100$ NPL and the $10 \times 1 \times 100$ NPL will yield the same diffraction pattern. These simulations and plots were realized by Benjamin Abécassis.

X-Ray Photoelectron Spectroscopy (XPS) was carried on NR to go further in the analytical description of the NR.

About X-Ray Photoelectron Spectroscopy (XPS)

XPS is a key technique to access to the atomic composition of a solid sample and to highlight which elements of a sample is linked to which others.

A X-ray radiation interacts with the surface of the sample, placed in a very high vacuum chamber: from this interaction, a core electron is extracted from the material and detected by the apparatus. Its ionization energy is function of the element from which it is extracted and also from the chemical environment of this element.

By knowing the energy of the X-ray photon and the kinetic energy of the detected photoelectron extracted from the material, it is possible by applying a conservation energy equation to determine the binding energy of this electron. This binding energy is tabulated for different elements in different environments (i.e. linked with different atoms). It is then possible to access to the elemental composition of the sample, as well as information on the bonds between elements.

In the framework of our study we use XPS in two purposes: the first one is to confirm RBS analyses and highlights if other light elements (as oxygen) are present in the sample. Actually, RBS is much more sensitive to heavy elements: for instance, if sulfides can be detected, it is not the case of oxides which could have been part of our samples. The second and main purpose is to determine the ligand density by knowing the proportion between indium and typical heteroelements of the surface ligands, such as oxygen (from ethanol ligands) or nitrogen (from oleylamine ligands).

XPS survey spectrum is available on Figure 2.9. Its interpretation gives the following atomic composition of the sample: C (65.9%), O (0.5%), S(18,6%), In (12,2%) and N (2,8%). The analysis was carried on two different spots, revealing a similar distribution in elements. Indium and sulfur are reported to be linked together, forming indium sulfide material as expected, with an atomic ratio between these elements of 1.52. This stoichiometry is consistent with the one obtained from RBS analysis and it confirms the empirical formula of In_2S_3 for the NR. Oxygen is involved in C-O bonds, proving it is solely part of ethanol molecules that may be grafted on the surface of the NR during the different purification steps. Nitrogen comes from oleylamine surface ligands. The composition of NR can then be written $\{\text{In}_2\text{S}_3[\text{oleylamine}]_{0.46}\}$. The NR coverage in amine is analogous to coverages reported for instance on wurtzite $\{\text{CdSe}[\text{n-octylamine}]_{0.53}\}$ quantum belts [128, 129].

Assuming the volume of one ribbon from $7.2 \times 10^6 \text{ \AA}^3$ (in compliance with statistical measurements done previously in TEM) and the volume of one unit-cell of $\gamma\text{-In}_2\text{S}_3$ of 118.5 \AA^3 , we may say one ribbon is made of 6.1×10^4 cells. Each crystallographic cells contain 4 indium atoms, leading to 2.4×10^5 indium atoms per NR. As the atomic ratio between indium and nitrogen is of 4.4, we can calculated the number of oleylamine molecules bonded to the NR surface (i.e. 5.6×10^4 molecules). The surface accessible for oleylamine molecule are of $2.0 \times 10^4 \text{ nm}^2$ (top plus bottom face planes of the NR), so that the oleylamine ligand density is of $2.3 \text{ molecules.nm}^{-2}$.

This ligand density is in the order of magnitude of other surface ligand densities already reported in the literature for nanomaterials, ranging from 0.5 to $5.5 \text{ ligands.nm}^{-2}$ [130, 15, 79, 87]. For instance, *Anderson et al.* determined by NMR the ligand density of $4.3 \text{ oleate.nm}^{-2}$ for PbS QD and $3.3 \text{ oleate.nm}^{-2}$ for CdSe QD [15]. *Fritzing et al.* reported a value for CdSe QD of $(4.6 \pm 0.4) \text{ oleate.nm}^{-2}$ [131]. With the same reasoning, ethanol ligand density is estimated at $0.5 \text{ molecules.nm}^{-2}$.

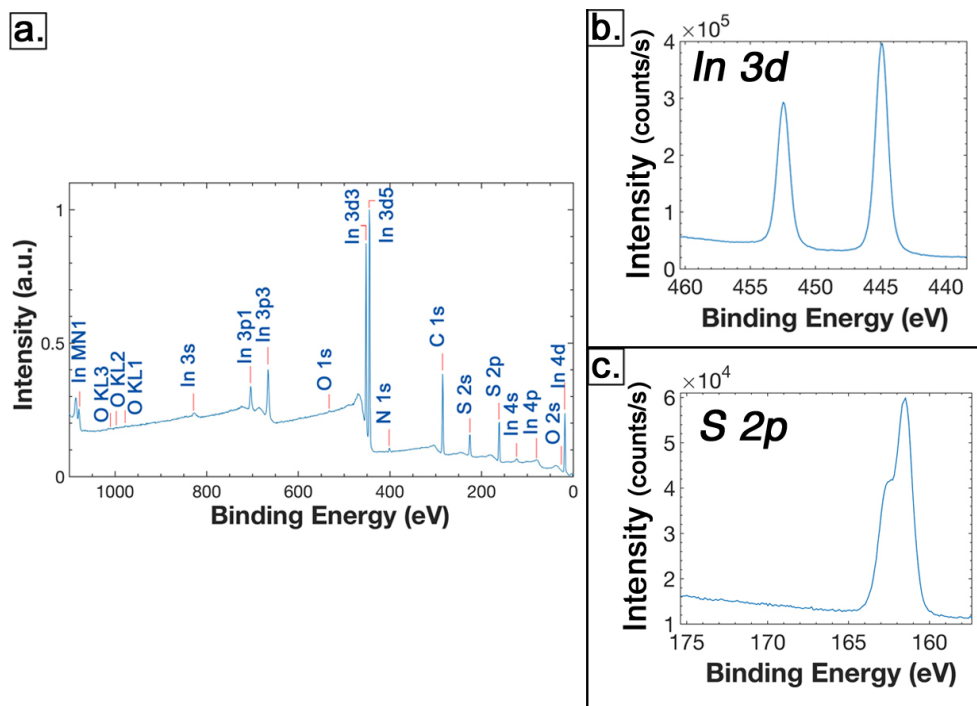


Figure 2.9 – XPS analyses: (a.) XPS patterns for survey of NR, proving the atomic presence of In(12.2%), S(18.6%), O(0.5%), C(65.9%), N(2.8%) - High-resolution spectra highlighting the presence of: (b.) In in the form of sulfide (peak centred at 444.7-444.9 eV), (c.) S in the form of sulfide (peak centred at 162.5 eV).

Finally, UV-visible absorption spectroscopy reveals three absorption peaks centred at 255, 261 and 269 nm (Figure 2.10). In_2S_3 NR do not present photoluminescent properties.

As the band gap of $\gamma\text{-In}_2\text{S}_3$ is of 2.53 eV [122], we would have expected an absorption corresponding to the band gap near 490 nm. Nevertheless, the energy associated to the transition we observed at 261 nm is of 4.75 eV: such a difference from bulk value can be explained from the strong quantum confinement that occurs along the thickness of the NR. Indeed, this thickness (0.7 nm) is much smaller than the excitonic Bohr radius for bulk In_2S_3 material, estimated at 33.8 nm [132].

To summarize, we successfully characterize indium sulfide NR from the combination of several techniques, from HAADF-STEM to XPS by way of XRD. The crystallographic structure of these very long and ultrathin NR turns out to be the $P\bar{3}m1$ trigonal structure, known also as the $\gamma\text{-In}_2\text{S}_3$ phase.

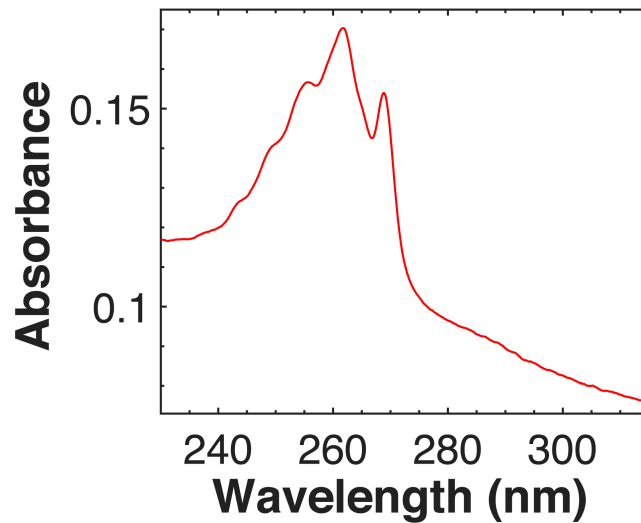


Figure 2.10 – UV-visible absorption spectrum of In_2S_3 long NR in cyclohexane.

2.4 Shape control and synthesis optimization

2.4.1 Morphological control: from hexagons to nanoribbons

Once the material characterized, we focus on the experimental conditions of the synthesis and firstly on the hydration of the indium precursor.

We found that the hydration of indium (III) chloride determines the shape of the final nano-objects. When indium chloride is a minima octahydrated, long ultrathin In_2S_3 nanoribbons as described before are obtained. When indium chloride is anhydrous, hexagonal nanoplates (NPL) are obtained (Figures 2.11 and 2.12). These hexagonal NPL are mainly regular, with an average apothem of (26.9 ± 0.5) nm (measured on 200 NPL), although some are elongated along one direction (Figure 2.12.b.).

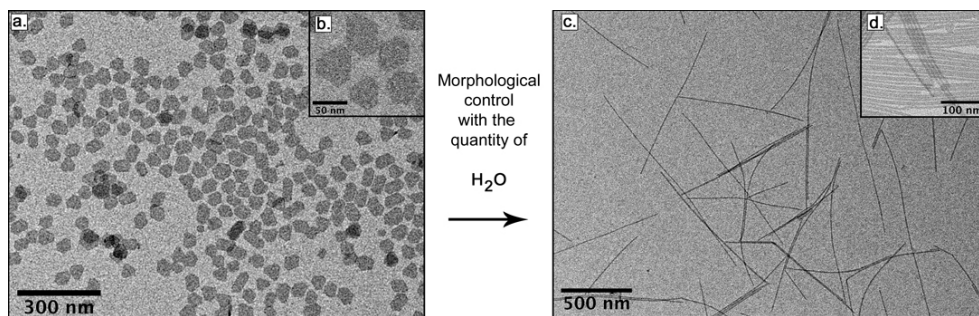


Figure 2.11 – Shape-control induced by the variation of the quantity of water in the reaction medium: TEM images of In_2S_3 hexagonal nanoplates (a., b.), and of In_2S_3 nanoribbons (c., d.).

Hexagonal NPL have the same composition as nanoribbons, as RBS measurements give a composition of the hexagons of $(57 \pm 1)\%$ of sulfur and $(43 \pm 1)\%$ of indium. The small excess of indium might reveal the presence of unreacted indium

chloride from the reaction along In_2S_3 NPL. Additionally, their XRD pattern is similar to the one of NR, indicated hexagonal NPL are also made of $\gamma\text{-In}_2\text{S}_3$ (Figure 2.14).

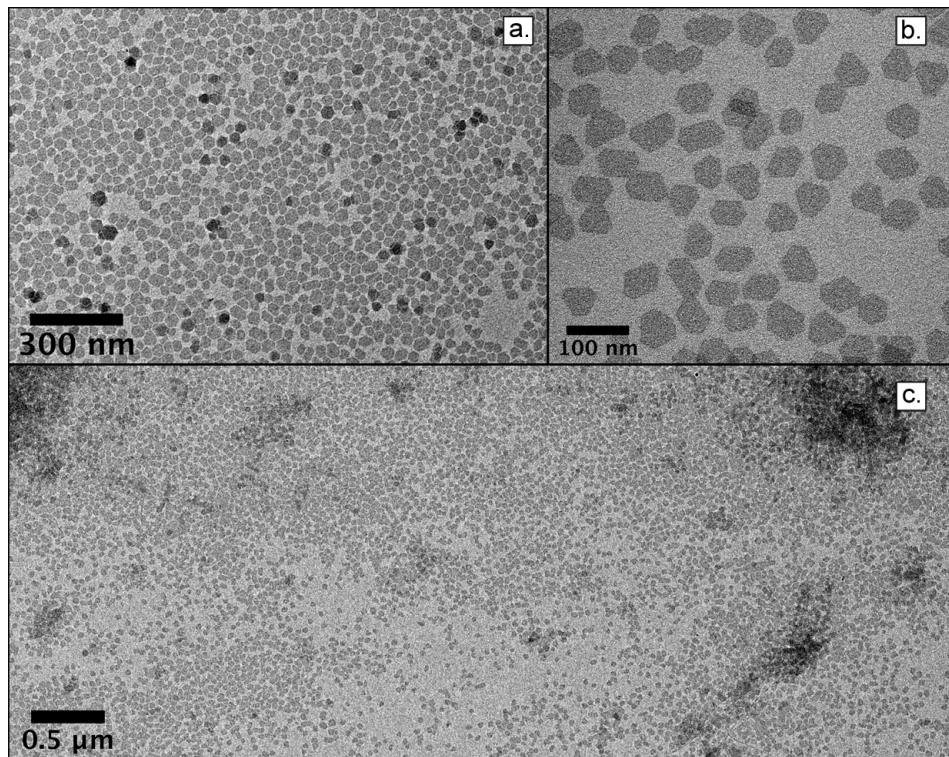


Figure 2.12 – TEM images of In_2S_3 hexagonal NPL, obtained when no water is present in the initial reaction mixture.

To further understand the evolution of shape from hexagons to nanoribbons, we realized several syntheses varying the amount of water in the initial mixture. For one equivalent of anhydrous indium (III) chloride, we add successively 0, 2, 4, 6, 8 and 10 equivalents of water. TEM image of the products of each synthesis are available on Figure 2.13 and show various nano-objects shapes depending on the quantity of water added.

Anhydrous conditions yield only hexagons. These hexagons have an average apothem of (26.9 ± 0.5) nm. The hexagons get smaller (up to twice smaller) while increasing the amount of water in the initial mixture, before completely disappearing from the crude as soon as 4 and more equivalents of water are added.

Nanotriangles appear alongside hexagons for 2 to 6 equivalents of water. The size of these equilateral triangles also decreases with the quantity of water, from an average altitude of (95 ± 3) nm to (16.8 ± 0.8) nm.

As soon as 2 equivalents of water and more are present in the initial mixture, long nanoribbons appear and form bundles. According to TEM images, the number of NR clearly increases with the amount of water in the medium. This is in agreement with the physical aspect of the crude, gradually more and more viscous when more water is added. The NR length seems maximal for 4 equivalents of water added (measurements reported on Figure 2.13). It decreases for 6 equivalents, but then increases again from 6 to 10 equivalents of water. This discrepancy could result from the purification step used to isolate In_2S_3 from the crude. This process can require trituration to redisperse nano-objects in an appropriate solvent before dropcasting on

TEM grids. This trituration, more and more important as the amount of water in the synthesis increases, may have broken some NR in length.

As soon as 8 equivalents of water and more are in the reaction medium, only long ultrathin In_2S_3 NR are obtained. Finally, we can note the presence of rectangular nanoplates which extremities are triangular only on the crude of the reaction with 2 equivalents of water. Their dimensions are $(112 \pm 11) \times (29 \pm 2)$ nm.

Figure 2.13 sums up these observations.

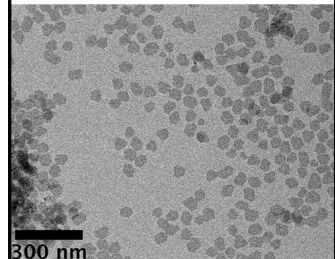
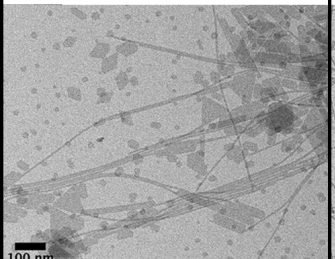
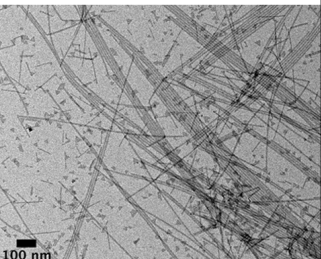
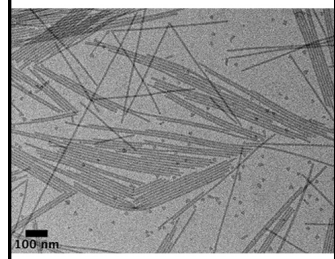
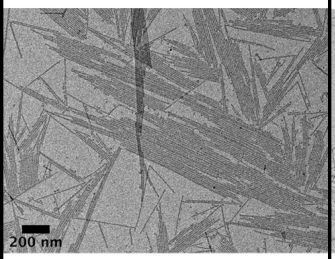

<p>a. $\text{InCl}_3, 0\text{H}_2\text{O}$</p>  <p>Hexagons : (26.9 ± 0.5) nm</p>	<p>b. $\text{InCl}_3, 2\text{H}_2\text{O}$</p>  <p>Hexagons : (14 ± 1) nm Triangles : (95 ± 3) nm Rectangular nanoplates : $(112 \pm 11) \times (29 \pm 2)$ nm Nanoribbons : $(769 \pm 30) \times (5.7 \pm 0.2)$ nm</p>	<p>c. $\text{InCl}_3, 4\text{H}_2\text{O}$</p>  <p>Triangles: (22.4 ± 0.9) nm Short nanoribbons : $(145 \pm 10) \times (5.6 \pm 0.3)$ nm Nanoribbons : $(1204 \pm 110) \times (7.3 \pm 0.2)$ nm</p>
<p>d. $\text{InCl}_3, 6\text{H}_2\text{O}$</p>  <p>Triangles : (16.8 ± 0.8) nm Nanoribbons : $(782 \pm 56) \times (7.4 \pm 0.2)$ nm</p>	<p>e. $\text{InCl}_3, 8\text{H}_2\text{O}$</p>  <p>Nanoribbons : $(817 \pm 50) \times (7.5 \pm 0.3)$ nm</p>	<p>f. $\text{InCl}_3, 10\text{H}_2\text{O}$</p>  <p>Nanoribbons : $(868 \pm 86) \times (8.0 \pm 0.3)$ nm</p>

Figure 2.13 – TEM image of products of syntheses where only the amount of water is varied with respect to the amount of indium (III) chloride. Characteristic dimensions of the various nano-objects obtained in each synthesis are given: below each image is given the measurement of the average apothem for regular hexagons, the average altitude for equilateral triangles or the average dimension of rectangular nanoplates and nanoribbons.

X-Ray diffraction was performed on the different products of reactions and shows only a decrease in intensity of the peak at 48° with the amount of water added (Figure 2.14) along the apparition of two other peaks at 47° and 49° . We conclude that all the different nano-objects reported above are of a same material, that is to say $P\bar{3}m1$ trigonal $\gamma\text{-In}_2\text{S}_3$.

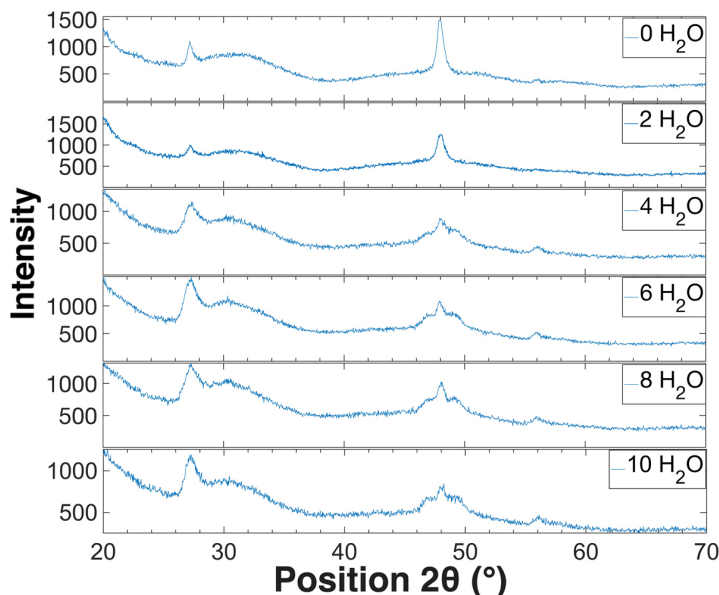


Figure 2.14 – XR diffractograms of products from syntheses of In_2S_3 nanomaterials, where only the amount of water compared to the one of indium(III) chloride is varied.

2.4.2 Synthesis optimization of NR

We then moved on the optimization of the synthesis of In_2S_3 NR in terms of temperature, indium precursors, solvent and stoichiometry (see experimental section). These experiments were performed in glass capillaries with the use of a Linkam temperature controller. This setup allows a precise control of experimental temperature parameters such as the ramp in temperature (thanks to a nitrogen pump), the final temperature and a minimal overshooting guaranteed. Moreover, thanks to its optical window, it is adaptable for optical measurements (UV-visible absorption) and SAXS/WAXS measurements. A picture of the setup is available on Figure 2.15.

The experimental procedure is described in details in section 2.8 and is based on the synthesis of In_2S_3 NR which parameters (i.e. reaction temperature, water quantity, solvent, stoichiometry) are varied. In each case, $15\mu\text{L}$ of the reaction mixture is poured in a glass capillary of 1 mm of diameter. This capillary is sealed by using a welding torch. The use of capillaries and of a Linkam heating stage allows us to realize time-resolved in-situ SAXS/WAXS measurements. At the end of each reaction, we break the capillary in order to purify the reaction medium: the reaction mixture is dispersed in a mixture of toluene and ethanol before being centrifuged. The precipitate is redispersed in THF and dropcasted onto a carbon-coated copper grid for TEM observations. As SAXS data analysis is still in progress, we will focus only on TEM analyses in this part.

Firstly, we checked this setup does not influence the outcomes of the reaction. In that purpose, we performed in a glass capillary the exact same protocol than the one

we achieved usually in autoclave. We obtained also NR that have an average length of $(1.1 \pm 0.2) \mu\text{m}$ and an average width of $(6.3 \pm 0.3) \text{ nm}$. These dimensions are in the same order of magnitude than the ones of solvothermally-synthesized NR. The main difference between these two ways of synthesis remains on their reaction volume ($15 \mu\text{L}$ vs 11.8 mL). Besides, the use of capillaries allows each sample to react in very similar conditions: the heating is guaranteed as homogeneous and identical from one capillary to another, the reaction volume in each capillary is exactly the same, and their sealing prevents the reaction mixture to be in contact with air. A better control and tuning on each reaction parameter can then be achieved. As a result, the comparison between the different outcomes of the reaction is more rigorous.

TEM analyses are performed on final products.

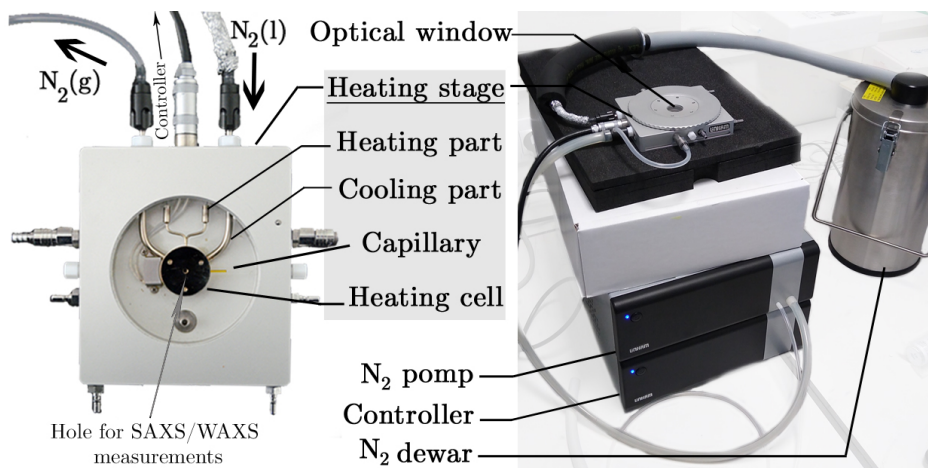


Figure 2.15 – Experimental setup for the synthesis optimization of NR using a Linkam stage. Left: heating stage - Right: general setup.

Temperature dependence:

All synthesis parameters (reaction time and volume, stoichiometry of precursors, quantity of water, ramp of temperature) are kept constant, we only vary the reaction temperature. At 180°C , no objects are synthesized. As we increase the reaction temperature, NR get more numerous, longer and wider until reaching up to 4 micrometers in length in the case of the synthesis made at 250°C . TEM images are available in Figure 2.17: the averaged dimensions of NR are made with 100 measurements and summed up in the following table 2.1.

Table 2.1 – Average measured dimensions of In_2S_3 as a function of the reaction temperature.

Reaction Temperature	180°C	200°C	230°C	250°C
Averaged length	No NR	$(97 \pm 6) \text{ nm}$	$(238 \pm 20) \text{ nm}$	$(1.6 \pm 0.1) \mu\text{m}$
Averaged width	No NR	$(5.2 \pm 0.2) \text{ nm}$	$(6.0 \pm 0.3) \text{ nm}$	$(9.4 \pm 0.3) \text{ nm}$

Uncertainties are determined as explained in section 2.2. These are important as the polydispersity in size of each sample is huge.

As we could have foreseen, increasing the temperature speeds up the reaction kinetics and favours longer and wider ultrathin NR.

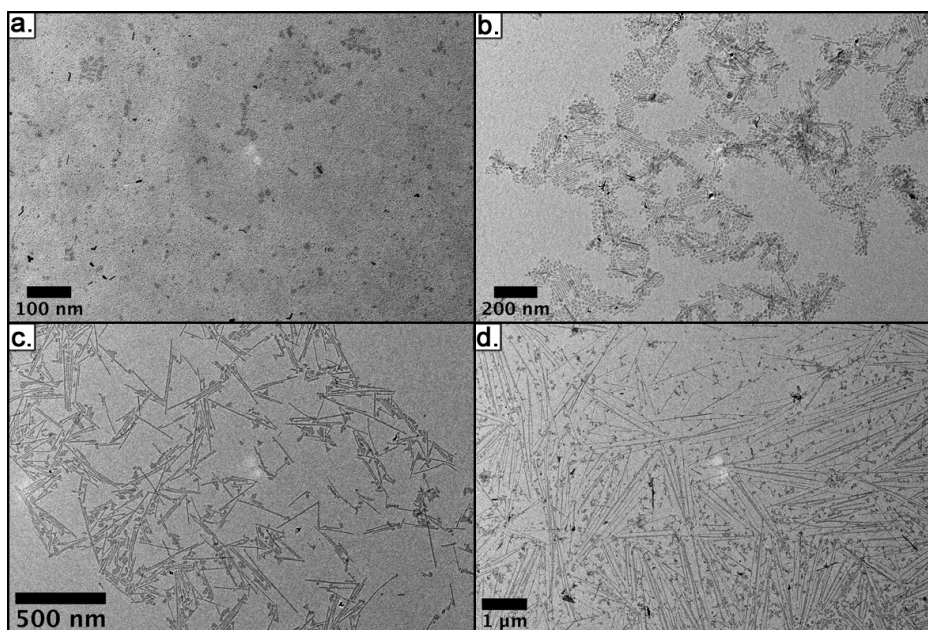


Figure 2.16 – TEMPERATURE-DEPENDENCE. TEM images of the products of In_2S_3 NR reaction at different temperatures: (a.) 180°C , (b.) 200°C , (c.) 230°C , (d.) 250°C . The quantity and length of NR increase with the reaction temperature.

Reaction time:

The same trend is observed for the increase of the reaction time at a given temperature (230°C): the longer the reaction time, the longer the NR. Indeed, after 15 minutes of reaction, NR are of (238 ± 20) nm in length for (6.0 ± 0.3) nm in width. After 2 hours of reactions, NR are (1.1 ± 0.2) μm long and (6.3 ± 0.3) nm wide. Increasing by a factor of 8 the reaction time leads to five times longer NR which present although the same width. This highlights the highly anisotropic growth character of the NR along one direction.

Change of the solvent:

We first change the solvent of the reaction which is also the surface ligand of NR, at a given reaction time (15 minutes) and temperature (230°C). Oleylamine was replaced by dodecylamine or tetradecylamine. Changing interligands interactions and ligand-surface interactions might have resulted in different conformations of NR in solution (bending, curling, bundling), as well as having an impact on their growth and their final shape (see chapter 3 and section 1.3 for ligand-surface interactions and implications). In both cases, NR with similar morphologies are obtained but with a high degree of agglomeration and difficulties to realize purifications. Indeed, dodecylamine and tetradecylamine are solids under room temperature - their melting points are respectively of 27°C and 38°C - which complicate the crude purification.

Change of the In/S ratio:

The ratio between indium and sulfur is varied in order to see the impact of an excess of one of the reagent on the outcome of the reaction or its kinetics. Results are compared to the usual condition where the ratio In:S is equal to 1 : 1.5. We keep for each synthesis a same reaction time (15 minutes) and the same reaction temperature (230°C).

With an excess of indium (In:S=1:0.5, Figure 2.17.a) or in stoichiometric proportions (In:S=1:1, Figure 2.17.b), only hexagonal nanoplates are obtained. Interestingly, when an excess of sulfur is added (In:S=1:3, Figure 2.17.d), the anisotropic growth along the direction of the NR length is enhanced. NR made with a ratio In:S=1:3 are 2.5 times longer than NR synthesized with the ratio In:S=1:1.5 (Figure 2.17.c). The former are indeed (621 ± 62) nm long for (5.6 ± 0.3) nm wide, whereas the latter are (238 ± 20) nm long for (6.0 ± 0.3) nm wide. The same width is observed between the two samples. The excess of sulfur might facilitate the nucleation of small seeds that could become more numerous: the subsequent anisotropic growth of the NR might be accelerate, leading to longer NR.

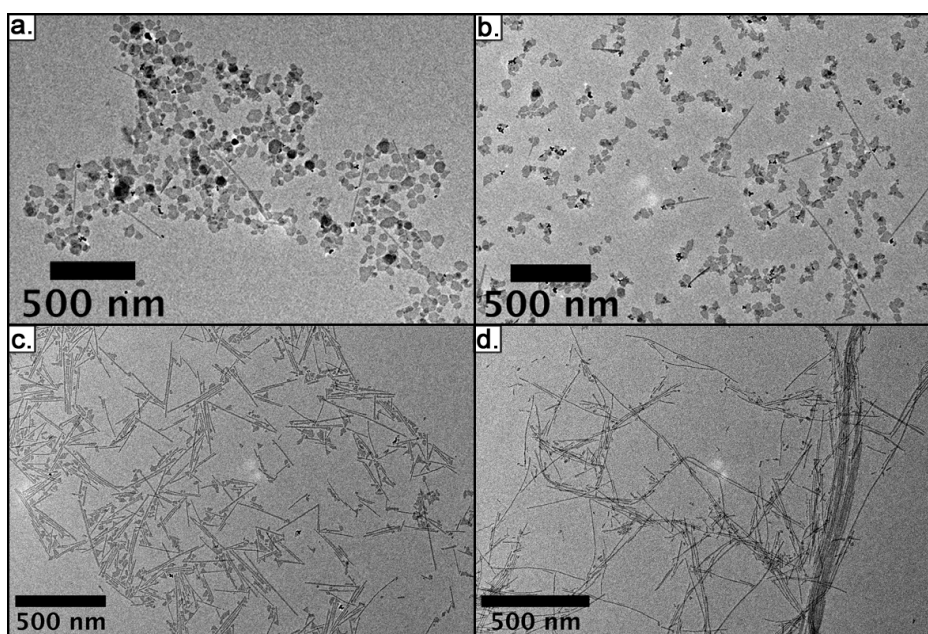


Figure 2.17 – CHANGE IN IN:S RATIO. TEM images of the products of NR reaction at different stoichiometric ratios between indium and sulfur : (a.) In:S=1:0.5, (b.) In:S=1:1, (c.) In:S=1:1.5 (usual condition), (d.) In:S=1:3. The quantity and length of NR increase with the ratio In:S.

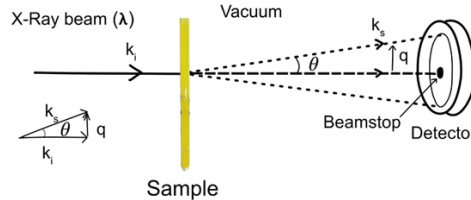
2.5 Insights into formation mechanism of In_2S_3 NR

In order to better understand the role of water in NR synthesis, we performed time resolved in-situ SAXS/WAXS. We expected to shed light on the nucleation and growth of In_2S_3 NR, in the same way it was done for instance on CdSe QD [133] or NPL [66].

About Small-Angle X-Ray Scattering

X-Ray diffraction at small angles (typically $0,1^\circ$ to 10°) allows the determination of statistically relevant structural information on the sample in the 1 - 1000 nm range. This technique is not destructive, presents no preparation artefact and can be applied for liquids as well as for solids [134]. A lot of information can be extracted from SAXS experiments. For instance, the size and concentration of CdS, CdSe, PbS or PbSe QD was determined by SAXS [134], as well as the growth kinetics and mechanism of CdSe QD [133]. Shape and structural information may also be encoded in SAXS pattern: for example, the radius of curvature of bended CdSe NPL was calculated from SAXS [66]. The investigation of the structure and interactions within a system, such as a protein, is also an important field of investigation that can be probed by SAXS [135].

The technique lies upon the scattering of a monochromatic X-ray beam of incident wave vector \vec{k}_i by the sample. This elastic interaction gives rise to a scattered wave of wave vector \vec{k}_s , which modulus is equal to the one of \vec{k}_i . The scattered beam is detected on a 2D position sensitive detector. For isotropic samples, the SAXS intensity does not depend on the azimuthal angle of the detector, such as it is possible to average the data over this angle without losing any information [134, 136]. The scattered intensity is then plotted as a function of the modulus of the scattering vector $\vec{q} = \vec{k}_i - \vec{k}_s$, defined by $q = \frac{4\pi \cdot \sin(\theta)}{\lambda}$ with θ the scattering angle and λ the wavelength of the incident beam [137, 136].



SAXS intensity can be expressed as a function of the form factor of the particles constituting the sample, which depends on their size and shape: information on the particle morphology may be gleaned by considering its limiting form [136]. For instance, for small q value (Guinier regime) and a dilute system, it is a function of q^2 . Thereby, plotting the SAXS intensity (which is proportional to the form factor) as a function of q^2 gives access to the radius of gyration of a particle (e.g. the radius for spherical particles).

At large q (Porod regime), the asymptotic behaviour of the SAXS intensity follows a power law with an exponent that depends on the dimensionality of the particle: the SAXS intensity of rods is proportional to q^{-1} , whereas the SAXS intensity of flat NPL is proportional to q^{-2} . For spheres, the SAXS intensity is proportional to q^{-4} and moreover to its surface area [136, 134]. Finally, SAXS pattern interpretation can provide information on the statistical distribution of particle sizes, as well as on inter-particle interactions [136].

Different reaction batches differing just in their composition in water were placed inside glass capillaries (see experimentals and Figure 2.15 for details on the procedure and the setup). Capillaries were sealed and heated 15 minutes at 230°C thanks to a Linkam temperature controller while SAXS acquisition was performed throughout the whole synthesis. Time-resolved in-situ synchrotron SAXS/WAXS was realized at SOLEIL in Saclay or at the ESRF in Grenoble.

Data are currently still under treatments and analyses with the help of Laurent Lermusiaux from the chemistry laboratory of the ENS de Lyon. Nevertheless, first insights can already be brought out.

Firstly we can draw a growth scenario about the synthesis without any water. We showed that in such case hexagonal nanoplatelets (NPL) are obtained. SAXS intensity is plotted in function of q and its evolution is followed along time (Figure 2.18.a.). In each case, the peak at $q \sim 10.5 \text{ nm}^{-1}$ is attribute to the solvent.

During the first 5 minutes of reaction (Figures 2.18.a.1 and 2.18.a.2), the intensity at small q is increasing with a plateau. The temperature reaches 150°C , according to the temperature ramp of $30^\circ\text{C}.\text{min}^{-1}$. We interpret this stage as the nucleation of small spheres which grow in number, as a clear Guinier regime increases (i.e. at small q , the SAXS intensity is function of q^2) and as no shape changes of the objects seem to happen.

From 5 minutes to 7.5 minutes of reaction, the intensity at small values of q increases while the one at large values of q is constant (Figure 2.18.a.3). This supports the hypothesis (also founded in the literature for similar SAXS intensity evolution [133]) that attractive interactions occur between these spheres, leading to the formation of bigger nanoparticles.

After 8.5 minutes, as the temperature has reached its final value of 230°C , a Bragg peak appears at the position of $q^*=1.462 \text{ nm}^{-1}$ (Figure 2.18.a.4.). Until the end of the reaction this peak and its two harmonics (at $2q^*=2.85 \text{ nm}^{-1}$ and $3q^*=4.28 \text{ nm}^{-1}$) grow in intensity (Figure 2.18.a.5.). In the same time, an oscillation at low q appears and can correspond to the lateral dimension of 2D NPL (Figure 2.18.a.5.).

The characteristic distance associated to the Bragg peak at $q^*=1.462 \text{ nm}^{-1}$ is of $d^* = \frac{2\pi}{q^*} = 4.406 \text{ nm}$. It can correspond to the distance between two oleylamine-capped nano-objects, separated each other from a distance of d^* which correspond to the distance of two oleylamine molecules. Indeed, the length of one oleylamine molecule is $d_{\text{oleylamine}} = 1.95 \text{ nm}$ according to our molecular modelling^f. The ligand and brushes of these objects might not interpenetrate (as d^* is slightly superior to $2 \times d_{\text{oleylamine}}$) but are sufficiently close to interact and to lead to the stacking of the nano-objects. These nuclei might then order and fuse in such a lamellar phase, that serve as a template and ends up with the formation of NPL. These different steps in the growth of NPL are summed up in Figure 2.19.

f. i.e. Avogadro modelling of one oleylamine molecule. We report its final length after a conformation energy optimization of the molecule.

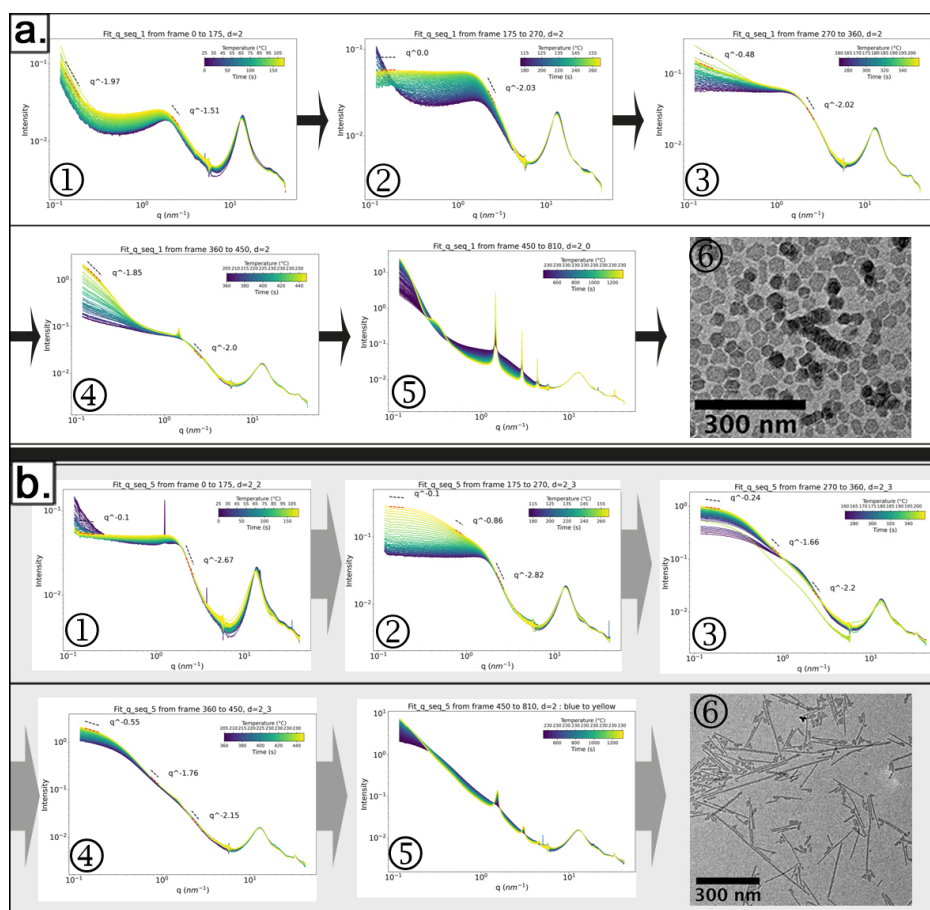


Figure 2.18 – Time-resolved in situ SAXS/WAXS measurements for the synthesis of hexagonal NPL (top, path (a.) no water added in the reaction mixture) along the data for the synthesis of nanoribbons (bottom, path (b.) in grey, water added in the reaction mixture). In each case, the scattered intensity is plotted in function of the scattering vector for different reaction times, as the reaction temperature is increased. These plots were realized by Laurent Lermusiaux. At the end of each paths (a.) or (b.) is a TEM image of the resulting as-synthesized nano-objects (i.e. respectively flat hexagons, which can stack one upon each other, or nanoribbons).

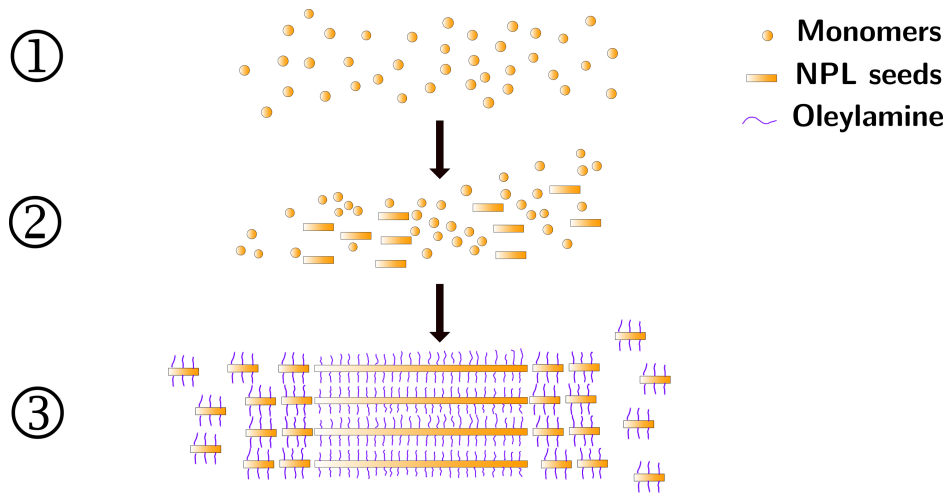


Figure 2.19 – Mechanism suggested for hexagonal NPL growth after preliminary interpretations of time-resolved in-situ SAXS. 1. First occur the nucleation of small spheres. 2. These spheres interact to form nuclei that stack one upon each other. 3. This lamellar phase could serve as a template to the formation of NPL. Oleylamine molecules are not represented in steps 1 and 2 for clarity reasons.

We then turn on the effect of water on this synthesis, by acquiring SAXS on samples with varying amounts of water. Again, data are still under treatments and analyses. Let us consider the synthesis with 8 equivalents of water compared to one of indium chloride (i.e. the normal conditions that leads to NR). Figure 2.19 allows the comparison between SAXS patterns of the synthesis without water (Figure 2.19.a.) and the one with 8 equivalents of water (Figure 2.19.b.). The first step is similar in both cases: we see an increase in intensity with a flat plateau at low q which we attribute to the nucleation of small spheres. Nevertheless, in the case where water is added, the intensity in the medium q range increases before the onset of the final peaks (i.e. from frames 175 to 810 of path b., Figures 2.19.b.2 to 2.19.b.5). This can be the signature of an anisotropic growth of the particles before the formation of the lamellar phase evoked above.

The intensity slope is close to q^{-1} which is typical of rod like objects. Therefore, we hypothesize the following growth mechanism for In_2S_3 NR : fist occurs the nucleation of small spheres. Such nuclei starts to aggregate in a 1D growth process. This anisotropic growth could be induced by chelation of water molecules on preferential crystallographic facets of seeds and is favoured with the increase of the amount of water molecules in the reaction mixture. Then, in a third and last step, these threads might fused into 2D ribbons, probably inside a lamellar templating framework.

Of course this is just preliminary hypotheses which still need to be confirmed and supported by precise and further analyses of our data.

2.6 Colloidal stability and bundling in solution

Finally, we wondered about finding an appropriate solvent to ensure the colloidal stability of the NR. Indeed, NR are dispersed in toluene after synthesis, which leads to a cloudy and viscous yellow colloidal solution that precipitates in few hours. Moreover, we remarked NR tend to form bundles when dispersed in toluene as seen on TEM images in Figure 2.21.a.

We dispersed the same amount of NR in a same volume of different solvents (see experimental section). Apolar solvents (Figure 2.21) as well as polar aprotic solvents (Figure 2.22) were tested. Protic polar solvents such as ethanol lead to an immediate precipitation of the NR, as well as acetone or ethyl acetate which are all known as typical nonsolvents used in nanocrystals purification.

In terms of the visual aspect of the colloidal solutions, they are all yellow and cloudy and precipitate rapidly except for four solvents: cyclohexane, chloroform, hexane and tetrahydrofuran (Figure 2.20.a.). The dispersion in cyclohexane stays yellow-transparent in time but jellifies and does not suspend all NR. The dispersion in chloroform is initially yellow-transparent but becomes cloudy after one day. The hexane solution stays partially cloudy compared to others. Finally, the solution in tetrahydrofuran (THF) is perfectly yellow transparent and is very stable over time (Figures 2.20, 2.21 and 2.22). The stability of the solution is ensured even at a high concentration of NR compared to the case with toluene (Figure 2.20.b. and 2.20.c.).

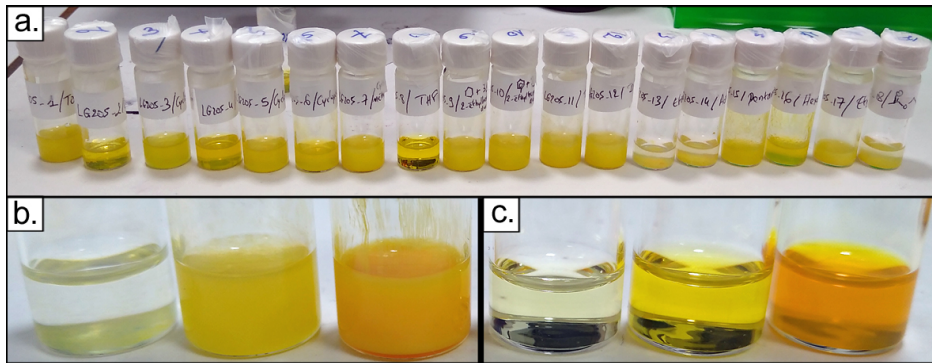





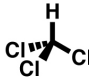


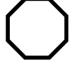
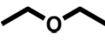

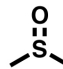
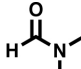
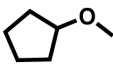

Figure 2.20 – COLLOIDAL STABILITY OF NR (a.) From left to right, pictures of In_2S_3 NR solutions in: toluene, cyclohexane, cyclohexene, chloroform, cyclooctane, cyclopentane, cyclopentylmethyl ether, THF, cyclohexane with 2-ethylhexylamine (to try to stabilize the solution), toluene with 2-ethylhexylamine, DMSO, DMF, ethanol, acetone, pentane, hexane, diethyl ether, ethyl acetate - (b.) In_2S_3 NR solution in toluene when NR concentration is varied, with dilution factors of 0.1, 1 and 10 from left to right - (c.) In_2S_3 NR solution in THF when NR concentration is varied, with dilution factors of 0.1, 1 and 10 from left to right.

We then analysed these samples by TEM (Figures 2.21 and 2.22). NR tends to form bundles in most of cases except for three solvents: chloroform (Figure 2.21.d.), cyclohexene (Figure 2.21.i.) and tetrahydrofuran (THF, Figure 2.22.e). In these dispersion, NR do not aggregate and lie separately on TEM grids.

We describe these bundle in terms of length, width and general aspect in Table 2.2. Bundles are more or less dense and long according to the solvent: solvent with a high polarity (e.g. DMSO, DMF) especially form long and thick bundles of NR. Nevertheless, important bundling is also observed in apolar solvents such as toluene. Hence, polarity does not seem to be the only pertinent parameter to control the bundling of the NR.

If the ionizing power of the solvent seems not appropriate, its dissociative power

Table 2.2 – TEM measurements on bundles of NR in various solvents.

SOLVENT	Toluene 	Cyclohexane 	Hexane 	Chloroform 	Cyclopentane 	Pentane 	Cyclooctane 
μ (D)	0.375	0	0.08	1.15	0	0	?
ϵ	2.4	2.02	1.9	4.8	2	1.84	?
LENGTH (SD) - μm	12.957 (5.246)	6.798 (2.103)	4.478 (1.572)	2.405 (1.217)	8.998 (3.107)	4.261 (1.853)	15.044 (7.411)
WIDTH (SD) - μm	0.819 (0.261)	0.320 (0.068)	0.238 (0.133)	0.225 (0.080)	0.418 (0.125)	0.199 (0.091)	0.526 (0.198)
Bundling	++	+	+	--	++	++	++
Bundle aspect	Large, bended	Thin, straight	Lots of thin bundles made of few NR	Straight, in very few number	Long, bended, tangled	As in hexane, but with more NR per bundle	Long, thin, straight
SOLVENT	Diethyl ether 	Cyclohexene 	DMSO 	DMF 	Cyclopentyl methyl ether 	THF 	
μ (D)	1.098	0.332	4.06	3.86	?	1.75	
ϵ	4.3	18.3	47	36.7	?	7.6	
LENGTH (SD) - μm	20.455 (5.872)	No bundle	5.619 (2.025)	3.998 (1.461)	1.908 (0.826)	No bundle	
WIDTH (SD) - μm	0.524 (0.165)		0.188 (0.087)	0.137 (0.073)	0.295 (0.117)		
Bundling	+++	---	+++	+++	+	---	
Bundle aspect	Straight, braided, lots of NR per bundle		Numerous, aggregated, lots of NR per bundle	Few bundles, straight, braided	Lots of small bundles		

μ is the dipolar moment of the solvent, ϵ its dielectric constant (when known) at 298 K.

The average length and width of the bundles according to the solvent are given in μm along the standard deviation (SD) associated to the statistical series (of at least 50 measurements each).

The quantity of bundles in solution is evaluated on a qualitative scale (--- : no bundling in solution / +++ : very important bundling in solution).

Finally, the aspect of a bundle in each solvent is given.

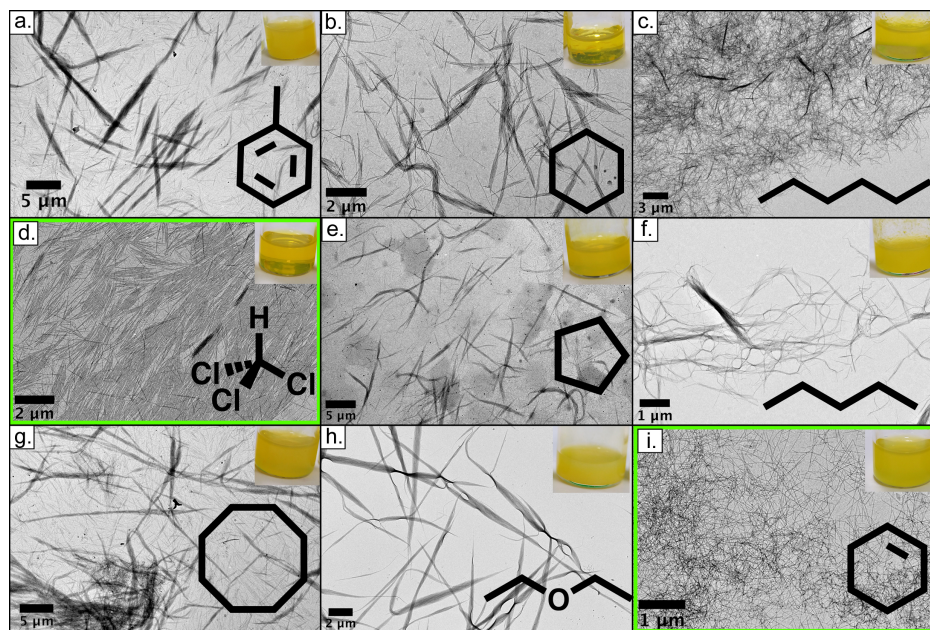


Figure 2.21 – COLLOIDAL SOLUTION OF NR IN APOLAR OR WEAKLY POLAR SOLVENTS. TEM images of the redispersion of a same amount of In_2S_3 NR in a same volume of the following solvents: (a.) toluene, (b.) cyclohexane, (c.) hexane, (d.) chloroform, (e.) cyclopentane), (f.) pentane, (g.) cyclooctane, (h.) diethyl ether, (i.) cyclohexene. Inserts are pictures of the colloidal dispersions. Green boxes indicate solvents that allow a good dispersion of NR, as seen on TEM grids.

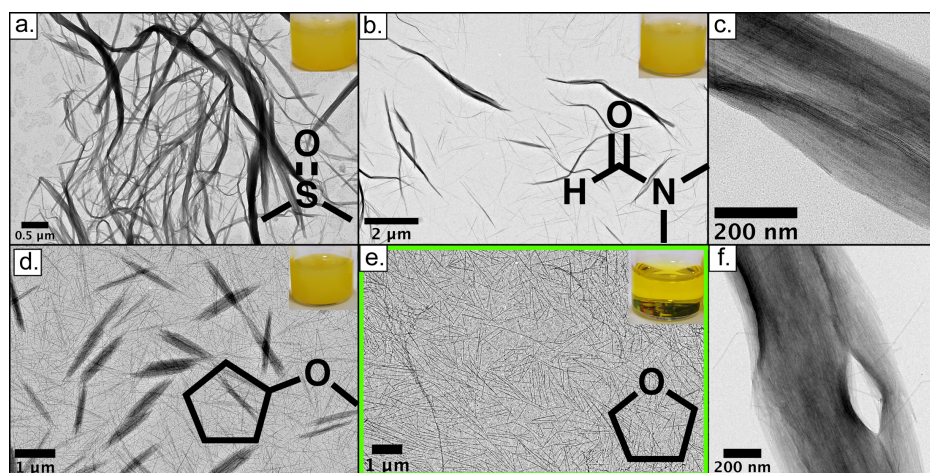


Figure 2.22 – COLLOIDAL SOLUTION OF NR IN POLAR SOLVENTS. TEM images of the redispersion of a same amount of In_2S_3 NR in a same volume of the following solvents: (a.) dimethyl sulfoxide (DMSO), (b.) dimethylformamide (DMF), (d.) cyclopentylmethyl ether, (e.) tetrahydrofuran (THF). Inserts are pictures of the colloidal dispersions. Green boxes indicate solvent that allows a good dispersion of NR, as seen on TEM grids. (c.) and (f.) are magnification on a bundle in respectively DMF and diethyl ether. NR are stack together side by side in the direction of their length, forming bundles that can reach several micrometers in length and several hundreds of nanometers in width, according to the solvent of dispersion used.

might play a role in the bundling. We note that the solvents which prevent bundling get moderate values of dielectric constant. It appears then the use of solvents with intermediate values of dipolar moment ($1 < \mu < 2$ D) and dielectric constant ($5 < \epsilon < 20$) prevent the formation of bundles. Further investigations are now necessary to establish a proof and explanation of such a direct correlation between the formation of bundles and the properties of the solvent.

First insights were given from SAXS/WAXS analyses on these samples. Data are currently under treatment and analyses with the help of Laurent Lermusiaux from the chemistry laboratory of the ENS. Figure 2.23.a. reports the SAXS/WAXS patterns of NR dispersions in solvents where no bundles were observed in TEM (i.e. "non-bundling solvents" as cyclohexene and THF), whereas Figure 2.23.b. reports the SAXS/WAXS patterns of some NR dispersions in solvents where strong bundling was observed in TEM (i.e. "bundling solvents" such as toluene, DMSO, DMF or Et₂O).

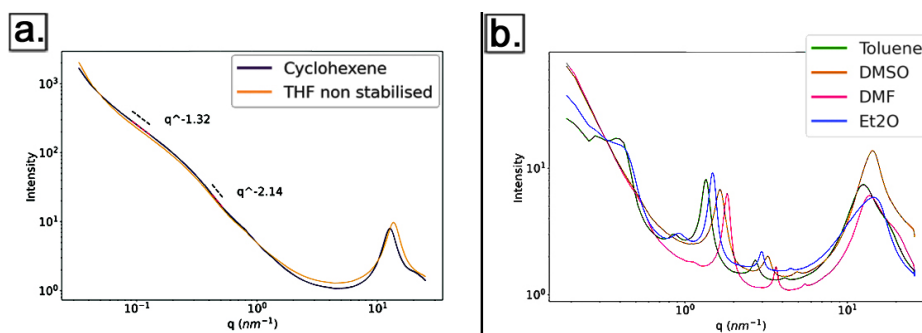


Figure 2.23 – SAXS/WAXS patterns of a NR dispersion respectively in (a.) non-bundling solvents (THF, cyclohexene) and (b.) bundling solvents (toluene, DMSO, Et₂O, DMF). These plots were realized by Laurent Lermusiaux.

For "non-bundling solvents" dispersions (i.e. NR in THF, cyclohexene, Figure 2.23.a.), no Bragg peaks are observed, proving there is no agglomeration of NR and thus no bundling in these solvents. This is consistent with TEM observations. At small q , the SAXS intensity evolves as q^{-1} : we saw few paragraph above this behaviour is typical of rod-like objects. For larger q , it evolves as q^{-2} , which is typical of NPL. It is important to keep in mind that the apparent dimensionality inferred from experiment may change with the range of wavevector considered: how an object appears depends on the length scale at which it is investigated [136]. That is why at small q , NR can be seen as long nanowires, hence the q^{-1} SAXS intensity dependence (this is understandable as the length of the NR is two orders of magnitude longer than its width). At larger q , NR can be seen much more as NPL, hence the q^{-2} SAXS intensity dependence.

For "bundling solvents" dispersions (e.g. NR in toluene, DMSO, DMF, Et₂O, Figure 2.23.b.), Bragg peaks are observed in the range of 1 to 2 nm⁻¹. This confirms the bundling of NR in solution and is consistent with TEM analyses. The fact the position of the Bragg peak varies with the solvent means the distance between NR inside a bundle varies with this solvent. Typical distances from 6.3 nm ($q \sim 1$ nm⁻¹, in toluene) to 3.1 nm ($q \sim 2$ nm⁻¹ in DMF) are observed. This is another proof than the nature of the solvent influences greatly the bundling of NR.

Solvent molecules might intercalate and order within the ligand shell of the NR, as it was advanced for gold nanowires in hexane [138]. This intercalation would result in a loss in entropy of the system. In the case of dispersed NR, the formation of bundle would be favoured as it minimizes this decrease in entropy. Indeed, when NR bundles, they share ordered solvent molecules. Compared to the case where NR are isolated, the area where solvent molecules have to be ordered is then divided by two (i.e. solvent molecules only needs to be ordered once in a bundle of 2 NR). The decrease in entropy of the system is thus limited. This hypothesis has to be checked by the detailed and upcoming analyses of our datas, without excluding other potential mechanisms that may come out. For instance, in the case of polar solvents, the non-miscibility of the ligands may also favours direct interaction and interpenetration between ligand shells. The bundling could then originate merely in this case from a phase separation.

Looking for stable colloidal suspensions is relevant in the perspective of further potential applications of In_2S_3 long NR: one can imagine succeeding in their alignment in solution and thus the emergence of new ensemble properties (for instance the creation of a liquid-crystal phase).

2.7 Outlooks

We reported in this chapter the solvothermal synthesis of trigonal In_2S_3 ultrathin and long nanoribbons. Nanoribbons dimensions were determined by TEM: NR length is of (1162 ± 44) nm for a width of (8.7 ± 0.1) nm and a thickness of (0.71 ± 0.04) nm.

Their composition was investigated by RBS and XPS, both techniques agreeing on the empirical formula of In_2S_3 . Additionally, XPS allowed us to determine the surface ligand density of these NR as 2.3 oleylamine molecules. nm^{-2} and 0.5 ethanol molecules. nm^{-2} .

XRD combined with HAADF-STEM observations led to the final attribution of the trigonal $P\bar{3}m1$ crystallographic structure.

The growth mechanism of NR was investigated by time-resolved in-situ synchrotron SAXS/WAXS: data are currently still under treatment but already let us hypothesize a 3-steps growth mechanism. First takes place the nucleation of small spheres. A one-dimension growth then occurs as water might bind into specific reactive facets. Finally a fusion of these rods happens to lead to nanoribbons. Further works and full interpretations of data are needed to be done to get more insights.

Furthermore, we highlighted the amount of water is a crucial parameter of the synthesis. Just by tuning it we are able to realize an accurate shape control of the reaction products, from hexagonal nanoplates in anhydrous conditions to micrometer-sized nanoribbons when water is added inside the reaction medium. An optimization of the synthesis was done, in terms of reaction temperature and time, stoichiometry, solvent and amount of water.

Finally, we focused on the colloidal stability of NR in suspension. By varying the nature of the solvent and looking to the sample in TEM, bundles of NR were pictured in all cases except for chloroform, cyclohexene and THF. Further works (SAXS/WAXS analyses) need still to be done in order to understand the origin of the bundling and to establish an exact link between the bundling phenomenon and chemico-physical properties of solvents.

Moreover, we saw no aggregation when THF is used as a solvent of dispersion, leading to excellent and stable dispersions. This is important in order to investigate more in details optical properties of NR and their behaviour in solution: we expect in a near future to create liquid-crystal phase by aligning these NR inside the sample along their length direction. This expectation comes from preliminary observation of birefringence from our sample when observed through a polarizer-crossed analyzer system.

2.8 Materials and experimental methods

2.8.1 Starting Materials and chemicals

Indium (III) chloride (anhydrous, 99+%), chloroform, cyclopentane, THF, diethyl ether and ethyl acetate were purchased from Fisher-Alfa Aesar. Indium (III) chloride is stored in a glovebox. Sulfur (powder, 99.998%), cyclohexene and cyclooctane were purchased from Sigma-Aldrich. Oleylamine (approximate C18-content 80-90%), cyclohexane, DMSO, DMF, acetone and hexane were purchased from Fisher-Acros Organics. Absolute ethanol and toluene ($\geq 99.5\%$) were purchased from VWR.

2.8.2 Instrumentation

TEM images were acquired on a JEOL JEM-1400 (accelerating voltage of 120kV) at CIQLE Lyon. The sample are prepared by drop casting In_2S_3 NR suspensions in toluene onto 200 carbon-coated copper grids. To avoid agglomeration of NR on the TEM grids, the suspension of NR can be beforehand diluted a minima by a factor of ten and sonicated 2 minutes in a bath. In_2S_3 ultra-thin NR are electron beam sensitive and may deteriorate in a few seconds.

HR-STEM pictures have been acquired using a Jeol Neoarm operating at 200kV at the Centre Électronique de Microscopie Stéphanois, in Saint-Étienne, with the help of Benoit Mahler from the ILM Lyon.

UV-vis absorption was measured on a Lambda 750 Perkin-Elmer and an OceanOptics spectrophotometers.

Powder X-Ray Diffraction (XRD) analyses were realized with a PANalytical Empyrean X-ray diffractometer equipped with a 1.8 kW $\text{Cu K}\alpha$ ceramic tube, operating at 45 kV and 40 mA and a PIXcel3D 2 x2 area detector.

Rutherford backscattering spectrometry (RBS) was used in order to measure the mean atomic composition $[\text{S}]/[\text{In}]$. For this purpose the sample, initially in powder form, was deposited on a carbon adhesive tape. The analysis was performed with 4He^+ ions of 2 MeV energy delivered by the 4 MV Van de Graaff accelerator of the "ANAFIRE" platform located at the Institut de Physique des 2 Infinis (IP2I) Laboratory of Lyon. The backscattered particles were detected with a 15 keV resolution implanted junction set at an angle of 169° with respect to the beam axis. The experimental data were fitted with the help of the SIMNRA simulation code [124]. RBS analyses were performed with the help of Bruno Canut from the INL.

XPS spectra were recorded on a THERMO K-alpha+ spectrometer with the $\text{Al K}\alpha$ line used as the excitation source at the Laboratoire Science et Surface of Ecully (Serma Technologies).

Part of the synchrotron SAXS experiments were performed on the SWING beamline at the SOLEIL synchrotron (Saint-Aubin, France) using an X-ray energy of 16 keV with a sample to detector distance of 1 m. The other experiments were performed on beamline ID02 [139] at the ESRF (Grenoble, France) with an energy of 12.23 keV, with a sample to detector distance of 1.2 m.

2.8.3 Solvothermal synthesis of In_2S_3 NPL

0.265 g of anhydrous indium (III) chloride (1.2 mmol, 1 eq.), 0.0576 g of sulfur powder (1.8 mmol, 1.5 eq.), 11.8 mL of oleylamine are introduced in a 20-mL Teflon-lined autoclave. The reaction mixture is ultrasonicated 10 minutes to get a homogeneous solution. The autoclave is then sealed and heated at 215°C for 2h in an oven. Once it is cooled down to room temperature, the yellow viscous resulting mixture is centrifuged 5 minutes at 6153 x g; the product is then redispersed in 5 mL of ethanol before being centrifuged 5 minutes at 6153 x g. The product is then redispersed in 5 mL of toluene and 3mL of absolute ethanol are added: the system is centrifuged again 5 minutes at 6153 x g, and this last procedure is repeated at least once with a redispersion in 5mL of toluene. The final yellow product is redispersed in 10 mL of toluene. Hexagonal nanoplatelets are obtained.

In order to synthesize ultrathin and long In_2S_3 nanoribbons, the exact same procedure as above is applied, adding in the initial mixture on top of the reagents listed above 170 μL of water (9.6 mmol, 8 eq). A typical concentration in NR obtain at the end of the purification process is of 31 g/L.

2.8.4 Growth kinetics: Time-resolved in-situ synchrotron SAXS / WAXS

Anhydrous indium (III) chloride, sulfur powder and oleylamine are mixed in the proportions described above for the synthesis of In_2S_3 nanoribbons. Different equivalents of water are added as respect to the quantity of indium chloride, that is to say 0, 2, 4, 6, 8 and 10 equivalents.

15 μL of the mixture is poured in a glass capillary of 1 mm of diameter, a length of 80 mm and a thickness of 0.01 mm. The capillary is sealed thanks to a welding torch. After sealing, the capillary measures approximately 20 mm long. Time-resolved in-situ synchrotron SAXS/WAXS is then performed while the capillary is heated from room temperature to 230°C for 15 minutes, with a temperature ramp of 30°C/min, thanks to a Linkam stage.

Other reaction parameters are then tested, such as the reaction temperature (180°C, 200°C, 250°C), the stoichiometry (ration In/S of 1/0.5, 1/1, 1/1.5, 1/3) or the reaction solvent (dodecylamine, tetradecylamine, oleylamine).

At the end of each reaction, the capillary is broken, the reaction mixture is dispersed in a mixture of 1 mL of toluene and 0.5 mL of ethanol, before being centrifuged and redispersed in THF. The resulting solution is dropcasted onto a carbon-coated copper grid for TEM observations.

2.8.5 Bundling of In_2S_3 nanoribbons

900 μL of toluene is added to 100 μL of In_2S_3 nanoribbons solution in toluene prepared above. After centrifugation, the supernatant is removed. NR are redispersed in various solvents, such as toluene, cyclohexane, hexane, cyclohexene, chloroform, cyclooctane, cyclopentane, pentane, cyclopentylmethyl ether, DMSO, DMF, ethanol, acetone, diethyl ether or ethyl acetate.

40 μL of each dispersion are injected in glass capillaries. The capillaries are then sealed in the same way as described above thanks to a welding torch. The dispersion are also analysed by TEM after dilution by 10 and dropcasting onto TEM grids.

CHAPTER 3

Conformation control of indium sulfide nanoribbons by ligand exchange

Chapter abstract

We report in this chapter the conformational control of ultrathin indium sulfide nanoribbons (NR) under surface ligand exchange.

These nanoribbons adopt a coiled conformation when solvothermally synthesized in octylamine. The combination of X-ray photoelectron spectroscopy (XPS), X-Ray diffraction, energy-dispersive X-ray spectroscopy (EDX), selected-area electron diffraction (SAED) and HAADF-STEM permit to identify the composition and the crystallographic structure of this nanomaterial that turns out to be orthorhombic InS.

When native octylamine is exchanged with longer carbon-chain primary amine ligands, the curvature of the NR decreases to reach flat ribbons for C18 carbon-chain amines. The unfolding of the NR according to the different exchanged amino-ligands is quantified by TEM curvature measurements and synchrotron SAXS.

The dimensions of the unfolded NR are determined by TEM: these are of (152 ± 4) nm in length for (9 ± 2) nm in width and (1.3 ± 0.2) nm in thickness.

Finally, we have successfully induced chiroptical properties in NR by exchanging native surface ligands with a chiral amino-acid through a phase transfer procedure.

We saw in chapter 1 (section 1.3) that there is a direct interplay between the surface stress induced by the ligands, the shape of the 2D-nanomaterial and its optical properties. The accurate tuning of its properties is thus achievable by controlling its shape. That may be performed by choosing an appropriate surface ligand, and so the nature of the stress (compressive or tensile) it imposes on its surface [71].

For this purpose, solvothermally-synthesized indium sulfide nanoribbons (NR) described in this chapter represent an ideal model system. Indeed, they exhibit a coiled conformation after synthesis and their average radius of curvature can be easily measured from TEM experiments. Uncoiling these NR by ligand exchange was then a great challenge to achieve in order to illustrate the link between ligand-induced surface stress and nanoparticle conformation.

The first part of this chapter is dedicated to their synthesis and characterization.

Compared to the NR described in the last chapter, these objects are much shorter in length even if they still present a high degree of anisotropy. In a second part, we report the conformation control of NR by ligand exchange between a coiled and an uncoiled conformation. Finally, we show in a third part preliminary results on chiroptical properties induced by ligand exchange of penicillamine using a phase transfer method.

3.1 Synthesis and characterization

Indium sulfide nanoribbons are synthesized from indium acetate and sulfur in octylamine by a solvothermal method synthesis inspired by Wang et al. [74, 75]. Indium (III) acetate and sulfur powder are dissolved in a mixture of 1-octylamine and absolute ethanol in a Teflon-lined autoclave (Figure 3.1 - see the experimental section for more details). The autoclave is sealed and heated 12h at 220°C in an oven. The yellow resulting product is then washed at least once with absolute ethanol and twice with a mixture of toluene and absolute ethanol using centrifugation. The final indium sulfide NR are finally dispersed in toluene. Transmission Electron Microscopy (TEM) and high angle annular dark field STEM (HAADF-STEM) display coiled NR (Figure 3.2). Octylamine-capped NR tend to form aggregates (Figure 3.2.b): a dilution and sonication of the solution before dropcasting on a TEM grid is then necessary to observe isolated NR.

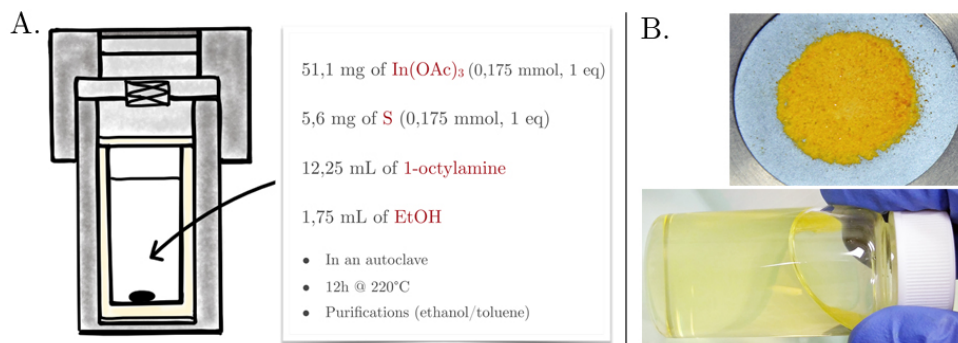


Figure 3.1 – A. Scheme of the experimental conditions - B. Top: Nanoribbons in the powder form, Bottom: Colloidal solution of nanoribbons dispersed in toluene.

By examining NR lying on their side (Figures 3.2.a. and 3.2.c.), we can discriminate two distinct ways of coiling: one where the extremities of the NR coil along a same direction (Figure 3.2.e., in/in conformation) and another where they coil in opposite directions (Figure 3.2.d., in/out conformation). From these observations, we are able to measure the length and the thickness of the nanoribbons, which are respectively of (138 ± 10) nm and (1.3 ± 0.2) nm. Besides, by examining NR lying flat (Figure 3.2.b.), we measure an average width of (10 ± 2) nm^a.

A previous report [74] on the same material attributed to these NR the chemical formula In_2S_3 despite a lack of thorough investigation. In order to determine the exact composition of the NR, we first performed Rutherford Backscattering Spectrometry (RBS) (Figure 3.4). The ratio between indium and sulfur is of (1.05 ± 0.04) , leading

a. We repeat the measurement on a statistical assembly of NR (typically a hundred of NR). The global uncertainty given for each dimension is then $U = 2 \cdot \sqrt{U_A^2 + U_B^2}$ with $U_A = \frac{\sigma}{\sqrt{n}}$ the A-type uncertainty (σ is the square deviation of the statistical series and n the number of measurements, generally more than a hundred to be statistically relevant). U_B is the B-type uncertainties and is evaluated on the repetition of a same measurement 50 times.

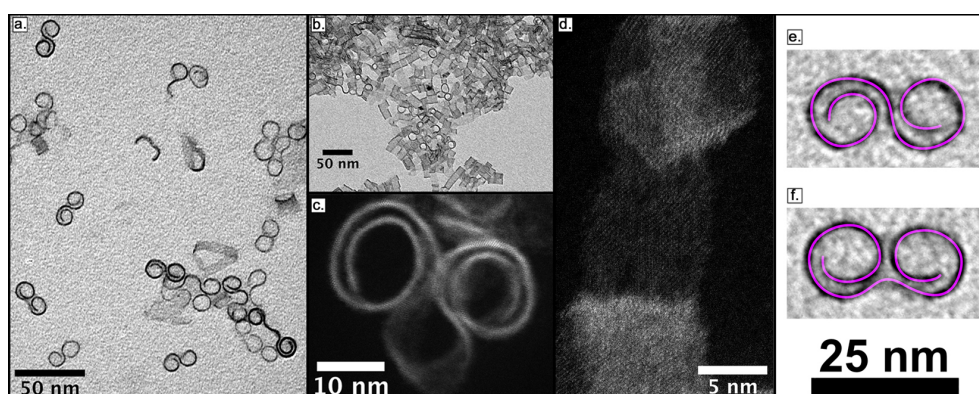


Figure 3.2 – (a.) TEM image of coiled InS NR lying edge-on - (b.) TEM image of coiled InS NR lying flat - (c., d.) HR-STEM images of a coiled InS NR lying edge-on (c.) and flat (d.). Acquired with the help of Benoit Mahler from the ILM Lyon. – (e., f.) TEM images of on-edge coiled NR, illustrating by the violet curve the “in-out” conformation (e.) and the “in-in” conformation (f.).

to an equal stoichiometry in In and S. We then deduced the empirical formula of InS for the NR.

To determine the NR crystallographic structure, we performed X-ray diffraction (Figure 3.3). Nevertheless, we were not able to find a crystallographic structure of InS that matches directly the NR experimental X-ray diffractogram. Indeed, the experimental diffractogram presents three main broad peaks at 24.7° , 33.8° and 44.3° , eight others of low intensity (18.5° , 39.3° , 47.3° , 48.3° , 54.1° , 56.4° , 58.9° and 70.8°) and two intense and narrow peaks at 27.2° and 29.2° .

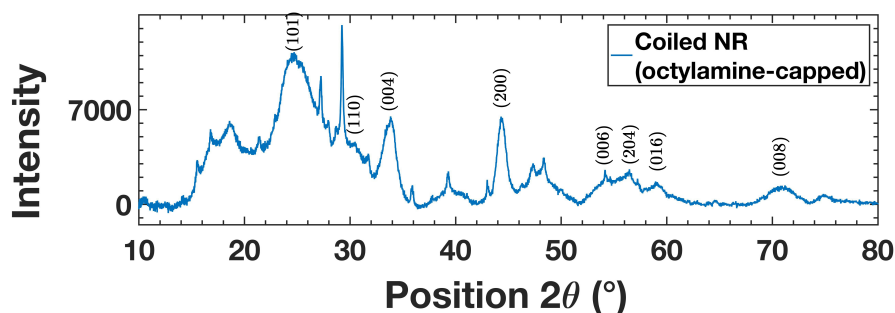


Figure 3.3 – XR diffractograms of coiled octylamine-capped indium sulfide nanoribbons. Attributed peaks are the ones inherent to InS NR (see next paragraph) and are in agreement with diffraction peaks positions of orthorhombic $Pn\bar{m}$ InS crystallographic structure (ICDD card n°01-072-0551).

According to Scherrer’s equation, these two last narrow peaks at 27.2° and at 29.2° correspond to large crystalline domains and are not typical in terms of broadness of diffraction peaks obtained for nano-sized objects [117]. Indeed, the crystalline domains associated to these two peaks are respectively of 83 nm and 66 nm. This is 3 to 8 times bigger than the crystalline domains evaluated for the peaks at 24.7° , 33.8° and 44.3° which are respectively of 10 nm, 21 nm and 15 nm. These peaks at 27.2° and at 29.2° do not correspond to traces of precursors still present in the medium, as XRD of sulfur powder and indium acetate do not present diffraction peaks at these positions.

To explain the presence of these peaks, we suggested bigger crystalline particles might form in parallel of NR. To know the exact atomic composition of the overall

sample, we carried on X-Ray photoelectron spectroscopy (XPS) measurements (Figure 3.5). In that sense, XPS is a more reliable method than RBS, in the meaning RBS is a technique sensitive only to heavy elements (see RBS sidebar in section 2.3 on page 38). Heteroatoms such as oxygen - that may compose part of the sample for instance in the form of indium oxide - are then not detected in RBS.

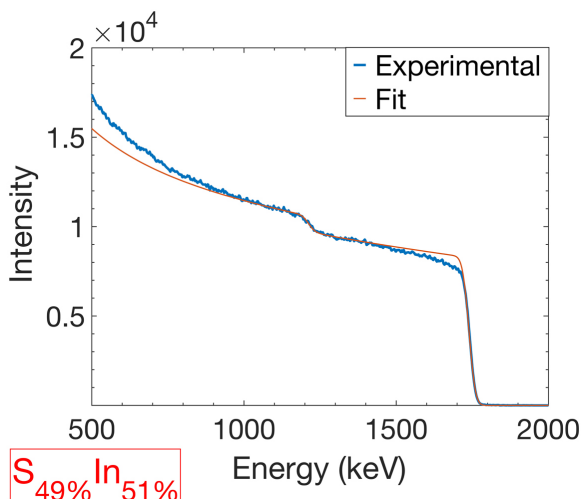


Figure 3.4 – RBS spectrum for NR: the experimental data are fitted in order to obtain the chemical composition of the sample, written below the spectrum. The spectrum and its interpretation were realized with the help of Bruno Canut from the Institute of Nanotechnologies of Lyon.

XPS data interpretation gives the following atomic composition of the sample: C (43.3%), O (18.9%), S (14.7%), In (16.3%), N (4.8%). Nitrogen is entirely due to octylamine molecules bonded at the surface of the material. Sulfur is present predominantly in the form of sulfide (Figure 3.5.d.) with some traces of sulfate. As regards oxygen, half is involved in C-O bonds (i.e. 9.45%) as part of ethanol surface ligands (ethanol is present in the reaction medium and is used as an antisolvent during purification process), the other half is under the form of oxide (Figure 3.5.c.). Carbon belongs to ethanol and octylamine molecules grafted on the surface of the particles. Indium is present under the oxide and sulfide forms (Figure 3.5.b.). Excluding the atomic proportion of oxygen involved in ligand composition (i.e. 9.45%), the overall material seems to be a mixture of indium sulfide particles and indium oxide particles ($x.\text{In}_A\text{S}_B$, $y.\text{In}_C\text{O}_D$) with the global empirical formula $\text{In}_{1.72}\text{S}_{1.56}\text{O}$. Variables A, B, C and D are the stoichiometric coefficients associated respectively to In and S in the sulfide, and In and O in the oxide. Variables x and y are the molar fractions of each species and are at this stage not accessible. By exploring Material Project or ICDD crystallographic databases, only four indium oxide forms are reported: In_2O_3 , InO_2 , InO_3 and InO . We find then the four following couples of indium-based materials which are in agreement with atomic proportions given by XPS: $\text{In}_2\text{O}_3/\text{In}_2\text{S}_3$, $\text{InO}_2/\text{In}_3\text{S}_4$, InO_3/InS and InO/InS_2 . Moreover, the following system of equation is obtained^b:

$$\left\{ \begin{array}{l} x.A + y.C = 1.72 \\ x.B = 1.56 \\ y.D = 1 \\ x + y = 1 \end{array} \right. \quad (3.1)$$

b. This system is hardly resolvable as we can only fix the ratios A/B or C/D. It is then not possible to get directly access to the value of x or y.

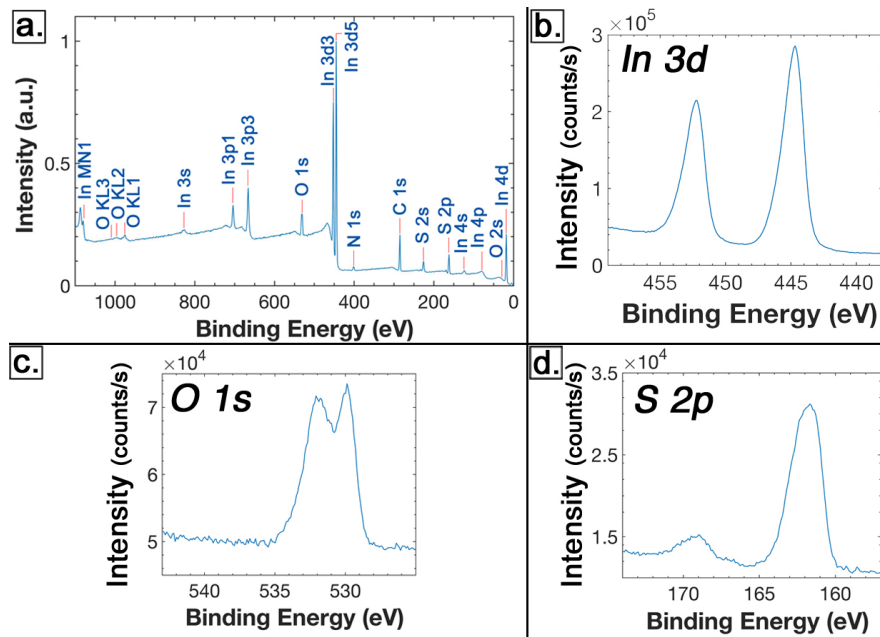


Figure 3.5 – XPS analyses: (a.) XPS patterns for survey of NR, proving the atomic presence of In(16.3%), S(14.7%), O(18.9%), C(45.3%), N(4.8%) - High-resolution spectra highlighting the presence of: (b.) In in the form of sulfide and/or oxide ; (c.) O in the form of oxide ($\sim 50\%$) and ligand ($\sim 50\%$) ; (d.) S mainly in the form of sulfide (peak at 162 eV). Some is founded to be in a sulfate or sulfonate form ($< 10\%$, peak at 169 eV)

Besides, we suggested from TEM and HAADF-STEM observations that NR are made of a single material (i.e. indium sulfide) and that bigger particles (i.e. indium oxide) are formed in parallel in the medium. The presence of such indium oxide material is not clearly highlighted on electron microscopy. Nevertheless, we punctually remark on some TEM observations large areas of blurry and hardly distinguishable material in addition to NR that may be interpreted as indium oxide material. Figure 3.6 shows TEM images displaying such areas, often found along NR agglomerates.

To confirm our hypothesis, we performed Energy Dispersive X-Ray Spectroscopy (EDX) and made an elemental mapping of the sample at the nanoscale (Figure 3.7).

About Energy Dispersive X-Ray Spectroscopy (EDX)

The principle of EDX is to excite, thanks to an electron beam, an inner shell electron of an atom which is ejected from it. The hole created by this electron is filled by an outer higher energy shell electron. This phenomenon occurs with the emission of an X-ray radiation. The energy of the emitted X-ray radiation is characteristic of the element and EDX permits to access locally to the atomic composition of the sample.

We deduce from these analyses two main assertions: first, the NR are only made of indium and sulfur (Figure 3.7.b.). Oxygen, which is present all other the mapped area, is not a constituent of the NR (Figure 3.7.c.). Secondly, the atomic ratio on the scanned area between sulfur and indium is of 0.72. The expected ratio of 1 is not reached maybe because of the presence of indium oxide in the mapped area, that leads to an excess of indium atoms compared to sulfur atoms in the sample. We thus considered the NR empirical formula is indeed InS.

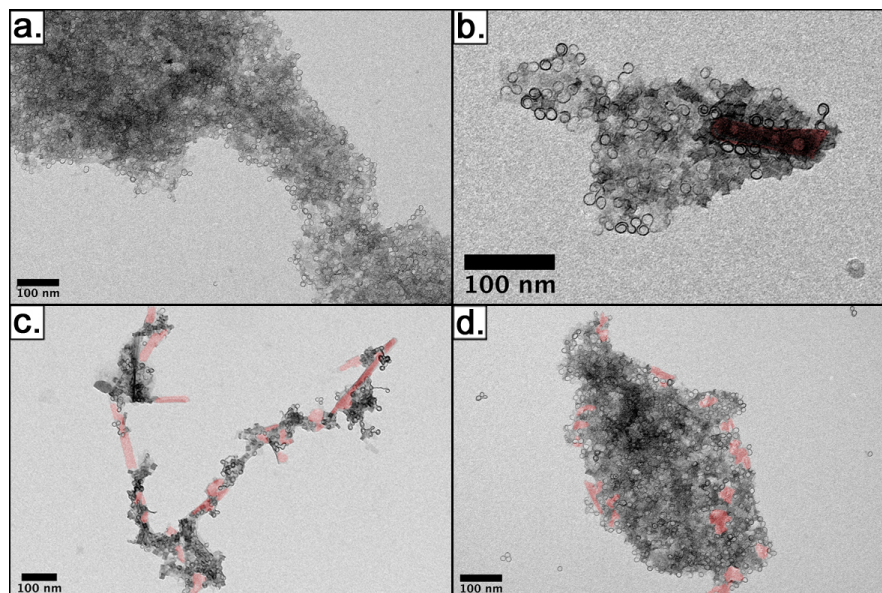


Figure 3.6 – TEM images showing blurry areas of unshaped large material along NR that might be attributed to indium oxide. The presence of this material, mainly along NR agglomerates, is highlighted in red in (c.) and (d.).

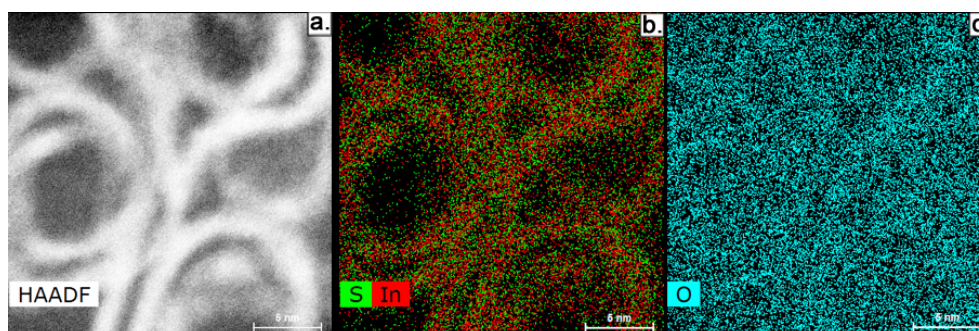
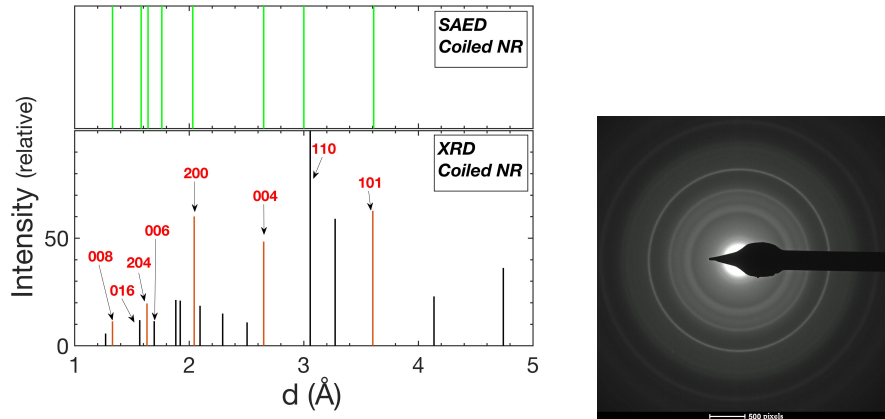


Figure 3.7 – Elemental mapping of a coiled NR sample by Energy Dispersive X-Ray Spectroscopy (EDX): (a) HAADF-STEM image showing the area of the sample selected for EDX elemental mapping - (b.) Indium and sulfur elemental mapping - (c.) Oxygen mapping. These analyses were conducted by Gilles Patriarche at the Centre de Nanosciences et de Nanotechnologies of Paris-Saclay.

Among all the diffraction peaks of the X-ray diffractogram (Figure 3.3), we were able to isolate the ones due only to InS NR thanks to Selected-Area Electron Diffraction (SAED). SAED was realized in parallel of HAADF-STEM experiments on coiled InS NR by Gilles Patriarche (C2N Paris-Saclay). Each ring seen on the SAED pattern (Figure 3.8.b.) is associated to a precise interplanar distance in the NR crystallographic structure. These distances can be evaluated from the measure of the radius of each ring^c and after calibration of the camera on a GaAs single crystal oriented following the [110] zone axis. The results are shown on Figure 3.8.a (top). For each InS X-ray diffraction peak (Figure 3.3), we can measure the associated interplanar distance thanks to Bragg's law. Results are reported on Figure 3.8.a. (bottom). The eight distances measured from SAED are matching with eight distances measured from XRD: we then attribute the corresponding XRD peaks to be inherent to InS NR, and the rest of the diffraction peaks to other materials (such as indium oxide^d) also present in the sample.



(a) a. Interplanar distances measured from SAED (top) compared to interplanar distances calculated from X-ray diffraction (XRD, bottom). From SAED, we were able to select the peaks in the X-ray diffractogram that really correspond to InS NR. We made the attribution according to orthorhombic $Pn\bar{m}$ InS crystallographic structure (ICDD card n°01-072-0551). Peak in red are those who are shifted after ligand-exchange (see next part).
 (b) b. SAED pattern of InS NR. These analyses were conducted by Gilles Patriarche at the Centre de Nanosciences et de Nanotechnologies of Paris-Saclay.

Figure 3.8 – Selected-Area Electron Diffraction (SAED) experiments.

These NR diffraction peaks present a broadness that is expected from nano-sized material [117]. Moreover, the peaks represented in red on Figure 3.8.a. are the only ones which positions move when changes the conformation of the NR (Figure 3.12), as we will see in the next part 3.2. Therefore, they must be associated to the NR crystallographic structure. Indeed, we describe in this part 3.2 how the tuning of ligand-induced surface stress can change the conformation of the NR from a coiled form to an uncoiled form. This change in surface stress (and so in conformation) necessarily goes along a variation of lattices parameters and thus a change in the position of diffraction peaks according to Bragg's law.

c. For large rings, their radius is defined as the one of the circle corresponding to the maximum diffraction intensity.

d. In_2O_3 is the most likely form of indium oxide present inside the sample according to XPS analyses. Using equation 3.1 with $A/B=1$, we can evaluate $C/D=0.16$, which does not correspond to any known indium oxide structures but which is closest to In_2O_3 stoichiometry. Yet, we were not able to find a known crystallographic structure of In_2O_3 or of another indium oxide (such as In_2O_3) that could match with all other peaks in NR XRD.

These peaks are then attributed to orthorhombic InS material (ICDD card n°01-072-0551) and are indexed as well in Figure 3.3. Shifts in diffraction peaks positions between referenced bulk and coiled NR are observed (see Figure 3.12)^e. This can be explained again as a consequence of an octylamine-induced stress on the NR surface, which thus changes lattice parameters compared to bulk parameters and so interplanar distances. As we can observe, all these peaks correspond to reflections from (h0l) planes. This is consistent with a thickness of the NR along the b-axis: in this case, according to Scherrer's equation, (0k0) reflections should not be visible as few unit cells are present along the b-axis, whereas (h0l) reflections should be seen on XR diffractogram as the associated crystal domains that lead to diffraction are larger [117].

Our assertion is strengthened with the crystallographic modelling of an orthorhombic flat InS NR with a thickness along the b-axis (Figure 3.9). For our model, we took one *Pnmm* orthorhombic InS conventional cell and multiply it 100 times along a-axis, 2 times along b-axis and 10 times along c-axis in order to reflect the experimental NR dimensional ratio.

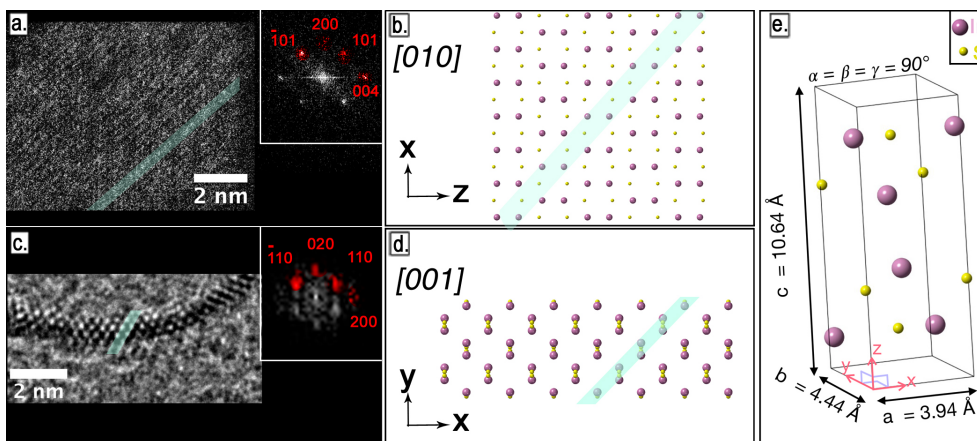


Figure 3.9 – (a.) HAADF-STEM image of a NR lying flat. Inset: Fourier transform of this image that corresponds to the modelled electron diffraction of orthorhombic InS whose indexation is given in red figures - (b.) View of a modelled orthorhombic InS NR along the [010] zone axis. In the model and in the HAADF-STEM images, atoms are aligned in rows, oriented at approximately 45° from the edge (see highlighting). - (c.) Bright-field STEM image of a NR viewed edge-on. Inset: Fourier transform of this image that corresponds to the modelled electron diffraction of orthorhombic InS whose indexation is given in red figures - (d.) View of a modelled orthorhombic InS NR along the [001] zone axis. In the model and in the HAADF-STEM images, atoms are both aligned in rows, oriented at approximately 40° from the edge (see highlighting). - (e.) Scheme of an orthorhombic *Pnmm* InS conventional cell, from ICDD card n°01-072-0551. STEM images were realized with the help of Benoit Mahler from the ILM Lyon, Marta de Frutos from the LPS Orsay and Gilles Patriarche from C2N Palaiseau.

First, microscopy experiments show the presence of a quaternary symmetry axis in the NR structure when we observed it in a direction either parallel or perpendicular to the thickness direction: Fourier transforms of STEM images, available in Figure 3.3.a. and 3.3.c., match with electron diffractions of modelled orthorhombic InS along these directions.

Secondly, the atomic disposition observed under HAADF-STEM is reflected in our model. Row of atoms (experimentally oriented at approximately 45° from the edge)

e. The relative difference between the experimentally measured interplanar distance and the one from the reference (i.e. the bulk) could reach 3% to 5%.

are observed in both case for a lying-flat observed NR (Figures 3.3.a and 3.3.b). When we observe the modelled NR lying on its edge (Figure 3.3.d.), its atomic disposition is also consistent with our experimental observations (rows of 4 atoms or pairs of atoms that are experimentally oriented at approximately 40° from the edge, cf bright-field STEM image in Figure 3.3.c.). Nevertheless, the low definition of STEM images does not allow us to accurately measure atomic distances or angles and so to compare them in a relevant way with our model. Further high resolution TEM observations are thus needed to conclude about the exact atomic disposition in NR.

Recent high resolution STEM observations (Figure 3.9.c.) allows us to precisely determine the NR thickness of 0.8 nm. This is less than the statistically measured thickness value of (1.3 ± 0.2) nm we reported before: indeed, we might have previously overestimated this value as we measured it from TEM images that have not such an atomic resolution^f. If we take into account this new NR thickness value of 0.8 nm, it is in agreement with the one measured on our model. NR are then of two unit cells thick of orthorhombic *Pnm* InS along the b-axis (Figure 3.9.e.).

Finally, we performed UV-visible spectroscopy of NR in cyclohexane (Figure 3.18.a). They present three narrow peaks of absorption at 255 nm, 261 nm and 269 nm and a broad absorption band from 300 nm to 400 nm (Figure 3.18). Light scattering is also noticed on the UV-vis spectrum of NR, as their colloidal stability is low. Indium sulfide nanoribbons present no photoluminescent properties.

InS orthorhombic single crystal present an optical band gap of 2.09 eV [114]. This value is far below the transition energy we measure on the absorption spectrum of the NR, which is of 4.75 eV for the transition centred at 261 nm. Such a difference from bulk value can be explained by the strong quantum confinement that occurs along the thickness of the NR and that modifies drastically the optical properties of the material.

f. Again, further high resolution TEM observations are needed to determine accurately and statistically the NR thickness.

3.2 Conformation control by ligand exchange

An outstanding feature of these NR is their coiled shape in solution after their synthesis in octylamine. Controlling their conformation by the accurate tuning of their curvature is a great challenge to achieve, as this could have tremendous impact on their optical properties for instance, as proved on other materials in section 1.3. We then undertook the uncoiling of these NR via ligand exchange (Figure 3.10).

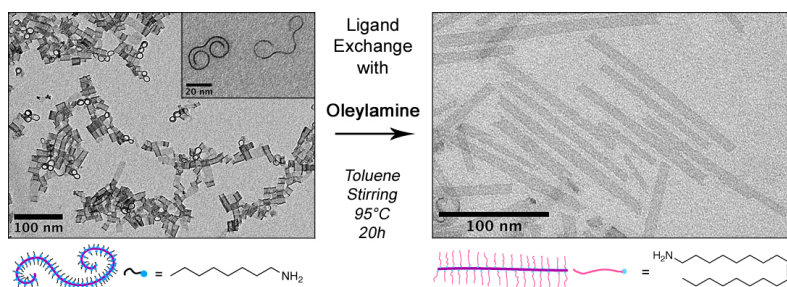


Figure 3.10 – Conformational control of nanoribbons by ligand exchange. Left: TEM images of coiled octylamine-capped NR viewed lying flat or (insert) on edge - Right: TEM images of uncoiled oleylamine-capped NR viewed lying flat.

Purified octylamine-capped indium sulfide NR (0.22 mg/mL) are mixed with a 1.2M oleylamine solution in toluene. The vial is sealed and heated 20h under gentle agitation at 95°C (See the experimental section for more details). After purification using ethanol, the white product is dispersed in toluene and characterized by TEM (Fig. 3.11). We expect that the large excess of oleylamine with respect to the bound surface octylamine, coupled to the large reaction temperature ensures that the ligand exchange takes place under these experimental conditions.

A lower reaction time (e.g. 2h, 5h) allows the unfolding of only a fraction of the NR. Toluene is chosen for its high boiling point (110°C), as tests at lower temperature (e.g. room temperature or 60°C) and in other solvents (e.g. cyclohexane that boils at 81°C) were not successful. The concentration in oleylamine was optimized such as all the sample is uncoiled after 20h at 95° in toluene.

After the ligand exchange with oleylamine, TEM images displays uncoiled and flat indium sulfide NR. The uncoiling is attributed to the exchange of native octylamine with oleylamine. This uncoiling is not due to an exposition of NR at high temperature since a control sample of InS NR in toluene heated in the same experimental conditions still presents coiled NR. The average curvature radius of octylamine-capped InS NR before and after heating is calculated from TEM images thanks to a semi-automatic image treatment algorithm (see sidebar on page 78 for details) and remains in both cases the same of (5.6 ± 0.1) nm, confirming that heating does not affect the conformation of the nano-object and is just necessary to kinetically favour the ligand exchange.

We carried out statistical measurements over 350 uncoiled NR to get their average dimensions. The InS uncoiled NR are of (152 ± 4) nm in length for (9 ± 2) nm in width. These value are consistent with the ones we measured on coiled NR.

Uncoiled oleylamine-capped NR present a far better colloidal stability than coiled octylamine ones in toluene: that can be explained by the better solubility oleylamine have with toluene than octylamine.

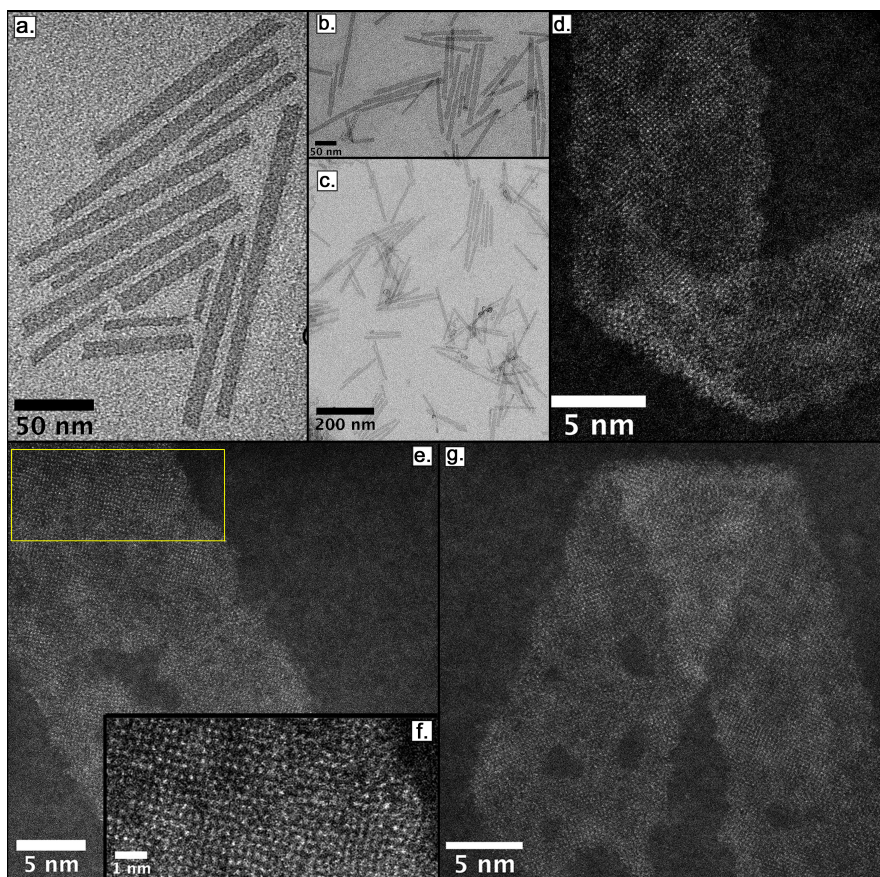


Figure 3.11 – (a.), (b.), (c.) TEM image of unfolded oleylamine capped indium sulfide NR lying flat at different magnifications - (d., e., f., g.) HAADF-STEM images of unfolded NR lying flat. The observed folding here is just due to drying effect on TEM grid. The holes observed in the structure of the NR is due to a fast degradation of the ultrathin NR under electron beam. Inserts (f.) is the enlargement of the yellow box of (e.). HAADF-STEM images were realized with the help of Benoit Mahler from the ILM Lyon.

XRD pattern of uncoiled indium sulfide NR presents the same peaks as coiled indium sulfide NR (Fig 3.12). The narrow and intense peak at 20° on the uncoiled oleylamine-capped NR diffractogram is attributed to remaining free oleylamine from the uncoiling process, despite the purification step. X-ray diffractogram of oleylamine is available on Figure 2.6 on page 39 from last chapter.

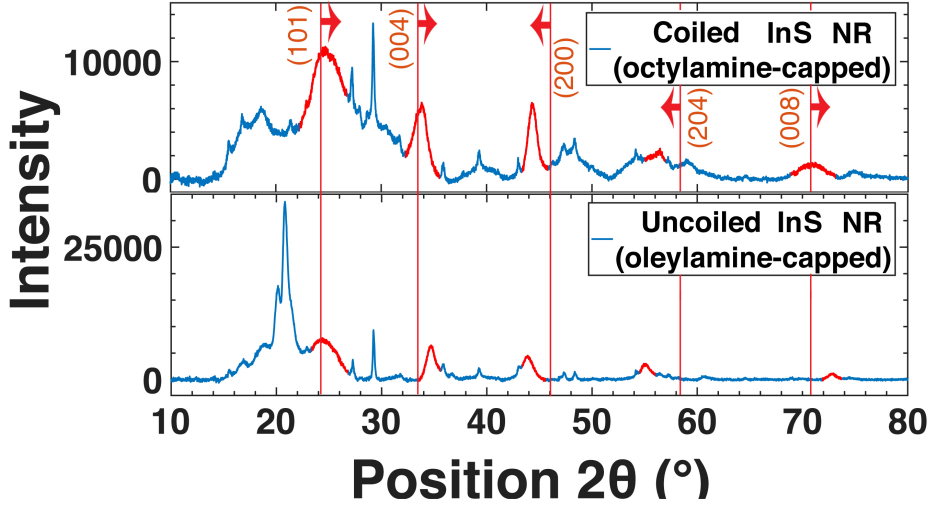


Figure 3.12 – XR diffractograms of: (a.) Coiled octylamine-capped InS nanoribbons – (b.) Uncoiled oleylamine-capped InS nanoribbons. Peak shifting as regards bulk orthorhombic $Pnnm$ InS diffraction peak (ICDD card n°01-072-0551) positions is highlighted by red lines and arrows.

Compared to the diffractogram of coiled octylamine-capped indium sulfide NR, a shift in diffraction peak positions is observed for uncoiled oleylamine-capped indium sulfide NR. Diffraction peaks of both diffractograms are shifted as regard bulk orthorhombic InS diffractogram (see red lines in Figure 3.12). These shifts can be explained as a result of a stress imposed by the organic ligands to the surface, thus modifying the lattice parameters and therefore the diffractogram. Indeed, a compressive stress along one direction will shorten the distance between planes that get their normal vector along this direction: according to Bragg's law, the glancing angle has to increase to recover constructive interferences. For instance, in the case of the (004) diffraction peak, oleylamine impose a much compressive surface stress than octylamine: according to notations introduced in table 3.1, the relative variation in interplanar distance (i.e. the strain) compared to the coiled (octylamine-capped) case is negative ($\delta_d = -2.4\% < 0$) and the one in diffraction peak position is positive ($\delta_\theta = \frac{\theta_{uncoiled} - \theta_{coiled}}{\theta_{coiled}} = 2.6\% > 0$).

On the other hand, a tensile stress will negatively shift the value of the glancing angle to recover diffraction. For example, in the case of the (200) diffraction peak, oleylamine impose a much tensile surface stress than octylamine: still according to the notations in table 3.1, $\delta_d = 2.2\% > 0$ and $\delta_\theta = -1.1\% < 0$. This is a proof that octylamine and oleylamine impose different stresses (compressive and tensile depending on the planes) at the surface of NR. They both exert compressive stresses on (101), (004) and (008) planes and a tensile stress on the (200) and (204) planes (see Figure 3.12 and Table 3.1) as regards bulk orthorhombic $Pnnm$ InS. The amplitude of these stresses are different according to octylamine or oleylamine, as pointed out by the different strain they impose on a same plane (see Table 3.1).

Let us take the particular case of atoms in (004) planes. According to our crystal

model (Figure 3.9), a stress imposed on these planes is a stress imposed along the direction of the width of the NR (c-axis). We have just demonstrated this stress is compressive, let us now wonder at which extent it may impact the overall width of the NR. Let us hypothetically consider an orthorhombic InS NR of 9 nm in width without any ligand at its surface (i.e. in a bulk form). Dividing its width by the distance between two (004) planes ($d_{ref} = 2.66 \text{ \AA}$) gives us 33 (004) planes along the width of the modelled NR. If octylamine is now bonded to the surface of the NR, there is a variation in the distance between two (004) plane of $\Delta_d = d_{coiled\ NR} - d_{ref} = -0.01 \text{ \AA}$. By multiplying this distance variation by the number of (004) planes along the width, we are able to determine the overall width variation of $33 \times \Delta_d = 33 \times -0.01 = -0.33 \text{ \AA}$. By octylamine bonding, the NR width is then shortened by 0.33 \AA . By the same reasoning with oleylamine instead of octylamine at the surface of the NR, we can show the NR width is shortened by 2.52 \AA as regards the bulk form, that is to say 7.7 times more than with octylamine.

In anyways, the difference in magnitudes between octylamine and oleylamine surface stresses may explain the difference in the morphology adopted by the indium sulfide NR (i.e. coiled or flat).

Table 3.1 – Shifts of diffraction peaks between coiled octylamine-capped NR and uncoiled oleylamine-capped NR.

Diffraction peak	(101)	(004)	(200)	(204)	(008)
$2\theta_{coiled}$	24.7°	33.8°	44.3°	56.4°	70.9°
$2\theta_{uncoiled}$	24.3°	34.7°	43.8°	55.1°	72.9°
δ_d	1.5%	- 2.4%	1.1%	2.2%	- 2.4%
δ_{coiled}	-2.5%	- 0.4%	3.7%	3.0%	-0.2%
$\delta_{uncoiled}$	-1.0%	- 3.0%	4.8%	5.2%	-2.5%

- The first line gives the attribution of diffraction peaks to the ones of orthorhombic $Pnmm$ InS crystallographic structure (ICDD card n°01-072-0551).

- $2\theta_{coiled}$ and $2\theta_{uncoiled}$ are their positions in the diffractograms of respectively coiled octylamine-capped and uncoiled oleylamine-capped NR, available in Figure 3.12.

- δ_d is the strain (i.e. the relative variation in interplanar distance d , which is the distance between two successive atomic (hkl) planes) of the uncoiled conformation as respect to the coiled conformation, defined as: $\delta_d = \frac{d_{uncoiled} - d_{coiled}}{d_{coiled}}$. Bragg's law allows to express the distance d between two successive atomic planes as a function of the glancing angle θ (i.e. angle between the plane of the surface and the incident X-Ray beam of wavelength λ) as followed: $2d \cdot \sin\theta = n \cdot \lambda$, with n the diffraction order. We can thus express $\delta_d = \frac{\sin(\theta_{coiled}) - \sin(\theta_{uncoiled})}{\sin(\theta_{uncoiled})}$.

- In the same manner, δ_{coiled} (resp. $\delta_{uncoiled}$) is the strain of the coiled (resp. uncoiled) conformation as respect to the bulk (ICDD card n°01-072-0551), and is calculated as $\delta_{coiled} = \frac{\sin(\theta_{bulk}) - \sin(\theta_{coiled})}{\sin(\theta_{coiled})}$ (resp. $\delta_{uncoiled} = \frac{\sin(\theta_{bulk}) - \sin(\theta_{uncoiled})}{\sin(\theta_{uncoiled})}$).

To better understand the role of alkyl chain length of the ligand in the uncoiling of the NR, we performed several ligand exchange experiments with primary alkylamines of several different linear saturated carbon chains. The native octylamine from the surface of the NR is thus replaced by a shorter carbon chain amino ligand (n-butylamine) and several longer carbon chain amino ligands: dodecylamine, tetradecylamine, hexadecylamine and octadecylamine. The experimental protocol is identical to the one described for ligand exchange with oleylamine and is described in the experimental section. The resulting NR are then characterized by TEM (Figures 3.14, 3.15 and 3.16), from which the average curvature radii of the NR are calculated using a semi-automatic image treatment algorithm (Figure 3.13).

About the semi-automatic image treatment algorithm

To quantify the coiling inside a sample, we use a semi-automatic image treatment algorithm (ImageJ plugin Kappa [140]) which detects the contour of the nanoribbon, measures the curvature along its length and computes the mean curvature and thus the average curvature radius of the NR.

The Fiji plugin Kappa allows the modelling of the curve adopted by a NR viewed along its side on TEM images from an initialization curve created manually by a point-click method (see Figure 3.13).

The initialization curve is then fit by the software to the underlying data using an iterative minimization algorithm that uses cubic B-splines (i.e. parametric piecewise 3^{rd} degree Bézier curves).

Considering one NR and for each point on the line is then calculated the curve length, the curvature κ and so the radius of curvature ρ which is defined as the inverse of κ . This radius of curvature is then averaged for the whole modelled NR: by repeating this procedure to a hundred of NR of the sample, we are then able to give an averaged and global radius of curvature of the NR inside the sample.

The associated uncertainty U of this global curvature (or of the radius of curvature) is calculated as follows: $U = \frac{2 \cdot \sigma}{\sqrt{n}}$ with σ the square deviation of the statistical series and n the number of measurements (i.e. the number of NR of the sample for which we measure the curvature, generally around a hundred) ^a.

^a. As regards uncertainties, we take into account only A-type uncertainty for curvature measurements, as B-type uncertainties are evaluated as much smaller than A-type uncertainty (This is not the case for the measurement of the dimensions of flat NR, where A-type uncertainty U_A and B-type uncertainties U_B have both to be taken into account).

The results of these analyses are given in Table 3.2 and are compared with the ones of a control sample of native octylamine (C8)-capped indium sulfide NR in toluene, just heated 20 hours under low agitation at 95°C.

With a shorter carbon chain amine (e.g. n-butylamine (C4)), the NR display a smaller curvature radius and thus are more heavily bent than in the control sample (i.e. with octylamine (C8)). With a longer carbon chain amine (e.g. dodecylamine (C12), tetradecylamine (C14) or hexadecylamine (C16)), the NR show a larger curvature radius and thus are less coiled until being completely unfolded with octadecylamine (C18), the saturated equivalent of oleylamine (Figure 3.14, 3.15). Thus, the longer the carbon chain of the amine ligand, the greater the uncoiling.

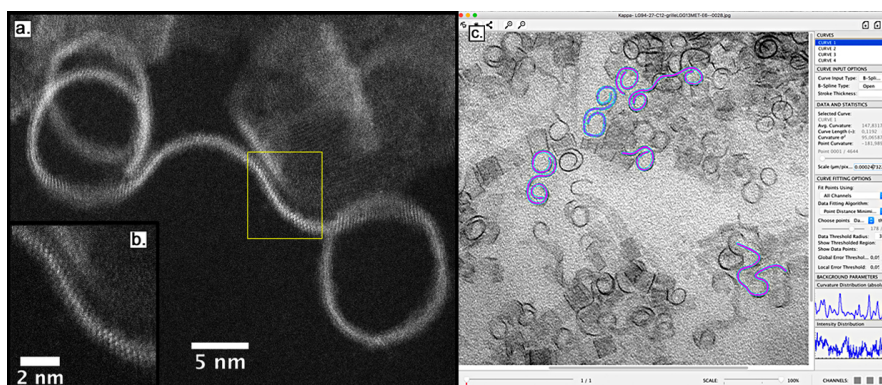


Figure 3.13 – (a., b.) HAADF-STEM images of octylamine-capped coiled InS NR lying on-edge, highlighting the high degree of curvature of these nano-objects. Inserts (b.) is the enlargement of the yellow box of (a.). Acquired with the help of Benoit Mahler from the ILM Lyon. - (c) Screenshot of Kappa plugin interface: in purple is represented the fit curve obtained from an initialization curve created by a point-click method and which follow the observed curve of the NR.

Table 3.2 – Average curvature radius according to the length of the carbon chain of the amino-ligand exchanged with native octylamine.

Amino-ligand used for the exchange	Number of carbon atoms of the linear carbon chain	Average curvature radius
Butylamine	C4	(5.4 ± 0.1) nm ^a
Native Octylamine	C8 (control sample)	(5.6 ± 0.1) nm ^b
Dodecylamine	C12	(7.1 ± 0.2) nm ^c
Tetradecylamine	C14	(6.2 ± 0.2) nm ^d
Hexadecylamine	C16	(6.3 ± 0.1) nm ^e
Octadecylamine	C18 -saturated	Uncoiled
Oleylamine	C18 - unsaturated	Uncoiled

Averaged from ^a 98, ^b 68, ^c 123, ^d 115 and ^e 135 measurements (See Figure 3.13).

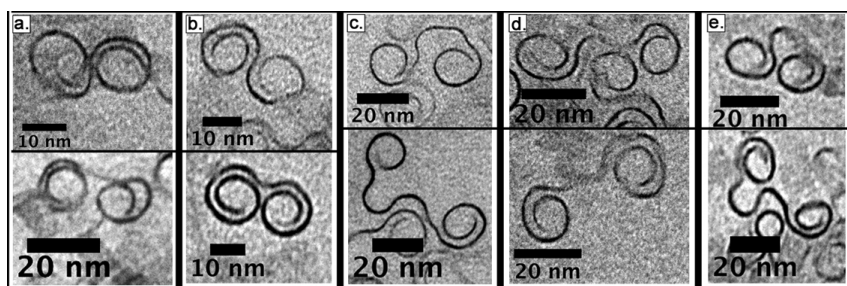


Figure 3.14 – TEM images of indium sulfide NR TEM capped with : (a.) butylamine - (b.) octylamine - (c.) dodecylamine - (d.) tetradecylamine - (e.) hexadecylamine.

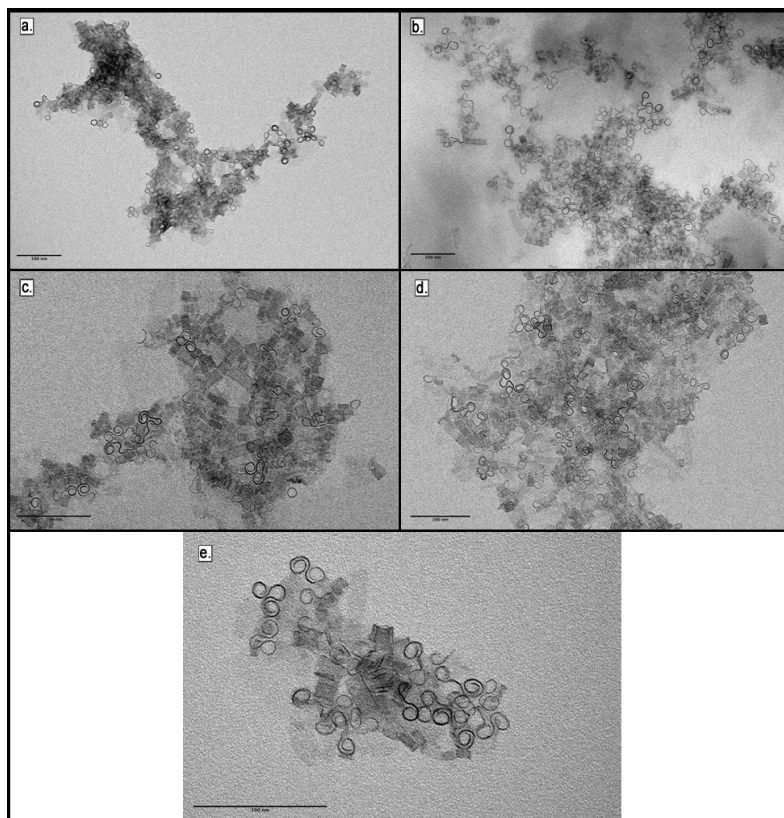


Figure 3.15 – TEM images of indium sulfide NR TEM capped with : (a.) butylamine - (b.) dodecylamine - (c.) tetradecylamine - (d.) hexadecylamine - (e.) native-octylamine

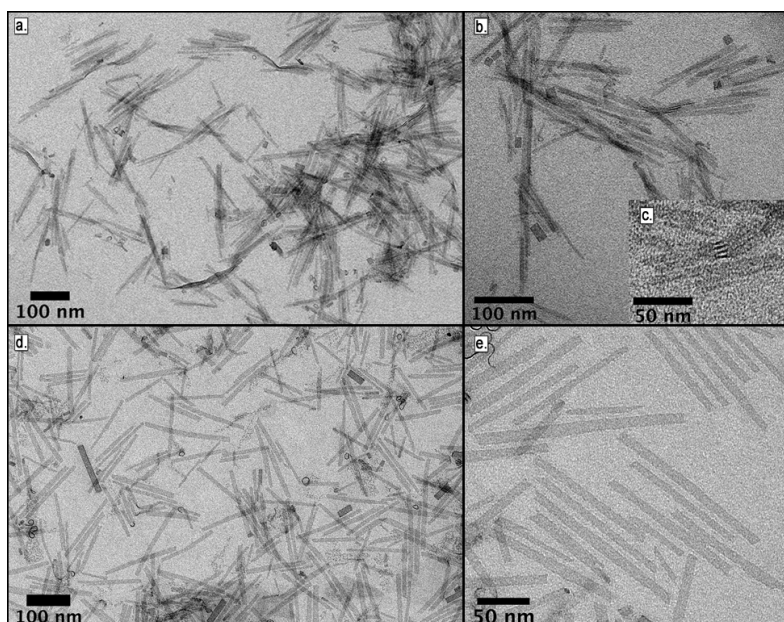


Figure 3.16 – TEM image of indium sulfide NR capped with octadecylamine (overall view : (a., b.), twisting : (c.)) and oleylamine (d., e.).

TEM images of octadecylamine-capped InS NR (Figure 3.16) show uncoiled NR with a slightly different morphological aspect than the one of oleylamine-capped NR. Some octadecylamine-capped InS uncoiled NR seems a bit bent (Figure 3.16.a), few others are twisted (Figure 3.16.c.) giving them a thinner aspect than oleylamine-capped NR. The agglomeration of the unfolded NR is much more important in the sample with octadecylamine. This can be explained by a cooperative effect between NPL during aggregation. The double bond carbon-carbon in oleylamine can be responsible of this difference in aspect, by arranging the ligand molecules differently on the surface of the NR. That organization would result in different steric and electrostatic repulsions between ligands, a different stress on the surface induced according to octadecylamine or oleylamine ligand, and thus a different morphological aspect.

To further confirm the gradual uncoiling of the NR according to the amino-ligand exchanged, we performed synchrotron Small-Angle X-Ray Scattering (SAXS). SAXS is a key technique to assess nanoparticle structural informations in solution and more specifically their curvature radius [66, 134, 141].

The measures were realized at SOLEIL synchrotron, using capillaries of amines capped indium sulfide NR. The results are reported on Figure 3.17. Even if a full modelling study would be required to extract from SAXS pattern an analytical expression and value of the curvature radius, we can already make some assertions. Indeed, as it was already reported for curved CdSe NPL [66], we report the correlation between the position in q of the first SAXS intensity minima with the TEM measured value of the curvature radius. As the curvature radius of the NR increase, the first minimum shift towards lower q (Figure 3.17). The discrepant value for hexadecylamine capped sample explained above is also reflected here in SAXS. SAXS intensity evolutions and TEM measurements of curvature radius are thus in perfect agreement.

The smaller value of curvature radius obtained for tetradecylamine compared to the one with dodecylamine is at odds with the overall trend. This can be explained by the smaller solubility of tetradecylamine in toluene. Thereby, we can suppose the ligand exchange is not fully achieved as less amine is available in the medium for the exchange. This would result in a mixture of octylamine-capped indium sulfide NR and tetradecylamine-capped indium sulfide NR and thus a lower average curvature radius than expected. This rationale can also explain the behaviour of hexadecylamine, whose solubility is similar to the one of tetradecylamine in toluene.

Finally, this change in conformation of indium sulfide NR from coiled to uncoiled is concomitant with a change in their optical properties. Indeed, both NR present three absorption peaks at 255 nm, 261 nm and 269 nm, coiled NR get an additional broad absorption band from 300 nm to 400 nm (Figure 3.18). That difference in UV-visible absorption is responsible of the difference of color adopted by powders of coiled NR (yellow) and uncoiled NR (white): see Figure 3.18. As the change of ligand modifies the surface stress, so can be the lattice parameters of the NR: that could result in a different electron organization between the coiled and uncoiled form and thus different optical features, as it was reported for other nanomaterials (see section 1.3.3). As we already noted, scattering is noticed on the UV-vis spectrum of folded NR: in toluene or cyclohexane coiled NR tend to aggregate and form cloudy yellow solution, which is not the case for uncoiled NR which dispersion is perfectly transparent.

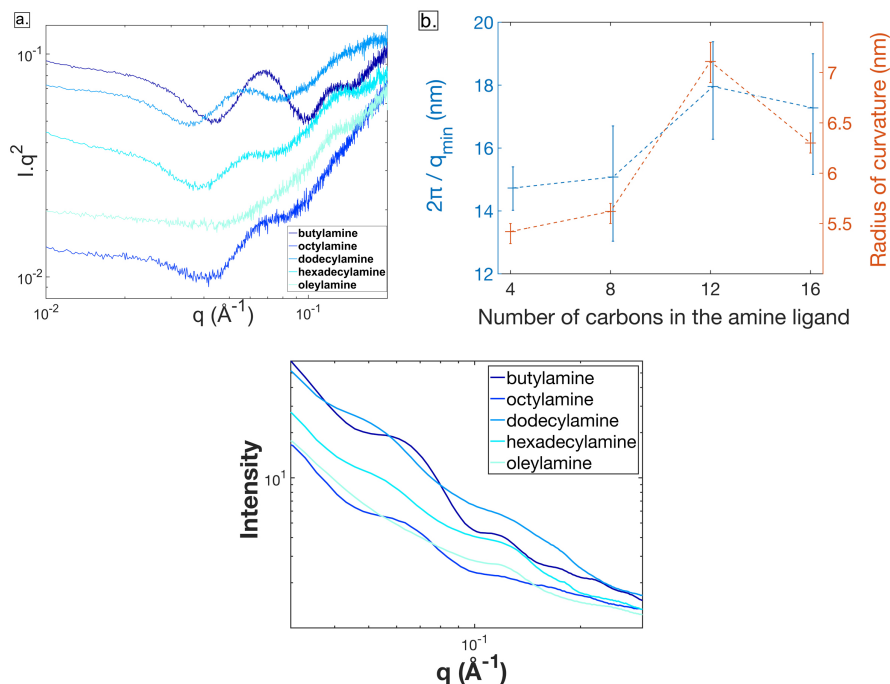


Figure 3.17 – SAXS results : (a.) $I \cdot q^2$ as a function of q , with I the SAXS intensity and q the scattering vector, for amino-ligand capped indium sulfide NR in glass capillaries. This graphic representation allows an enhancement of the variation of intensity with q . Corresponding SAXS pattern is available in Fig S8. (b.) Correlation between the calculated distance in SAXS $2\pi/q_{min}$, with q_{min} the position of the first intensity minima, and the TEM measured curvature radius of amino-ligand capped indium sulfide NR. (c.) SAXS patterns of amino-ligand capped indium sulfide NR in glass capillaries.

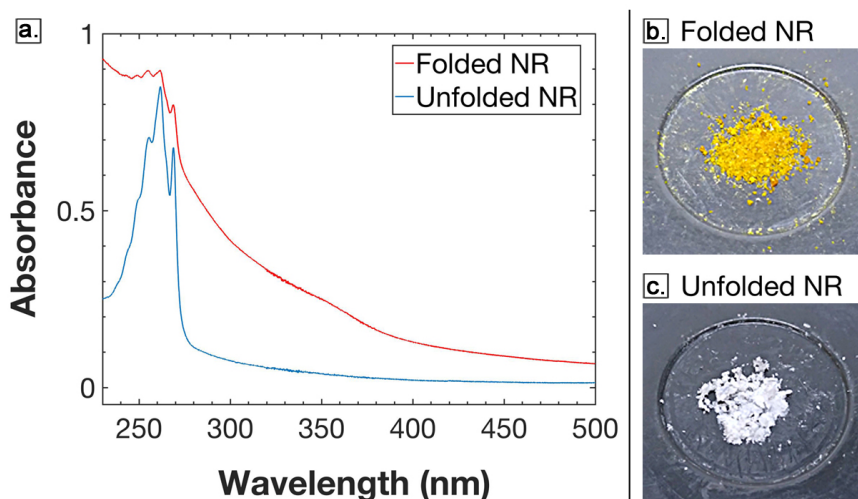


Figure 3.18 – (a.) UV-visible absorption spectra of coiled indium sulfide NR and uncoiled indium sulfide NR in cyclohexane - (b.) Picture of octylamine-capped coiled indium sulfide NR powder - (c.) Picture of oleylamine-capped uncoiled indium sulfide NR powder.

We now turn to the physical interpretation of the curvature tuning as a consequence of surface stress tuning. Let us consider a solid material intersected by a plane such as all atoms and electronic charge densities are removed from one side of this plane. A reorganization of electrons around surface atoms has then to occur. Surface stress represents the difference by unit of length between the new forces needed to maintain unchanged the mean position of surface atoms and the forces they would normally undergo if no surface was created. It can be negative (tensile^g) as well as positive (compressive).

The deposition of adsorbates (i.e. surface ligands) onto the surface modifies greatly the surface stress, as they bond to the surface in a way which does not necessarily correspond to the equilibrium configuration of the crystal. Surface stress then depends on the nature of the adsorbates (e.g. σ -donor or a π -acceptor [71], the length of its alkyl chain [77] (see also section 1.3.3)) and also on their surface density. For instance, adsorption of carbon monoxide on the (100) surface of nickel is reported as tensile at low coverage and compressive for high ligand coverage [142]. Besides, surface atoms can be displaced rapidly and reversibly by ligands [15]: the interplay between surface atoms of a crystal and ligands is strong.

The tuning of surface stress thanks to the use of ligands can then occur according to two scenarios. Either the surface stress originates from differences in ligand coverage, for example with changing the ligand chain length: in that case surface stresses up to 1 N/m can be reported [142]. Or the surface stress originates from dipole-dipole interactions between ligands for a same ligand density considered: in that case surface stresses up to 10^{-3} N/m can be reported [143]. In both cases, surface stresses can force the nanocrystal to adopt a particular shape to minimize its overall elastic energy.

In the case of a ribbon with a surface stress applied on one side, the bending radius is given by the Stoney's formula: $R = \frac{Y \cdot t^2}{6 \cdot \delta\sigma \cdot (1 - \nu)}$ where Y is the Young's modulus, t is the thickness, ν is the Poisson ratio and $\delta\sigma$ is the surface stress^h. In the case of anisotropic material such as NPL, Y and ν have to be replaced by a combination of the elastic tensors components.

The originality of our work lies in the control of curvature through the ligand alkyl chain. In previous reports, folding or unfolding were achieved through the grafting of different functional groups at the surface of NPL (see section 1.3.3 and for instance references [7, 69]). In these cases, the surface stress is tuned by the difference of magnitude in the ligand grafting at the surface of the nanomaterial, where a strain is imposed because of a mismatch between these two different materials.

In the framework of our study, a different phenomenon occurs as we exchange an amine for an amine that only gets a different alkyl chain length. Ligand chain interactions are likely to be much less energetic than covalent interactions between the ligand functional group and the surface. Yet, we demonstrate that such alkyl chain interactions within the ligand monolayer plays a significant role in surface stress. The fact that the shape of ultrathin nanoparticles can be tuned to such an extent by low energy interactions at their surface paves the way towards supramolecular control of nanoparticle conformation.

g. Naturally, surface atoms might get close to bulk atoms in order to recover their original electronic densities, leading to a tensile surface stress. Nevertheless, according to adsorbates in the medium or surface reconstructions, this may not be always the case and surface stress can be null or compressive.

h. By measuring the deflection of a laser beam reflected from the surface and by applying Stoney's formula, one can measure a surface stress: it's the bending method or cantilever method [143].

3.3 Induction of chirality in InS nanoribbons

The first chiral nanomaterials were synthesized by *Elliott, Moloney and Gun'ko*: they reported that D- and L-penicillamine stabilized CdS QD produce mirror image Circular Dichroism (CD) spectra, which is different from the CD spectra of the penicillamine ligands alone [144, 145]. Chiral penicillamine ligands strongly and enantiomerically distorts surface Cd atoms by its binding, transmitting an enantiomeric structure to the surface layers of the QD while the core of the QD remains achiral. Density-Functionnal Theory (DFT) calculations tend to confirm that the ligands pack into helical bands on the surface of the QD and break the mirror symmetry of the surface by this asymmetric bonding, leading to the chirality of the ensemble [145]. The first example of optically active CdSe QD prepared from achiral QD by a post-synthetic ligand exchange was realized in 2013 [146] with L- or D-cysteine. CD is the proof of an optical activity. The CD value at a given wavelength results from the difference between the absorptions of left and right-circularly polarized light.

The experimental protocol we used is inspired and adapted from our previous work on the functionalization of MoS₂ nanosheets with chiral amino-acid ligands [147]ⁱ and previous works of the literature [148, 26].

Chiral ligands available in the lab, L- and D- penicillamine, are thus exchanged with the native octylamine by phase transfer. The procedure is described in the following experimental part. L- or D-penicillamine is dissolved in a water-methanol mixture and the pH is adjusted to 10. Indium sulfide NR in hexane solution is mixed with the aqueous solution and stirred 4 minutes under vigorous agitation. The aqueous phase is then collected and circular dichroism of the sample is measured (Figure 3.19).

Compared to the CD of L- or D-penicillamine alone, we observe the onset of new peaks in the inorganic part of the spectrum from 320 nm to 400 nm, attributed to electron interactions between surface atoms of the NR and the chiral ligand. The chiral ligands on their own show of course also CD due to their direct absorption, whether they are free on the chemical medium or linked to the NR, for wavelength smaller than 300 nm. The CD value is strictly opposite for L-penicillamine and D-penicillamine functionalized indium sulfide NR (i.e. positive and negative Cotton effects are reported).

A material generally exhibits CD in the vicinity of its absorption bands: as free remaining L- or D-penicillamine presents CD signal below 300 nm (that is to say in the same region where NR absorb light), it was not possible to notice intrinsic CD of the NR under 300 nm. Nevertheless, CD is recorded in the 300 nm - 400 nm area, where NR present a broad absorption tail (Figure 3.18). Functionalized NR retain a coiled conformation after observation on TEM grids. As evoked above, the chiral ligand potentially causes the formation of chiral defects at the surface of the nanomaterial and in this way potentially transfers its enantiomeric structure to the surface of the indium sulfide NR.

Different chiral amines or amino-acids were also tested (R- and S-methylbenzylamine, R-2-aminononane, L and D-methionine, L and D-cysteine, L and D-phenylalanine), but only the functionalization with L and D-penicillamine yielded a CD signal.

The reasons why penicillamine induces optical activity whereas other ligands tested did not might be multiple: first penicillamine presents three functional groups

i. Chirality was successfully induced in this system and the presence of chiral ligands causes the preferential folding of MoS₂ nanosheets.

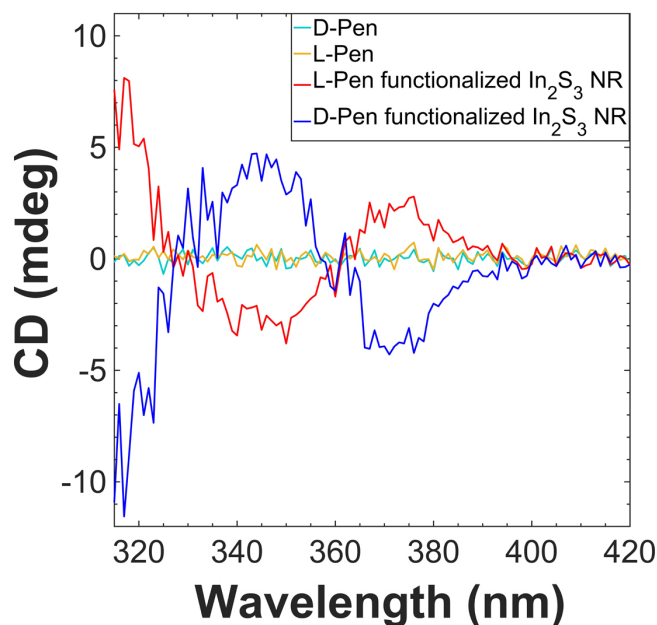


Figure 3.19 – Circular Dichroism spectrum of L- or D-penicillamine (Pen) functionalized indium sulfide NR

to bind at the surface of the NR. It is known indeed that a bidentate interaction (at least) is generally needed from the chiral ligand to induce chirality onto the surface of the NR [149, 150]. In most reported works of the literature [146, 26], one functional group needs to be a thiol while the other is usually a carboxylic acid. In addition, the closer the dissymmetry center of the ligand to the nanomaterial surface, the greater the possibility to induce CD [147]. Such a condition is realized with small chiral ligands such as penicillamine. Finally, penicillamine displays a greater stability in solution than others amino acids as its disulfide formation rate is lower [147], and thus penicillamine has a higher probability to interact with materials.

If such preliminary works on the induction of chirality in indium sulfide NR samples are promising, further work is needed to understand exactly the origin of this induction of chirality.

3.4 Outlooks

By combining TEM, HAADF-STEM, XRD, RBS, XPS, SAED and EDX analyses, we performed a complete characterization of orthorhombic InS nanoribbons synthesized by a solvothermal method. The as-synthesized octylamine capped indium sulfide NR present a strong coiling which can be quantified by TEM mean radius curvature measurements. Ligand exchanges are then performed between native octylamine and primary amines which differ only by the length of their saturated linear carbon-chain.

We show that the curvature, and hence the shape of the NR, can be tuned by the choice of the appropriate surface ligand. Indeed, the longer the carbon chain of the amino ligand, the more the uncoiling. This uncoiling is complete with octadecylamine or oleylamine. We thus demonstrate that alkyl chain weak interactions within the ligand monolayer are of a great importance in the tuning of the surface stress and so the shape of ultrathin NR. This variation of ligand-induced surface stress is reflected in X-ray diffractograms, as diffraction peaks are shifted with the conformation change. Moreover, this change in shape occurs along a change in absorption properties.

Generalizing this method to other materials with valuable optical properties might open a pathway to new optical applications. Indeed, if a change in properties is observed along a change in morphology, controlling accurately the shape of 2D-nanomaterials through surface ligand exchange would represent an efficient post-synthesis method to easily tune their properties.

Complementary works are still in progress on the optimization of NR synthesis. First result shows a reduction of reaction time from 12h to 2h or 4h does not allow the obtaining of coiled NR or with a very reduced yield. The necessity of adding ethanol on the reaction medium is also under investigation, as well as the nature of sulfur precursor. We indeed replaced sulfur powder by thiourea equivalents. It was reported in the literature that the use of different thioureas influences the nucleation kinetics and the size of PbS nanocrystals [151]: the idea was to extend these results to anisotropic nanomaterials such as indium sulfide NR. These works were realized with Marie-Ali  nor Zaretti in the framework of her undergraduate internship at the ENS de Lyon in 2019. We already found a change in sulfur precursor leads to a change in morphology: for instance, the use of 1-(4-trifluorophenyl)-3-phenylthiourea instead of sulfur powder leads to nanodisks of 50nm of diameter, whereas the use of 1-hexyl-3-dodecylthiourea instead of sulfur powder leads to 8nm-sized oval particles (Figure 3.20).

Finally, further investigations on the reversibility of the uncoiling process have to be carried out. We already performed experiments on reverse ligand exchange: uncoiled oleylamine-capped NR were dispersed in an octylamine solution in toluene and stirred one night at 95  C. We did not succeed in recovering a coiled conformation. We hypothesize that the exchange in this direction is not thermodynamically favoured, as uncoiled NR might be in a more stable state than coiled NR because of potential surface stress release in uncoiled conformation.

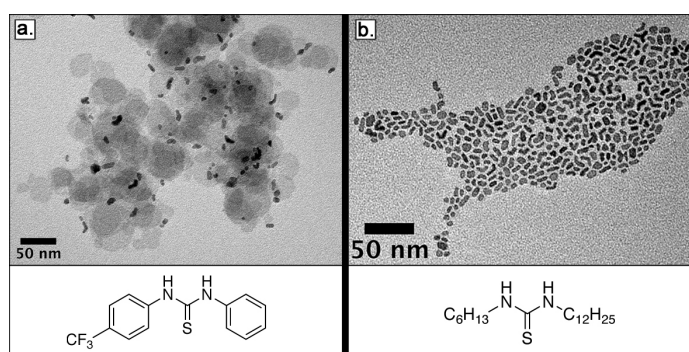


Figure 3.20 – TEM images of nano-objects obtained following the protocol of synthesis of coiled indium sulfide NR, by replacing sulfur powder by (a.) 1-(4-(trifluorophenyl)-3-phenylthiourea and (b.) 1-hexyl-3-dodecylthiourea.

3.5 Materials and experimental methods

3.5.1 Starting Materials and chemicals

Indium (III) acetate (anhydrous, 99.9%), 1-octylamine (99+%), oleylamine (approximate C18-content 80-90%) were purchased from Fisher-Acros Organics. Sulfur (powder, 99.998%), 1-hexadecylamine (98%), dodecylamine (98%) were purchased from Sigma-Aldrich. Tetradecylamine (>96%) was purchased from TCI Europe. Butylamine (99%) and 1-octadecylamine (97%) were purchased from Fisher-Alfa Aesar. Absolute ethanol and toluene (99.5%) were purchased from VWR.

3.5.2 Instrumentation

TEM images were acquired on a JEOL JEM-1400 (accelerating voltage of 120kV) at CIQLE Lyon. The sample are prepared by drop casting InS NR suspensions in toluene onto 200 carbon-coated copper grids. To avoid agglomeration of NR on the TEM grids, the suspension of NR can be beforehand diluted a minima by a factor of ten and sonicated 2 minutes in a bath. InS ultra-thin NR are electron beam sensitive and may deteriorate in a few seconds.

Part of HR-STEM pictures have been acquired using a Jeol Neoarm operating at 200kV at the Centre Électronique de Microscopie Stéphanois, in Saint-Étienne, with the help of Benoit Mahler from the ILM Lyon. Other experiments were performed on a Nion UltraSTEM 200 operating at 200 kV at the Laboratoire de Physique des Solides of Orsay, with the help of Marta de Frutos.

TEM/STEM observations were otherwise made on a Titan Themis 200 microscope (FEI/ Thermo Fischer Scientific) equipped with a geometric aberration corrector on the probe, at the center of nanosciences and nanotechnologies of Palaiseau, with the help of Gilles Patriarche. The microscope was also equipped with the "Super-X" systems for EDX analysis with a detection angle of 0.9 steradian. The observations were made at 200 kV with a probe current of about 50 pA and a half-angle of convergence of 17 mrad. HAADF-STEM images were acquired with a camera length of 110 mm (inner/outer collection angles were respectively 69 and 200 mrad). The HRTEM images and selected area electron diffraction patterns (SAED) were acquired on a Ceta 16M camera. The camera length for the electron diffraction was 100 cm with a spot size of 5 in order to minimize the irradiation of the sample.

UV-vis absorption was measured on a Lambda 750 Perkin-Elmer and an OceanOptics spectrophotometers.

CD was performed on a Jasco spectrophotometer.

Powder X-Ray Diffraction (XRD) analyses were realized with a PANalytical Empyrean X-ray diffractometer equipped with a 1.8 kW Cu K α ceramic tube, operating at 45 kV and 40 mA and a PIXcel3D 2 x2 area detector.

Rutherford backscattering spectrometry (RBS) was used in order to measure the mean atomic composition [S]/[In]. For this purpose the sample, initially in powder form, was deposited on a carbon adhesive tape. The analysis was performed with 4He⁺ ions of 2 MeV energy delivered by the 4 MV Van de Graaff accelerator of the "ANAFIRE" platform located at the Institut de Physique des 2 Infinis (IP2I) Laboratory of Lyon. The backscattered particles were detected with a 15 keV resolution implanted junction set at an angle of 169° with respect to the beam axis. The experimental data were fitted with the help of the SIMNRA simulation code [124]. RBS analyses were performed with the help of Bruno Canut from the INL.

XPS spectra were recorded on a THERMO K-alpha+ spectrometer with the Al K α line used as the excitation source at the Laboratoire Science et Surface of Ecully (Serma Technologies).

Synchrotron SAXS experiments were performed on the SWING beamline at the SOLEIL synchrotron (Saint-Aubin, France) using an X-ray energy of 16 keV. The sample to detector distance was of 1 m.

3.5.3 Solvothermal synthesis of indium sulfide nanoribbons

0.0511 g of anhydrous indium (III) acetate (0,175 mmol, 1 eq.), 0.0056 g of sulfur powder (0,175 mmol, 1 eq.), 12.25 mL of 1-octylamine and 1.75 mL of absolute ethanol are introduced in a 20-mL Teflon-lined autoclave.

The reaction mixture is ultrasonicated 10 minutes (amplitude 30) to get a homogeneous solution. The autoclave is then sealed and heated at 220°C for 12h in an oven.

Once it is cooled down to room temperature, the yellow-cloudy resulting solution is centrifuged 5 minutes at 6153 x g. The product is redispersed in 5 mL of absolute ethanol before being centrifuged again 5 minutes at 6153 x g. This procedure is reproduced twice in a mixture of 5mL of toluene and 3mL of ethanol, and twice in 5mL of toluene.

The final yellow product is redispersed in 20 mL of toluene. A typical mass concentration in product at the stage is 1.3 g/L.

3.5.4 Unfolding of indium sulfide nanoribbons by ligand exchange

A typical procedure to unfold completely as-synthesized octylamine-capped InS nanoribbons is to add 355 μ L of oleylamine (final concentration in solution of 1,2M) to 150 μ L of the above solution of folded-nanoribbons (final concentration in solution of 0.22 mg/mL) and 395 μ L of toluene in a vial. The mixture is then sonicated during 10 minutes before being heated 21h under agitation (150 rpm) at 95°C in an oil

bath. 500 μ L of absolute ethanol is added and the mixture is centrifuged 5 minutes at 6153 x g : the precipitate of unfolded-InS nanoribbons is then redispersed in 1mL of toluene. This last step can be repeated twice in order to get rid of oleylamine traces.

The same procedure above is then applied, using different amino ligands instead of oleylamine (used for complete unfolding): butylamine (maximal coiling), dodecylamine, tetradecylamine, hexadecylamine, octadecylamine (complete unfolding). The final amino ligand concentration in solution has still to be of 1.2M in solution.

3.5.5 Functionalization of indium sulfide nanoribbons by L- or D-Penicillamine using a phase transfer method

0.0306 g of L- or D-Penicillamine (0.2 mmol) are dissolved by sonication in 150 μ L of distilled water and 0.5 mL of methanol. The pH of the solution is adjusted between 10 and 12 using a 2M sodium hydroxide solution.

1 mL of a solution of InS NR in hexane (approximate concentration of 2.3 mg/mL) is then added to the mixture, which is vigorously stirred for 4 minutes. The upper organic phase initially yellow cloudy becomes transparent and is removed. The lower aqueous phase initially transparent becomes white cloudy.

0.5 mL of distilled water are then added. The aqueous solution is centrifuged and the white product is redispersed in 1.5 mL of distilled water before being characterized by circular dichroism spectroscopy.

CHAPTER 4

Self-assemblies of CdSe nanoplatelets

Chapter abstract

We describe the syntheses of four-monolayer (ML) and five-ML CdSe nanoplatelets (NPL) and their optimization in order to ensure their reproducibility. Once the NPL obtained, we perform their self-assembly upon the addition of oleic acid. Chains of hundreds of nanometers are obtained. 4ML-CdSe NPL assemblies present a twisted conformation with a high degree of distortion of the NPL inside it. We attribute this distortion to strain induced by the ligands to the NPL surface. Furthermore, a correlation between the aspect ratio of the NPL and the twisting of the overall assembly is observed: square 4ML NPL lead to straight assemblies whereas rectangular 4ML NPL lead to twisted assemblies. 5ML-CdSe NPL assemblies can reach several micrometers in length and may be found on a straight form or a twisted form.

In collaboration with Laurent Coolen and Jiawen Liu from the Institut des NanoSciences de Paris (INSP), we investigate the optical properties of 5ML-CdSe assemblies. We evidenced by fluorescence microscopy homo-FRET on self-assemblies of 5ML-CdSe NPL, with an exciton migration over 500 nm (90 NPL). We measured a FRET rate of 1.5 ps^{-1} , which makes this phenomenon much faster than all other decay mechanisms. Strong FRET-mediated collective photophysical effects can thus be expected. Moreover, we calculated a FRET efficiency between neighbouring NPL of 99.99%.

Among the variety of 2D-nanomaterials reported in the literature, CdSe nanoplatelets (NPL) represent a model of study as their synthesis is abundantly described as well as their outstanding optical properties. These properties are described in section 1.1.3. They originate from the strong quantum confinement that occurs along the thickness of the NPL: as this thickness is tunable to the monolayer, so are the absorption and emission properties of the NPL [4]. High fluorescence quantum yield [45, 4, 46], short fluorescent lifetime [4], low lasing threshold [51, 52, 53] or ultrafast resonance energy transfer [8, 46] are examples of interesting properties of cadmium chalcogenide NPL.

Assembling these NPL into larger superstructures broadens the scope of potential applications such nanomaterial might have and may lead to new ensemble optical

properties. Assemblies of 4ML-CdSe NPL [48, 44] and 5ML-CdSe NPL [43] were already realized in our group and an exhaustive discussion about them is led in section 1.4.3. The main aim of the following work was to reproduce CdSe NPL assemblies in order to go further in the investigation of their optical properties. This was led in the framework of a collaboration with Laurent Coolen during Jiawen Liu's PhD from the Institut des NanoSciences de Paris (INSP).

4.1 Syntheses and assemblies of 4ML-CdSe NPL

4.1.1 Synthesis of 4ML-CdSe NPL

The protocol used is described in the experimental section and on the scheme of Figure 4.1. A solution of cadmium myristate with selenium in ODE is heated up to 240°C with a temperature ramp around 30°C.min⁻¹. At 196°C cadmium acetate is injected and triggers the anisotropic growth of the NPL (see section 1.2.3). The temperature is held 10 minutes at 240°C, after what 1 mL of oleic acid is added. The mixture is cooled down to room temperature thanks to a water bath and the crude is purified with several centrifugations and redispersions in a hexane/ethanol 3:1 mixture.

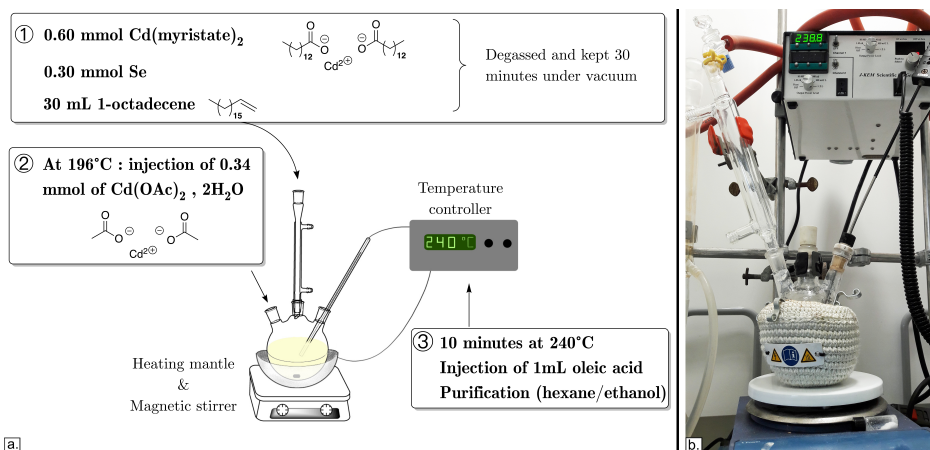


Figure 4.1 – (a.) Scheme of the experimental procedure to synthesize 4ML-CdSe NPL - (b.) Picture of the corresponding experimental setup.

Rectangular NPL are obtained, as showed in Figure 4.2.a. Typical dimensions are measured by TEM and are of (46 ± 1) nm by (10.0 ± 0.5) nm^a. The thickness of 4 monolayers (1.2 nm) is confirmed by UV-visible spectroscopy (Figure 4.2.b.), as the NPL present the two absorption peaks at 481 nm and 512 nm reported for NPL of this precise thickness [4] (see also section 1.1.3).

A first field of investigation was the optimization and the reproducibility of the synthesis to lead to the protocol finally described in the experimental section. Indeed, with the initial protocol followed [44], we first encountered some difficulties to obtain sample containing only 4ML-CdSe NPL, even after several purification steps of the

a. All following uncertainties are calculated as described in last chapters. The global uncertainty given for each dimension is $U = 2 \cdot \sqrt{U_A^2 + U_B^2}$ with $U_A = \frac{\sigma}{\sqrt{n}}$ the A-type uncertainty (σ is the square deviation of the statistical series and n the number of measurements, here 50). B-type uncertainties are given by U_B which is evaluated on the repetition of a same measurement 50 times.

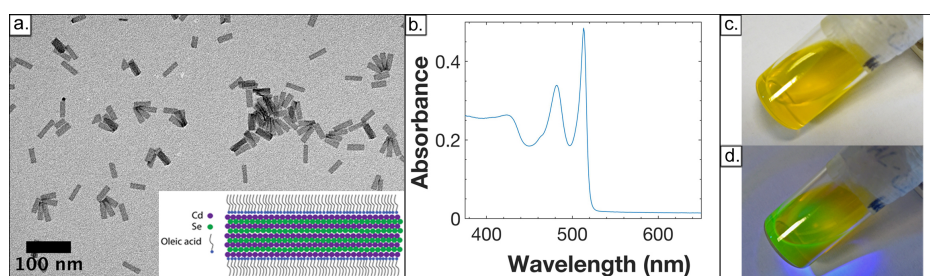


Figure 4.2 – (a.) TEM image of 4ML-CdSe NPL synthesized according to the protocol described in the experimental section. The insert is a schematic representation of the atomic arrangement inside a NPL, highlighting the different ML and the capping ligands (not at scale) - (b.) UV-visible absorption spectra of these 4ML-CdSe NPL with a characteristic feature at 510 nm - (c., d.) Pictures of 4ML-CdSe solution in hexane under visible light (c.) and illumination under UV light, showing the light green fluorescence of the NPL (d.).

crude. This last one was usually made of a lot of spherical quantum dots along some 3ML-CdSe NPL and few 4ML and 5ML-CdSe NPL, as shown by UV-visible spectroscopy.

To overcome this problem, we changed some synthesis parameters, such as the temperature ramp, the reaction time, the amount of cadmium acetate, the purification procedure or the cadmium myristate preparation. First, the purification scheme was adapted: while acetonitrile was firstly used to separate unreacted material and dots from anisotropic material, we observed that a simple centrifugation of the crude after the addition of hexane led to a better result. After that, the purification efficiency of the crude we obtained was improved by performing a succession of centrifugation and redispersion in a hexane/ethanol mixture. The final purification process retained is described in the experimental section.

Secondly, we varied parameters from the synthesis itself. We saw the temperature ramp greatly influences the final composition of the crude: reducing it from 35°C/s to 25°C/s allowed us to obtain less unwanted nanomaterials (that is to say QD and 3ML-CdSe NPL) in the crude.

We varied also the amount of cadmium acetate dihydrated injected during the synthesis. We observed a direct link between the quantity of cadmium acetate injected and the aspect ratio of the NPL.

Table 4.1 – CADMIUM ACETATE: Average lateral dimensions of 4ML-CdSe NPL synthesized with a varied amount of cadmium acetate injected, expressed in equivalents (eq) of Cd(myristate)₂.

Cd(OAc) ₂ injected	1 eq	0.6 eq	0.56 eq
Aspect ratio	1.0	3.3	4.6
Length (nm)	27 ± 1	25.2 ± 0.9	46 ± 1
Width (nm)	27 ± 1	7.6 ± 0.6	10.0 ± 0.5

When 1 equivalent of cadmium acetate is injected as regards the equivalent of cadmium myristate, square 4ML-CdSe NPL are obtained with sides of (27 ± 1) nm (Figure 4.3.a.). Decreasing the quantity of cadmium acetate injected leads to an increase of the aspect ratio of the NPL (Figures 4.3.b. and 4.2.a.). This trend is reflected in Table 4.1. As discussed in section 1.2.3, the coordination of cadmium acetate on preferential facets of the growing nanocrystal may lower the energy and the growth rate of such facets compared to others and thus induces the anisotropic growth. As the quantity of cadmium acetate is increased, we hypothesize that its

bonding is not as facet-selective than in the case with few equivalents injected, and that more facets are in the end coordinated with cadmium acetate. This would result in a loss of anisotropy in the growth process and thus a square shape instead of a rectangular shape at the end.

Moreover, decreasing the amount of cadmium acetate seems to limit the amount of undesirable 5ML-CdSe NPL.

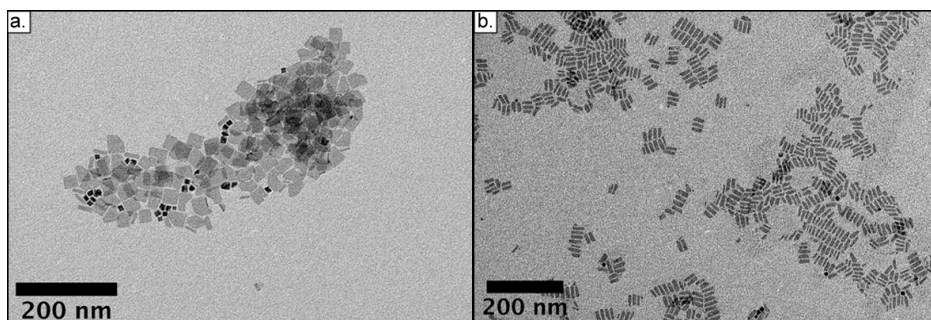


Figure 4.3 – TEM images of 4ML-CdSe NPL synthesized with the injection of: (a.) 1 equivalent or (b.) 0.6 equivalent of cadmium acetate as regards the equivalent of cadmium myristate. The former case gives rise to square NPL, the latter to rectangular NPL.

Finally, we focused on the preparation of the cadmium precursor. Cadmium myristate was initially synthesized from myristic acid which was deprotonated with sodium hydroxide, before being reacted with cadmium nitrate. As-synthesized cadmium myristate yielded poor-quality crudes with high proportion of unwanted materials (i.e. dots, 3ML and 5ML-CdSe NPL). We suggest that the presence of water in the precursor, mainly from the deprotonation step, was responsible for the bad quality of the crudes. This hypothesis was reinforced as we replaced myristic acid by commercial sodium myristate, avoiding the deprotonation step, and dried the product of the reaction between sodium myristate and cadmium nitrate overnight on a freezer-dryer. These additional procedures led to reaction crudes with fewer unwanted materials and to a better reproducibility of our syntheses.

4.1.2 Self-assembly of 4ML-CdSe NPL

Once 4ML-CdSe NPL were synthesized, we undertook their self-assembly according to the protocol described in the experimental section and previously used in our group [44]. To a solution of 4ML-CdSe NPL in hexane, a fixed amount of oleic acid is added. The solution is let to evaporate a few days before being redispersed in hexane and dropcasted on a TEM grid.

Figure 4.4 shows TEM images of the assemblies. We obtained twisted assemblies of individually strongly distorted 4ML-CdSe NPL. Intriguing distorted structures such as horseshoe (Figure 4.4.d.) or bow-tie shapes (Figure 4.4.e.) were noticed in TEM images. Figures 4.5.c. and 4.5.d. show high-resolution STEM images of distorted NPL inside an assembly.

For NPL with an aspect ratio of 2.5 (Figure 4.4.a. and b.), twisted assemblies of (565 ± 49) nm were observed with an average pitch of (197 ± 7) nm. Long assemblies were pointed out, for a maximal length measured of $1.381 \mu\text{m}$.

To obtain these assemblies, 4ML-CdSe NPL were dispersed in a 0.02M oleic acid solution in hexane and let to evaporate at the rate of 0.21 mL per hour. We then

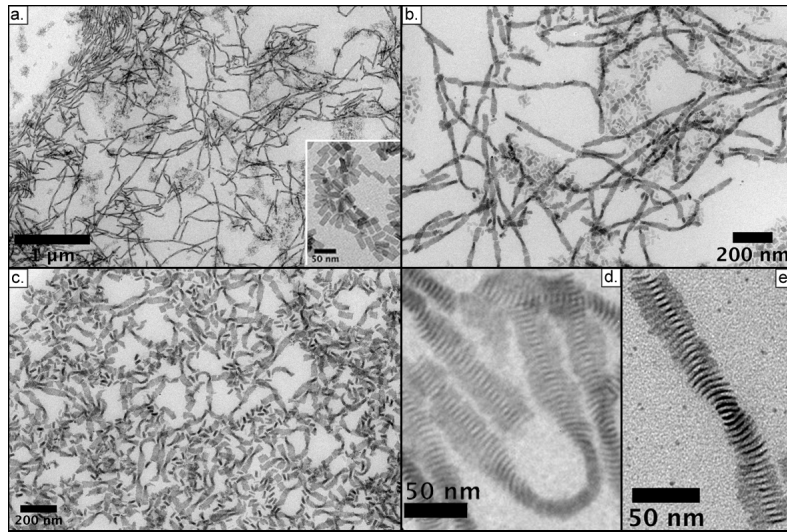


Figure 4.4 – TEM IMAGES OF 4ML-CdSe NPL ASSEMBLIES. (a., b.) Assemblies obtained after evaporation of a hexane solution of 4ML-CdSe NPL containing 0.02M of oleic acid. The assemblies get an average length of (565 ± 49) nm and could reach the micrometer. The insert is a TEM image of the 4ML-CdSe NPL used for the assembly, that get lateral dimensions of (31.8 ± 0.6) nm \times (12.9 ± 0.5) nm, that is to say an aspect ratio of 2.5. - (c.) Assemblies of 4ML-CdSe NPL obtained without any evaporation of the system, of an average length of (258 ± 22) nm. This length is similar to the one obtained with a same sample subjected to evaporation ((222 ± 19) nm). The NPL get an aspect ratio of 3.4 as they are (37 ± 1) nm long and (10.9 ± 0.6) nm wide. - (d., e.) Magnification on 4ML-CdSe assemblies, showing the strong distortion occurring inside assemblies, leading to a horseshoe (d.) or a bow-tie (e.) shape.

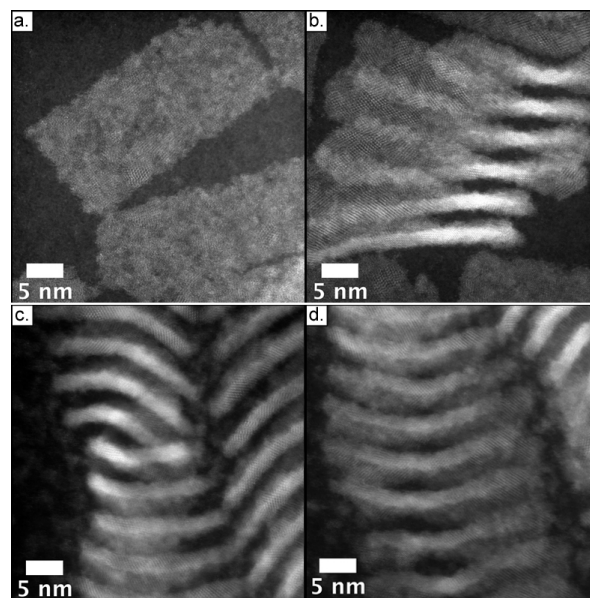


Figure 4.5 – (a., b.) HAADF-STEM images of 4ML-CdSe NPL before any assembly process. Some NPL are already strongly twisted in the sample - (c., d.) HAADF-STEM images of distorted 4ML-CdSe NPL within an assembly. These images were acquired with the help of Marta de Frutos from the Laboratoire de Physique des Solides in Orsay.

varied experimental parameters in order to control the length and potentially the shape of the assemblies.

We first wondered on the role of the evaporation in the auto-assembly process and compared the assemblies from two samples with and without evaporation. Both were made from the same batch of 4ML-CdSe NPL that get an aspect ratio of 3.4 in a 0.26M oleic acid solution in hexane. One was let to evaporate at a rate of 0.15 mL.h^{-1} and then redispersed in hexane, while the other was sealed and kept closed. Surprisingly, their deposit on TEM grids showed in both cases 4ML-CdSe NPL assemblies of a similar length: (222 ± 19) with evaporation, (258 ± 22) nm without evaporation.

We concluded that auto-assembly can occur without evaporation. Nevertheless, we are reserved on the fact that evaporation hasn't any impact on the length of the assembly: actually, to redisperse the evaporated solution, a short sonication is necessary and even few seconds in a sonic bath might break assemblies and therefore shorten their average length. Further investigations are underway to better understand the effect of the TEM grid preparation method and sonication on the NPL assembly.

We also varied the quantity of oleic acid (OA) added. We observed an increase in the assembly length as oleic acid concentration was increased (Table 4.2). This is consistent with previous works reported in the literature [44, 152] and with the potential origin of self-assembly process in depletion forces caused by OA molecules. Depletion and attraction between NPL are enhanced with the oleic acid concentration.

Table 4.2 – OLEIC ACID CONCENTRATION: Average length of 4ML-CdSe NPL assemblies for different oleic acid concentrations.

Oleic acid concentration (mol/L)	Average length
0	No assembly
0.056	(122 ± 10) nm
0.16	(166 ± 10) nm
0.26	(258 ± 22) nm

The aspect ratio of 4ML-CdSe NPL is of 3.4, no evaporation are carried out.

Other parameters such as the solvent of redispersion (toluene, cyclohexane) the evaporation rate or the purification procedure of NPL were tested but did not impact importantly the self-assembly process.

The shape difference between former straight assembly from our group [44] and twisted assembly reported here may originate from the different aspect ratios of the NPL. Square NPL would lead to straight assemblies whereas rectangular one would lead to twisted assemblies. In the latter case, the individual distortion of rectangular NPL due to ligand adsorption and ordering at their surface might be greater than for square NPL and thus propagate within the whole assembly as a consequence of NPL-NPL interaction and energy optimizations.

Kim et al. reported in a recent paper [152] 4ML-CdSe NPL assemblies with similar forms and patterns as the ones presented here. The pitch length of the assemblies was measured and founded as dependent of the lateral dimensions of the NPL. No pitch are obtained with square NPL assemblies, strengthening our hypothesis above.

4.2 Syntheses and assemblies of 5ML-CdSe NPL

4.2.1 Synthesis of 5ML-CdSe NPL

The synthesis of 5ML-CdSe NPL was realized according to a protocol established in the lab [43]. The procedure is detailed on the experimental section and illustrated on Figure 4.6. The synthesis is similar to the one of 4ML-CdSe NPL previously described. The precursor source is changed for cadmium oleate. The amount of cadmium acetate is increased and its injection has to be done at higher temperature (205°C).

No optimization of the reaction was necessary to be done except for the preparation of cadmium oleate, which for the same reason of cadmium myristate has to be dried one night on a freezer-dryer.

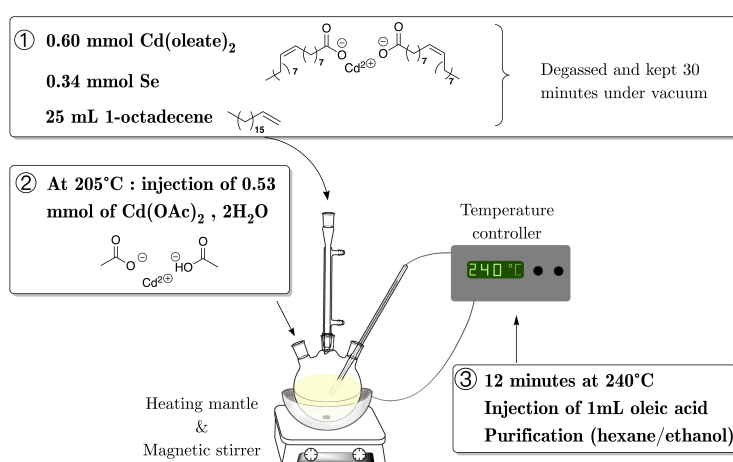


Figure 4.6 – Scheme of the experimental procedure to synthesize 5ML-CdSe NPL.

Figure 4.7.a. shows 5ML-CdSe NPL obtained from this procedure. These NPL are of (19.7 ± 0.9) nm in length for (8.1 ± 0.5) nm in width. Their UV-visible spectrum is typical for NPL of a five-monolayer thickness (1.5 nm, 6 layers of Cd and 5 layers of Se), with a narrow peak of absorption at 550 nm (Figure 4.7.b.). A bright green fluorescence is observed under UV-illumination. The emission spectrum of the NPL is centered at 549 nm for an excitation at 470 nm (Figure 4.7.b.). A Stokes shift of only 2 nm is measured.

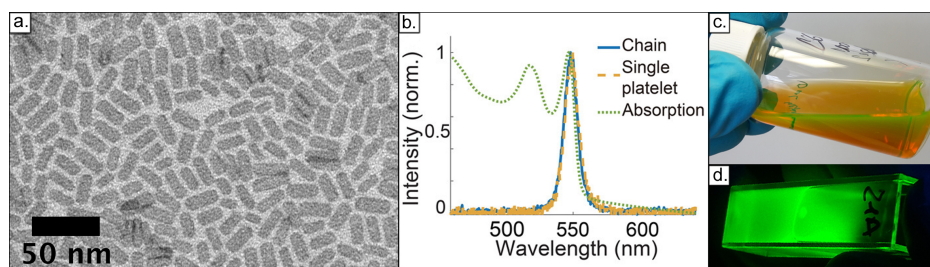


Figure 4.7 – (a.) TEM image of 5ML-CdSe NPL synthesized according to the protocol described in the experimental section. - (b.) UV-visible absorption spectra of these 5ML-CdSe NPL with a characteristic feature at 550 nm - (c., d.) Pictures of 5ML-CdSe solution in hexane under visible light (c.) and illumination under UV (d.), showing the green fluorescence of the NPL.

4.2.2 Self-assembly of 5ML-CdSe NPL

5ML-CdSe NPL are assembled in a similar manner than 4ML-CdSe NPL according to a procedure described in the experimental part and in previous works from our group [43]. After purification of the NPL, the assembly takes place upon the addition of oleic acid (OA) to a dispersion of NPL.

1D chains of NPL are obtained with typical lengths from 1 to 2 μm (Figure 4.8). NPL are facing face-to-face inside these assemblies with a center-to-center distance evaluated in TEM of $\delta = (5.4 \pm 0.1) \text{ nm}$ ^b.

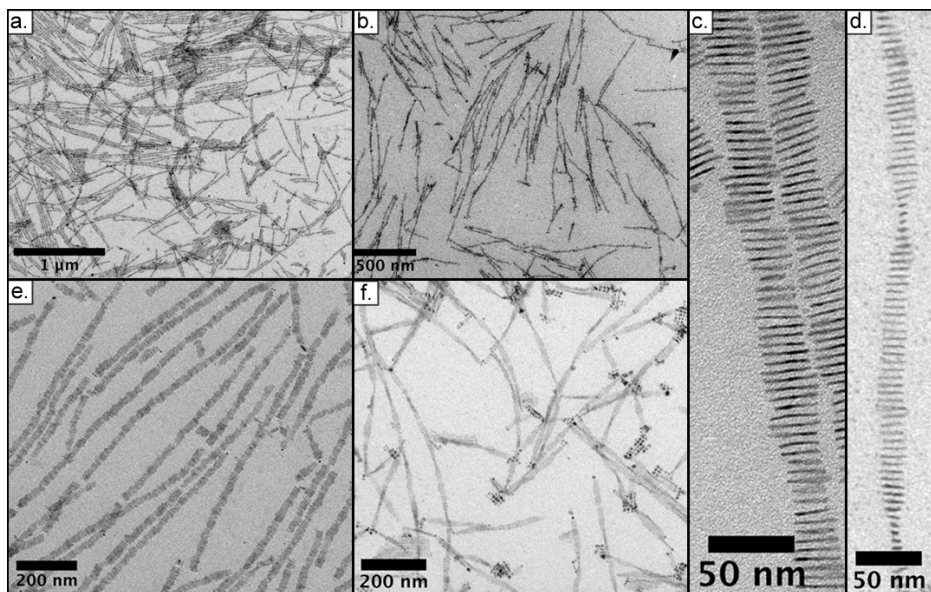


Figure 4.8 – TEM IMAGES OF 5ML-CdSe NPL ASSEMBLIES AT DIFFERENT MAGNIFICATIONS. (a., b.) Assemblies obtained after evaporation of a same NPL dispersion in an oleic acid solution in hexane of (a.) 0.036 M and (b.) 0.8 M - (e., f.) Two kinds of assemblies respectively (e.) straight (obtained after evaporation, [OA] = 0.018M) and twisted (no evaporation, [OA] = 0.025 M). Details of these straight or twisted assemblies are given respectively in inserts (c.) and (d.).

By varying experimental parameters, the same remarks as the one formulated for 4ML-CdSe assemblies can be made.

Firstly, we let the sample either under evaporation or in a closed vial. In both cases, NPL assemblies of similar length were obtained: $(529 \pm 80) \text{ nm}$ with evaporation and $(495 \pm 69) \text{ nm}$ without evaporation. The same conclusions as for 4ML-CdSe assemblies can be drawn.

We varied in a second time the quantity of oleic acid in the NPL dispersion (Figures 4.8.a. and 4.8.b.). Results are summed up in Table 4.3. The trend already pointed out on literature and in our group [43] is reflected here: the more the OA concentration, the longer the assemblies.

Finally, we observed two distinctive morphologies of assemblies: a first one where the overall thread is straight (Figure 4.8.c. and e.) and another where the thread is twisted and adopts an helicoidal structure (Figures 4.8.d. and 4.8.f.). In both cases, NPL inside these assemblies are distorted but in a lesser extent than 4ML-CdSe assembled NPL. At this stage of our work, we do not fully understand how to selectively

^b. This value is in agreement with previous small-angle X-ray scattering measurement of 5.84 nm on a similar sample [43].

obtain one kind of assembly rather than the other.

Table 4.3 – OLEIC ACID CONCENTRATION: Average length of 5ML-CdSe NPL assemblies for different oleic acid concentrations.

Oleic acid concentration (mol/L)	Average length
0	No assembly
0.036	(495 ± 69) nm
0.36	(549 ± 50) nm
0.80	(676 ± 80) nm

The length of the 5ML-CdSe NPL is of (18.4 ± 0.9) nm and their width of (6.1 ± 0.7) nm. So, the aspect ratio of 5ML-CdSe NPL is of 3. Assemblies were obtained without evaporation of the NPL solution.

We think the oleic acid coverage at the surface of each NPL might play a significant role, but we do not succeed to establish unambiguously a correlation between the OA concentration in the NPL dispersion and thread twisting yet. Indeed, and as discussed in section 1.4.3, OA may induce surface stress at the surface of NPL and be responsible for their individually twisted conformation. If this twisting is important, it might propagate throughout the whole thread length as a consequence of improved NPL-NPL interactions and energy stabilization of the structure.

Twisted assemblies upon gradual addition of OA and continuous evaporation was previously obtained in our group [43]. As we also obtained twisted assemblies in closed vials, the evaporation process does not seem the only pertinent parameter for the thread twisting. The quantity of OA might have to be taken also into account.

Finally, as the aspect ratio of the 5ML-CdSe NPL is always kept similar in all our experiments, it neither seems to be a critical parameter in thread twisting. Nevertheless, all other parameters fixed, it would be interesting to vary it and see its influence on NPL self-assembly. Further investigations are obviously needed to be performed to control experimentally the twisting of assemblies and to understand its physical origin.

4.2.3 Optical properties of nanoplatelets assemblies

As CdSe NPL present a very small Stokes shift and parallel in-plane dipoles when they are stacked face to face, their assemblies fulfill the criteria for Förster Resonant Energy Transfer (FRET) to occur (see also section 1.4.4).

FRET is reported in various system, such as fluorescent molecules or QD, but exciton migration by FRET hopping is generally limited to few tens of nanometers [153, 154] and few emitters.

In collaboration with Laurent Coolen from the Institut des Nanosciences de Paris (INSP) during Jiawen Liu’s PhD, we evidenced homo-FRET inside NPL assemblies with ultralong exciton migration over 500 nm and so FRET hopping over 90 NPL. FRET migration distance, rate and efficiency were evaluated from microphotoluminescence observations (Figure 4.9). Full experimental details are given in the paper in reference [155], and we will sum up in the following lines the main results. Syntheses and assemblies of 5ML-CdSe NPL were performed in our lab, whereas optical measurements, modelling and interpretations were realized by Laurent Coolen and Jiawen Liu at the INSP.

About Förster Resonant Energy Transfer (FRET)

FRET is a non-radiative energy transfer mechanism between two species, one donor and one acceptor, by electromagnetic dipole-dipole coupling. The principle of FRET is exposed in Figure 1.23 on page 31. If this phenomenon may be detrimental in optoelectronics as it can funnel excitonic energy to quenching site within the material and so decrease its quantum yield, it can also favour efficient charge collection in photovoltaic cells and lead to new FRET-enabled excitonic devices [156].

FRET efficiency η of a donor-acceptor system is defined as

$$\eta = \frac{\gamma_{tr}}{\gamma_o + \gamma_{tr}} \quad (4.1)$$

with γ_{tr} the rate of the FRET process and γ_o the exciton decay rate within the donor (e.g. a single isolated NPL) [46]. This exciton decay rate within a NPL can be expressed as the sum of the radiative γ_{rad} and non-radiative decay rates γ_{nr} , that is to say

$$\gamma_o = \gamma_{rad} + \gamma_{nr} \quad (4.2)$$

It characterizes the intrinsic relaxation of the donor. When considering the donor-acceptor system S (e.g. two NPL stacked face-to-face), we have to take additionally into account an energy transfer decay rate mainly from FRET phenomenon ^a, so as the exciton decay rate within the system γ_S is

$$\gamma_S = \gamma_o + \gamma_{tr} \quad (4.3)$$

FRET efficiency can then be rewritten as $\eta = 1 - \frac{\gamma_o}{\gamma_S}$. By definition of the fluorescent lifetimes of the donor ($\tau_o = \frac{1}{\gamma_o}$) and of the system S ($\tau_S = \frac{1}{\gamma_S}$), it comes:

$$\eta = 1 - \frac{\tau_S}{\tau_o} \quad (4.4)$$

The fluorescence lifetimes are experimentally accessible as the fluorescence intensity I evolves as $I(t) = I_o \cdot e^{-\frac{t}{\tau}}$ with I_o the initial fluorescence at $t=0$ and τ the fluorescence lifetimes of the system investigated (respectively τ_o for a single donor or τ_S for the donor-acceptor association).

Finally, let us note that in the case of NPL [156], the FRET rate γ_{tr} is proportional to $(\frac{R_o}{\delta})^4 \cdot \frac{1}{\tau_o}$ with R_o the Förster radius and δ the center-to-center distance between NPL ^b. R_o represents the distance between donor and acceptor at which the energy transfer efficiency is 50%. It is dependent on the spectral overlap between donor and acceptor and of their relative dipole orientations. As NPL get perfect spectral overlap and parallel dipole orientation between their assembly, long Förster radius are estimated to 13.5 nm and make this material an ideal candidate for ultrafast FRET [156].

^a. We consider for clarity reason that only FRET is responsible for energy transfer within the system: other energy transfer mechanisms as Dexter energy transfer are neglected here (see next paragraph for justification), otherwise their contribution would also be needed to be taken into account.

^b. This dependence varies with the geometry of the donor and the acceptor: for point-like dipole pairs, γ_{tr} is function of $(\frac{R_o}{d})^6$, with d the distance between dipoles.

A solution of the self-assembled NPL obtained as described in the previous section (twisted assemblies with lengths up to two micrometers long) was diluted 500 times and spin-coated on a glass slide at 4000 rpm for 40 s. The sample was then covered by a 30-nm layer of PMMA for microphotoluminescence observations. First, the emission spectrum of NPL inside the assembly is the same as for individual isolated NPL (Figure 4.7). Negligible dispersion is observed in the fluorescence spectrum of NPL that emit at 549 nm, showing the excellent homogeneity of the sample and excluding any strong hetero-FRET effect. The reason for this negligible inhomogeneity is that the exciton energy depends only on the confinement which occurs along the thickness of the NPL and that this thickness is controlled finely and accurately during the synthesis process with an atomic precision.

Figure 4.9.a. shows the fluorescence image from three different chains under wide-field excitation. In agreement with TEM observations, chains with a length between one to two micrometers were imaged. The excitation source was then changed for a pulsed laser positioned at the center of the chain. The radius of the spot was of 160 nm, so that if no transfer occur, only this region would have been luminescent. This was not the case as, for all chains considered, fluorescence was observed far beyond the spot of the excitation laser (Figure 4.9.b.). The intensity profile along the chain axis x can be fitted by a Gaussian of half-width l_x which range between 470 nm and 720 nm: l_x represents the maximal distance from the center of the laser spot at which we see fluorescence in the chain.

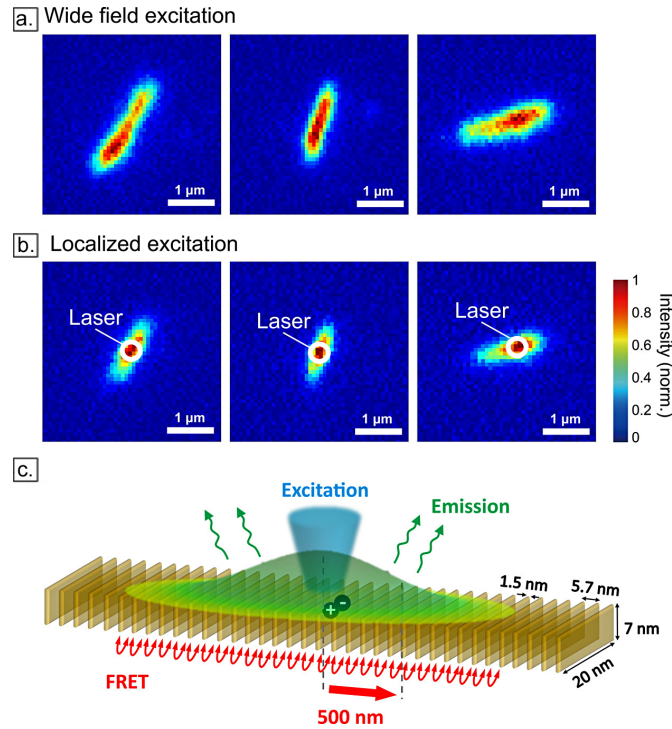


Figure 4.9 – FLUORESCENCE MICROSCOPY: Images of three platelets chains (a.) under wide field excitation and (b.) excited locally by a laser spot - (c.) Schematic of the proposed FRET migration mechanism. These optical measurements were realized by Jiawen Liu and Laurent Coolen from the INSP.

In order to estimate the exciton migration length value l_{FRET} , a correction in resolution has to be applied on l_x , taking into account the setup's response function. This response function represents the fact that, even in absence of any energy migra-

tion process, the Gaussian intensity profile along the chain axis of the assembly has a width caused by the microscopy protocol. As a function of the laser spot and the imaging point spread function^c, this half-width can be evaluated as $l_{RF} = 246$ nm. The fact that l_x is larger than l_{RF} unambiguously proved there is energy migration along the thread. We could then obtain the migration length inside the assembly:

$$l_{FRET} = \sqrt{l_x^2 - l_{RF}^2} \quad (4.5)$$

We found an average migration length l_{FRET} of 500 nm with a dispersion of 150 nm which could be caused by experimental uncertainties as well as differences between chains such as degree of disorder or twisting. By dividing l_{FRET} by the center-to-center NPL distance δ , we deduced there is inside NPL assemblies an exciton energy diffusion over 90 NPL (Figure 4.9.c.). It is shown in reference [155] homo-FRET is almost entirely responsible for this energy transfer, as waveguiding effects are negligible in light propagation along the chain according to our simulations as well as Dexter mechanism which decays exponentially with distance over a typical 1 nm scale. Multiexcitonic contribution and non-linear effect are also excluded.

Finally, to determine the FRET rate γ_{tr} and the FRET efficiency, Laurent Coolen and Jiawen Liu proposed a diffusion model based on the following assertions. Let us note n_i the probability of the i^{th} inside the chain to be excited after the creation of an exciton at $t=0$. The variation over time of this probability can be expressed in terms of energy transfers (ET) that the i^{th} NPL get with the $(i+1)^{th}$ and $(i-1)^{th}$ neighbouring NPL and in terms of its desexcitation:

$$\frac{dn_i}{dt} = \underbrace{\gamma_{tr} \cdot (n_{i+1} + n_{i-1})}_{\text{ET from } (i+1)^{th} \& (i-1)^{th} \text{ NPL}} - \underbrace{2\gamma_{tr} \cdot n_i}_{\text{ET to } (i+1)^{th} \& (i-1)^{th} \text{ NPL}} - \underbrace{\gamma_o \cdot n_i}_{\text{desexcitation of } i^{th} \text{ NPL}} \quad (4.6)$$

$$\Leftrightarrow \frac{dn_i}{dt} = -(\gamma_o + 2\gamma_{tr})n_i + \gamma_{tr}(n_{i-1} + n_{i+1}) \quad (4.7)$$

If we consider length scale much larger than δ , we can express from equation 4.7 the exciton probability density $n(x, t)$ as the solution of the following diffusion equation:

$$\left(\frac{\partial n}{\partial t}\right)(x, t) = -\gamma_o \cdot n(x, t) + D \left(\frac{\partial^2 n}{\partial x^2}\right)(x, t) \quad (4.8)$$

where $D = \delta^2 \gamma_{tr}$ is the diffusion coefficient. As the fluorescence intensity is a function of $n(x, t)$ and by resolving the preceding equation 4.8, we can express the fluorescence intensity of the overall chain (see [155] for mathematical details):

$$I(t) = \gamma_{rad} \cdot e^{-\gamma_o \cdot t} \quad (4.9)$$

We can then deduce that in the framework of our model the luminescence decay curve of the whole chain evolves in a similar way to the single NPL decay: both evolves as $e^{-\gamma_o \cdot t}$. In other terms, homo-FRET redistributes excitons within the thread but

^c The point spread function (PSF) is a mathematical function that describes the response of an imaging system to a point source. A manifestation of the PSF of an optical system lies on the blurring observed around the image of a point object.

does not impact their number neither the overall energy loss inside the chain which is just function of γ_o .

A consequence is that homo-FRET rate cannot be extracted directly from experimental decay curves as suggested previously by equation 4.4 and as it was made for hetero-FRET [8, 46]^d. Indeed, migration by hetero-FRET involves only one exciton jump so that the FRET rate can be directly extracted from hetero-FRET decay curves. This is not the case of homo-FRET where the exciton is delocalized on a very large distance l_{FRET} : the luminescent decay is then accelerated by additional non-radiative desexcitations from defect NPL inside the chain that act as collective exciton quenchers [99] (Figure 4.10). This explains why previous works on the decay of same-thickness NPL assemblies reported only a theoretical estimate of the homo-FRET rate but no experimental value [99, 152].

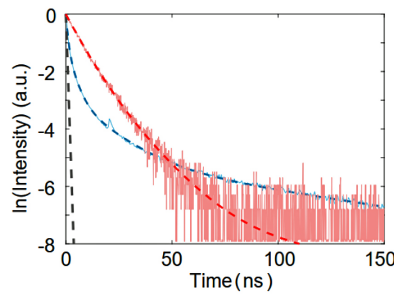


Figure 4.10 – Decay curves of single platelets (red) and stacked NPLs (blue). The grey dashed line indicates the instrument response function. These optical measurements were realized by Jiawen Liu and Laurent Coolen.

By expressing the intensity profile along the chain axis, we are able to link the FRET length to the diffusion coefficient as:

$$l_{FRET} = \sqrt{\frac{D}{\gamma_o}} \quad (4.10)$$

This quantity can be interpreted in diffusion terms: the excitation can migrate during a typical time $\frac{1}{\gamma_o}$ before it decays, so that l_{FRET} is the diffusion length with diffusion coefficient D during a time $\frac{1}{\gamma_o}$.

Thanks to this model and observations (i.e. the experimental values of $l_{FRET}=500$ nm and of $\gamma_o=12$ ns extracted from NPL decay curve in Figure 4.10), we are able to estimate the FRET rate as $\gamma_{tr} = 1.5 \text{ ps}^{-1}$. The associated FRET time of 0.66 ps is much faster than for any other excitonic mechanisms so that FRET is expected to create very strong modifications on the optical behaviour of stacked NPL. FRET time is also shorter than the one reported for QD films, varying from 30 ps to the ns [157, 158].

The diffusion coefficient along the chain is also estimated to $D = 0.2 \text{ cm}^2.\text{s}^{-1}$. It is much higher than the one reported for organic semiconductors or QD films [157, 159] (around $10^{-2}\text{cm}^2.\text{s}^{-1}$). Knowing all these parameters, the FRET efficiency can be calculated following equation 4.4 and a value of $\eta=99.99\%$ is found, in agreement with a very efficient transfer over almost one hundred NPL. This also suggests that diffusion experiences very little damping by quenchers or stacking faults.

^d. Nevertheless, different hetero-FRET rates between stacked NPL of different thicknesses (4ML and 5ML-CdSe NPL) were reported with this method, from 10 ps to 1 ns, and are interpreted as the result of insufficient control in the stacking order [8, 46, 156].

4.3 Outlooks

We have performed the synthesis and self-assembly of 4ML and 5ML-CdSe NPL. By varying the experimental parameters and mainly the concentration of oleic acid in solution, we succeeded in tuning the length of the assemblies.

Twisted assemblies of rectangular 4ML-CdSe NPL were characterized by TEM, highlighting a strong distortion of NPL within it. We think this distortion is the result of ligand strains induced at the surface of the NPL. Such a distortion seems a function of the aspect ratio of the NPL, as we do not observed twisted assemblies when square NPL are assembled [44]. Very recent works of other groups tends to confirm this observation [152].

As regards 5ML-CdSe NPL, two kinds of assemblies are observed: straight assemblies where NPL are perfectly stacked one upon each other, and twisted assemblies where a rotation angle is observed between each stacked NPL. Further work is needed to understand the origin of this twisting and its accurate experimental control.

In collaboration with Laurent Coolen from the INSP during Jiawen Liu's PhD, we evidenced homo-FRET on 5ML-CdSe NPL assemblies and we quantified it by the use of fluorescence microscopy. We found that exciton migration occurs over 500 nm along the thread, that is to say over 90 NPL, with a very low FRET time and an outstanding FRET efficiency of 99.99%. These results make 5ML-CdSe NPL promising devices for future optoelectronics applications.

The investigation on this topic has to be carried on, in order to evaluate the influence of the NPL thickness on the FRET process (e.g. by measuring FRET rate inside 4ML-CdSe NPL assemblies), as well as its dependence from structural features of the assembly (e.g. its twisting or not, or the center-to-center distance between NPL which can be tuned by replacing oleate ligands by shorter ligands such as myristate). We expect these results to pave way to new optoelectronics applications and devices.

4.4 Materials and experimental methods

4.4.1 Starting Materials

1-octadecene (90%) was purchased from Acros Organics. Selenium powder (99,5%), sodium oleate (82%), sodium myristate $\geq 99\%$, cadmium nitrate tetrahydrate (98%), cadmium acetate dihydrate, oleic acid (90%) were purchased from Sigma-Aldrich. Hexane (95%) was purchased from Fisher scientific.

4.4.2 Instrumentation

TEM images were acquired on a JEOL JEM-1400 (accelerating voltage of 120kV) at CIQLE Lyon. The sample are prepared by drop casting suspensions in hexane onto 200 carbon-coated copper grids.

The atomic structure was analyzed by STEM on a Nion UltraSTEM 200 operating at 200 kV and an HAADF detector with an inner collection angle of 70 mrad. The microscope was equipped with a spherical aberration corrector. HAADF-STEM images were realized with the help of Marta de Frutos from the Laboratoire de Physique des Solides in Orsay.

UV-vis absorption was measured on a Lambda 750 Perkin-Elmer spectrophotometer.

Fluorescence spectroscopy and fluorescence microscopy were realized by Laurent Coolen and Jiawen Liu from the Institut des Nanosciences de Paris. The emission spectra of single platelets were recorded by a monochromator (Triax 190 @Horiba) under pulsed laser excitation at 2.5-MHz repetition rate with input power of 10-nW and acquisition duration 20 s. For microphotoluminescence imaging, the experiments were performed on a homemade inverted fluorescence microscope equipped with laser scanning system. The excitation source could be either a mercury lamp (for wide field detection) or a 470 nm diode laser (PDL 800-D PicoQuant, 70-ps pulses, 2.5-MHz rate). The same objective (Olympus apochromat 100X 1.4N.A.) was used to focus the excitation beam on the sample and collect the emission. The scattered excitation light was filtered by a set of filters. The image was focused onto a charge-coupled device (QImaging Retiga EXi, pixel size 6.45 μm). The imaging magnification was 90 so that each pixel on the camera corresponded to 72 nm on the sample. For more details, see reference [155].

4.4.3 Synthesis of cadmium myristate

5.007 g of sodium myristate ($\geq 99\%$, 20 mmol, 250.35g/mol) are dissolved in 400 mL of methanol in a 1 L three-neck round bottom flask equipped with a septum, a cap and a dropping funnel. Sonication and a 40 minutes stirring could be necessary to get a clear solution.

In parallel 3,0847 g of cadmium nitrate tetrahydrate (98.5%, 10 mmol, 308.48 g/mol) is dissolved in 50 mL methanol.

This solution is then added slowly to the reaction mixture (30 minutes of drip-feeding). 350 mL of methanol can be added to allow a good stirring of the mixture which becomes very viscous in the course of the dripping. The reaction medium is afterward stirred for 2 hours at room temperature.

The resulting white product is filtered on sintered-glass (porosity 4), before being washed 3 times by methanol and drying 10 minutes.

Finally, the white resulting product is put on a freezer-dryer for one night, before being stored under vacuum for further uses.

4.4.4 Synthesis of cadmium oleate

12,1776 g (40 mmol, 304.44 g/mol) of sodium oleate (82%) is dissolved in 200 mL of 96% ethanol and 5 mL of water at 70°C, under stirring at 800 rpm and under argon on a 1 L three-neck round bottom flask equipped with a septum, a cap and a dropping funnel.

A mixture of cadmium nitrate tetrahydrate (6.1696 g, 20 mmol, 308.48 g/mol) in 50 mL of 96% ethanol is then added dropwise to the solution of sodium oleate in approximately 45 minutes.

The reaction medium turns white and is kept 2 hours under vigorous agitation at 70°C.

The resulting product is centrifuged 10 minutes at 6000 rpm and then washed four times with hot ethanol by centrifugation (5 minutes at 6000 rpm) and once with hot methanol (centrifugation 3 minutes at 6000 rpm).

Finally, the beige resulting product is put on a freezer-dryer for one night, before being stored under vacuum for further uses.

4.4.5 Synthesis of 4ML-CdSe NPL

Synthesis :

0.340 g of cadmium myristate (0.60 mmol, 567.15 g/mol) is introduced with 0.024 g of selenium powder (0.30 mmol, 78.971 g/mol) and 30 mL of 1-octadecene (ODE) in a 50 mL-three-neck round bottom flask equipped with a septum, a temperature controller and a air condenser. The reaction mixture is degassed and kept under vacuum for at least 120 minutes.

Afterward the flask is purged with argon and the temperature set to 240°C thanks to a 50 mL-flask heating mantle (setpoint at 250°C until 230°C are reached).

At 180°C the selenium begins to dissolve and the solution turns to clear yellow. When the temperature reaches 196°C (generally in 5'20), the septum is withdrawn and 0.090 g (0.34 mmol, 266.52 g/mol) of cadmium acetate dihydrate is swiftly injected into the flask.

The solution turns dark red and could present a green fluorescence under an UV-light. After the temperature reaches 240°C (generally in more or less 7 minutes), the reaction is continued for 10 minutes.

1 mL of oleic acid (3.17 mmol, 282.47 g/mol, density of 0.895) is finally injected and the flask is immediately cooled down to room temperature using a water bath.

Purification :

The crude is transferred in two falcons of 50 mL, where 15 mL of hexane is added in each before being centrifuged 10 minutes at 6000 rpm. The precipitate is then purified by several redispersion in hexane and centrifugations, before being washed once by adding ethanol (7,5 mL per falcon), centrifuged and redissolved in hexane (20 mL in total). The process is controlled under UV-vis absorption spectroscopy, and

additional washing with hexane could be undertaken if necessary to get rid of dots or 3ML-CdSe NPL.

4.4.6 Synthesis of 5ML-CdSe NPL

Synthesis : 0.404 g of cadmium oleate (0.60 mmol, 675.334 g/mol) is introduced with 0.027 g of selenium powder (0.34 mmol, 78.971 g/mol) and 25 mL of 1-octadecene (ODE) in a 50 mL-three-neck round bottom flask equipped with a septum, a temperature controller and a air condenser. The reaction mixture is degassed and kept under vacuum for at least 30 minutes (2h preferred).

Afterward the flask is purged with argon and the temperature set to 250°C with a 100 mL-flask heating mantle. It is important that the rise in temperature occurs quickly, for example in 6 or 7 minutes to heat up the reaction mixture from room temperature to 240°C.

At 180°C the selenium begins to dissolve and the solution turns to clear yellow. When the temperature reaches 205°C, the septum is withdrawn and 0.140 g (0.53 mmol, 266.52 g/mol) of cadmium acetate dihydrate is swiftly injected into the flask.

At 230°C the temperature controller is set to 240°C. The solution turns dark red. After the temperature reaches 240°C, the reaction is continued for 12 minutes. 1 mL of oleic acid (3.17 mmol, 282.47 g/mol, density of 0.895) is finally injected and the flask is immediately cooled down to room temperature using a water bath.

Purification :

The crude is transferred in two falcons of 50 mL and 10 mL of hexane is added in each falcon (if the crude presents too many dots in the UV-visible absorption spectrum, it is possible to replace hexane above by acetonitrile). The solution is centrifuged 10 minutes at 6000 rpm. * The precipitate in each falcon is redispersed in 15 mL of hexane and 5 mL of absolute ethanol, before being centrifuged 10 minutes at 6000 rpm. The final precipitate is redispersed in a total volume of 20 mL of hexane.

** NB°1 : If at this stage the medium contains 3ML-CdSe NPL cf UV-visible absorption spectrum, which generally is not the case, one can redisperse the precipitate in hexane, centrifuge it, and keep the supernatant on which ethanol is added, before centrifugation and final redispersion in hexane.*

NB°2 : It is possible to double the quantity of Cd-oleate (0.808 g), of Se (0.054 g) and Cd(OAc)₂·2H₂O (0.280 g).

4.4.7 Self-assembly of 4ML-CdSe NPL

An amount of 4ML-CdSe NPL in hexane is diluted in order to get an absorbance of 2 at 513 nm. An amount of oleic acid (OA) is then added, varying the OA concentration in a typical range between 0.06 and 0.26 mol.L⁻¹.

The sample is sonicated under a sonic bath for 10 minutes before let to evolve (possibly let to evaporate) for at least 2 days. Twisted assemblies of typically 100 nm to 300 nm in length of individually twisted-4ML-CdSe NPL are obtained.

4.4.8 Self-assembly of 5ML-CdSe NPL

An appropriate amount of 5ML-CdSe NPL in hexane is diluted in hexane in order to get an absorbance at 552 nm of approximately 2 (total volume of 2 mL (resp. 5mL)). Oleic acid (OA) is then added, such as the final concentration in OA in the sample is fixed between 0.025 mol/L and 0.05 mol/L and adjusted in order to get threads of different lengths. The sample is sonicated for 10 minutes and the solvent is slowly evaporated. The sample is then characterized by TEM: NPL threads with an average length from 375 nm to 735 nm are generally obtained.

The solution is then diluted 500 times and spin-coated on a glass slide at 4000 rpm for 40 s. Finally, the sample is covered by a 30-nm layer of PMMA and observed on fluorescence microscopy.

Conclusion

We described in this thesis the morphological and conformational control of colloidal In_2S_3 and InS NPL along with the self-assembly of CdSe NPL.

We have first presented the shape-controlled solvothermal synthesis of $\gamma\text{-In}_2\text{S}_3$ nanomaterials from molecular precursors. The geometry of these nanomaterials varies from hexagonal nanoplatelets to long nanoribbons, according to a single experimental parameter: the amount of water inside the reaction medium. The dimensions of these nano-objects are determined from transmission electron microscopy observations: the nanoribbons are (8.7 ± 0.1) nm in width, (0.71 ± 0.04) nm in thickness and (1162 ± 44) nm in length. Rutherford backscattering spectrometry, X-Ray photoelectron spectroscopy, X-Ray diffraction and high-angle annular dark field scanning transmission electron microscopy experiments were performed to determine their composition and crystallographic structure.

Besides, we suggest a growth mechanism for $\gamma\text{-In}_2\text{S}_3$ nanomaterials according to preliminary results from time-resolved in-situ Small-Angle and Wide-Angle X-Ray Scattering experiments. A deeper interpretation of our data is still in progress and is expected to shed light on the exact growth mechanism of these 2D-nanomaterials.

Moreover, we showed NR tend to form bundles which form depends on the nature of the solvent. We are currently carrying on investigations on this topic to understand the nature and origin of the bundling from Small-Angle and Wide-Angle X-Ray Scattering experiments. It is worth to notice no bundling is obtained with cyclohexene or tetrahydrofuran. Controlling the colloidal stability of these strongly anisotropic nano-objects is of great interest in the prospect of potentially achieving liquid-crystal phase.

In chapter 3, we have reported the conformational control of orthorhombic $Pnmm$ InS nanoplatelets by surface ligand exchange. Indium sulfide nanoplatelets adopt a coiled conformation when they are natively capped with a monolayer of octylamine ligands. When octylamine is exchanged with a longer carbon-chain primary amine, the nanoplatelets uncoiled until reaching a flat conformation with C18 carbon-chain amines. Changing the amine surface ligand may change alkyl chain interactions within the ligand monolayer. Small changes in these low-energy interactions is sufficient to tune the stress induced by the ligands at the surface of the nanoplatelets. As a result, the nanoplatelets undergo under these surface stress a change in their geometrical conformation.

The investigation of the conformation of the nanoplatelets is achieved by transmission electron microscopy, from which their average curvature radius is evaluated as a function of the carbon chain length of the surface amine ligand.

The dimensions of unfolded NR are of (152 ± 4) nm in length for (9 ± 2) nm in width and (1.3 ± 0.2) nm in thickness. Their composition and crystallographic structure are determined from Rutherford backscattering spectrometry, X-Ray photoelectron spectroscopy, X-Ray diffraction, selected-area electron diffraction, energy-dispersive X-ray spectroscopy and high-angle annular dark field scanning transmission electron microscopy experiments.

Further studies are currently in progress as regards the possible reversibility of the unfolding process. Besides, adapting our ligand exchange protocol to chiral ligands might be relevant to induce new chiroptical properties to indium sulfide NR.

Finally, assembling nanoplatelets into larger superstructures can lead to new collective optical properties. For this purpose, we have carried out the syntheses and self-assembly of CdSe NPL. The syntheses of four-monolayer and five-monolayer CdSe NPL are realized from protocols previously established in our group.

Their self-assembly is realized by the addition of oleic acid in a suspension of CdSe NPL and resulting threads are imaged by transmission electron microscopy. Four-monolayer CdSe NPL self-assemble into short and twisted assemblies of individually strongly distorted NPL, whereas five-monolayer CdSe NPL self-assemble into long threads that can be either twisted or not.

In collaboration with Laurent Coolen from the Institut des nanosciences de Paris during Jiawen Liu's PhD, we have evidenced by microphotoluminescence strong homo-FRET within self-assembly of five-monolayer CdSe NPL. The exciton migration occurs along 500 nm (90 nanoplatelets) with a FRET rate of 1.5 ps^{-1} . The FRET efficiency between neighbouring NPL is of 99.99%. We thus demonstrate that new collective properties can originate from the self-assembly of semiconducting nanoplatelets.

The influence of the NPL thickness and center-to-center distance on the FRET phenomenon have to be evaluated, as well as its dependence as regard the morphology (twisted or straight) of the assembly.

It would be interesting to apply the ligand exchange protocol we develop here on indium sulfide NR to other materials, in order to generalize this conformation control method to all kind of semiconducting thin NPL. For instance, PbS NPL reported in the literature (Figure 1.13 on page 18, [33]) would be in that sense a potential candidate for further investigations.

This would open way to the design of shape-changing semiconducting systems under an external stimulus. Indeed, we can imagine that assembling such stimuli-responsive NPL would lead to superstructures whose overall shape would be affected by the individual NPL conformation. Indeed, assuming this conformation change can propagate over the all assembly, we would then be able to bend it or twist it by tuning the individual NPL conformation under an external stimulus such as a surface ligand exchange.

Finally, we can wonder on the outcome of a surface ligand exchange with chiral molecules. If such a ligand would affect the NPL shape, then we can expect to obtain chiral assemblies of NPL whose chiroptical properties would be tunable according to the chiral surface ligand used. That would be a ground-breaking achievement that the work presented here let us foreseen.

Bibliography

- [1] Gall, K.; Diao, J.; Dunn, M. L. *Nano Letters* **2004**, *4*, 2431–2436.
- [2] Sharma, A.; Hickman, J.; Gazit, N.; Rabkin, E.; Mishin, Y. *Nature Communications* **2018**, *9*, 4102.
- [3] Hezinger, A. F. E.; Teßmar, J.; Göpferich, A. *European Journal of Pharmaceutics and Biopharmaceutics* **2008**, *68*, 138–152.
- [4] Ithurria, S.; Tessier, M. D.; Mahler, B.; Lobo, R. P. S. M.; Dubertret, B.; Efros, A. L. *Nature Materials* **2011**, *10*, 936–941.
- [5] Ithurria, S.; Bousquet, G.; Dubertret, B. *Journal of the American Chemical Society* **2011**, *133*, 3070–3077.
- [6] Christodoulou, S.; Climente, J. I.; Planelles, J.; Brescia, R.; Prato, M.; Martín-García, B.; Khan, A. H.; Moreels, I. *Nano Letters* **2018**, *18*, 6248–6254.
- [7] Vasiliev, R. B.; Lazareva, E. P.; Karlova, D. A.; Garshev, A. V.; Yao, Y.; Kuroda, T.; Gaskov, A. M.; Sakoda, K. *Chemistry of Materials* **2018**, *30*, 1710–1717.
- [8] Rowland, C. E.; Fedin, I.; Zhang, H.; Gray, S. K.; Govorov, A. O.; Talapin, D. V.; Schaller, R. D. *Nature Materials* **2015**, *14*, 484–489.
- [9] Alivisatos, A. P. *Science* **1996**, *271*, 933–937.
- [10] Brus, L. E. *The Journal of Chemical Physics* **1984**, *80*, 4403–4409.
- [11] Murphy, C. J. *Analytical Chemistry* **2002**, *74*, 520A–526A.
- [12] Yang, Y. A.; Wu, H.; Williams, K. R.; Cao, Y. C. *Angewandte Chemie International Edition* **2005**, *44*, 6712–6715.
- [13] Ouyang, J.; Zaman, M. B.; Yan, F. J.; Johnston, D.; Li, G.; Wu, X.; Leek, D.; Ratcliffe, C. I.; Ripmeester, J. A.; Yu, K. *The Journal of Physical Chemistry C* **2008**, *112*, 13805–13811.
- [14] Boles, M. A.; Ling, D.; Hyeon, T.; Talapin, D. V. *Nature Materials* **2016**, *15*, 141–153.
- [15] Anderson, N. C.; Hendricks, M. P.; Choi, J. J.; Owen, J. S. *Journal of the American Chemical Society* **2013**, *135*, 18536–18548.
- [16] Yin, Y.; Alivisatos, A. P. *Nature* **2005**, *437*, 664–670.
- [17] Berends, A. C.; de Mello Donega, C. *The Journal of Physical Chemistry Letters* **2017**, *8*, 4077–4090.

- [18] Murray, C. B.; Norris, D. J.; Bawendi, M. G. *Journal of the American Chemical Society* **1993**, *115*, 8706–8715.
- [19] Owen, J. *Science* **2015**, *347*, 615–616.
- [20] Houtepen, A. J.; Hens, Z.; Owen, J. S.; Infante, I. *Chemistry of Materials* **2017**, *29*, 752–761.
- [21] Nirmal, M.; Dabbousi, B. O.; Bawendi, M. G.; Macklin, J. J.; Trautman, J. K.; Harris, T. D.; Brus, L. E. *Nature* **1996**, *383*, 802–804.
- [22] Klimov, V. I.; Mikhailovsky, A. A.; Xu, S.; Malko, A.; Hollingsworth, J. A.; Leatherdale, C. A.; Eisler, H.-J.; Bawendi, M. G. *Science* **2000**, *290*, 314–317.
- [23] Keuleyan, S.; Lhuillier, E.; Brajuskovic, V.; Guyot-Sionnest, P. *Nature Photonics* **2011**, *5*, 489–493.
- [24] Talapin, D. V.; Lee, J.-S.; Kovalenko, M. V.; Shevchenko, E. V. *Chemical Reviews* **2010**, *110*, 389–458.
- [25] Caputo, J. A.; Frenette, L. C.; Zhao, N.; Sowers, K. L.; Krauss, T. D.; Weix, D. J. *Journal of the American Chemical Society* **2017**, *139*, 4250–4253.
- [26] Purcell-Milton, F.; Govan, J.; Mukhina, M.; Gunko, Y. *Nanoscale Horiz.* **2016**, *1*, 14–26.
- [27] Mazumder, S.; Dey, R.; Mitra, M. K.; Mukherjee, S.; Das, G. C. *Journal of Nanomaterials* **2009**, *2009*, e815734.
- [28] Li, L.-s.; Hu, J.; Yang, W.; Alivisatos, A. P. *Nano Letters* **2001**, *1*, 349–351.
- [29] Tang, Z.; Kotov, N. A.; Giersig, M. *Science* **2002**, *297*, 237–240.
- [30] Park, H.; Chung, H.; Kim, W. *Materials Letters* **2013**, *99*, 172–175.
- [31] Cunningham, P. D.; Coropceanu, I.; Mulloy, K.; Cho, W.; Talapin, D. V. *ACS Nano* **2020**, *14*, 3847–3857.
- [32] Schliehe, C.; Juarez, B. H.; Pelletier, M.; Jander, S.; Greshnykh, D.; Nagel, M.; Meyer, A.; Foerster, S.; Kornowski, A.; Klinke, C.; Weller, H. *Science* **2010**, *329*, 550–553.
- [33] Akkerman, Q. A.; Martín-García, B.; Buha, J.; Almeida, G.; Toso, S.; Marras, S.; Bonaccorso, F.; Petralanda, U.; Infante, I.; Manna, L. *Chemistry of Materials* **2019**, *31*, 8145–8153.
- [34] Kubie, L.; Martinez, M. S.; Miller, E. M.; Wheeler, L. M.; Beard, M. C. *Journal of the American Chemical Society* **2019**, *141*, 12121–12127.
- [35] Lauth, J.; Gorris, F. E. S.; Samadi Khoshkhoo, M.; Chassé, T.; Friedrich, W.; Lebedeva, V.; Meyer, A.; Klinke, C.; Kornowski, A.; Scheele, M.; Weller, H. *Chemistry of Materials* **2016**, *28*, 1728–1736.
- [36] Almeida, G.; Dogan, S.; Bertoni, G.; Giannini, C.; Gaspari, R.; Perissinotto, S.; Krahne, R.; Ghosh, S.; Manna, L. *Journal of the American Chemical Society* **2017**, *139*, 3005–3011.
- [37] Park, K. H.; Jang, K.; Son, S. U. *Angewandte Chemie International Edition* **2006**, *45*, 4608–4612.
- [38] Lhuillier, E.; Pedetti, S.; Ithurria, S.; Nadal, B.; Heuclin, H.; Dubertret, B. *Accounts of Chemical Research* **2015**, *48*, 22–30.
- [39] Ithurria, S.; Dubertret, B. *Journal of the American Chemical Society* **2008**, *130*, 16504–16505.
- [40] Son, J. S. *et al. Angewandte Chemie* **2009**, *121*, 6993–6996.
- [41] Wang, F.; Wang, Y.; Liu, Y.-H.; Morrison, P. J.; Loomis, R. A.; Buhro, W. E. *Accounts of Chemical Research* **2015**, *48*, 13–21.

- [42] Diroll, B. T. *Journal of Materials Chemistry C* **2020**, *8*, 10628–10640.
- [43] Jana, S.; Frutos, M. d.; Davidson, P.; Abécassis, B. *Science Advances* **2017**, *3*, e1701483.
- [44] Jana, S.; Davidson, P.; Abécassis, B. *Angewandte Chemie International Edition* **2016**, *55*, 9371–9374.
- [45] Bouet, C.; Mahler, B.; Nadal, B.; Abecassis, B.; Tessier, M. D.; Ithurria, S.; Xu, X.; Dubertret, B. *Chemistry of Materials* **2013**, *25*, 639–645.
- [46] Guzelturk, B.; Olutas, M.; Delikanli, S.; Kelestemur, Y.; Erdem, O.; Demir, H. V. *Nanoscale* **2015**, *7*, 2545–2551.
- [47] Scott, R.; Heckmann, J.; Prudnikau, A. V.; Antanovich, A.; Mikhailov, A.; Owschimikow, N.; Artemyev, M.; Climente, J. I.; Woggon, U.; Grosse, N. B.; Achtstein, A. W. *Nature Nanotechnology* **2017**, *12*, 1155–1160.
- [48] Abécassis, B.; Tessier, M. D.; Davidson, P.; Dubertret, B. *Nano Letters* **2014**, *14*, 710–715.
- [49] Ma, X.; Diroll, B. T.; Cho, W.; Fedin, I.; Schaller, R. D.; Talapin, D. V.; Wiederrecht, G. P. *Nano Letters* **2018**, *18*, 4647–4652.
- [50] Feng, F.; Nguyen, L. T.; Nasilowski, M.; Nadal, B.; Dubertret, B.; Coolen, L.; Maître, A. *Nano Research* **2018**, *11*, 3593–3602.
- [51] Grim, J. Q.; Christodoulou, S.; Stasio, F. D.; Krahne, R.; Cingolani, R.; Manna, L.; Moreels, I. *Nature Nanotechnology* **2014**, *9*, 891–895.
- [52] Guzelturk, B.; Kelestemur, Y.; Olutas, M.; Delikanli, S.; Demir, H. V. *ACS Nano* **2014**, *8*, 6599–6605.
- [53] She, C.; Fedin, I.; Dolzhenkov, D. S.; Dahlberg, P. D.; Engel, G. S.; Schaller, R. D.; Talapin, D. V. *ACS Nano* **2015**, *9*, 9475–9485.
- [54] LaMer, V. K.; Dinegar, R. H. *Journal of the American Chemical Society* **1950**, *72*, 4847–4854.
- [55] Whitehead, C. B.; Özkar, S.; Finke, R. G. *Chemistry of Materials* **2019**, *31*, 7116–7132.
- [56] Donegá, C. d. M. *Chemical Society Reviews* **2011**, *40*, 1512–1546.
- [57] Reiss, H. *The Journal of Chemical Physics* **1951**, *19*, 482–487.
- [58] Handwerk, D. R.; Shipman, P. D.; Whitehead, C. B.; Özkar, S.; Finke, R. G. *Journal of the American Chemical Society* **2019**, *141*, 15827–15839.
- [59] Riedinger, A.; Ott, F. D.; Mule, A.; Mazzotti, S.; Knüsel, P. N.; Kress, S. J. P.; Prins, F.; Erwin, S. C.; Norris, D. J. *Nature Materials* **2017**, *16*, 743–748.
- [60] Jiang, Y.; Ojo, W.-S.; Mahler, B.; Xu, X.; Abécassis, B.; Dubertret, B. *ACS Omega* **2018**, *3*, 6199–6205.
- [61] Huang, X.; Parashar, V. K.; Gijs, M. A. M. *ACS Central Science* **2019**, *5*, 1017–1023.
- [62] Delikanli, S. *et al. Advanced Functional Materials* **2019**, *29*, 1901028.
- [63] Kurtina, D. A.; Garshev, A. V.; Vasil'eva, I. S.; Shubin, V. V.; Gaskov, A. M.; Vasiliev, R. B. *Chemistry of Materials* **2019**, *31*, 9652–9663.
- [64] Cho, W.; Kim, S.; Coropceanu, I.; Srivastava, V.; Diroll, B. T.; Hazarika, A.; Fedin, I.; Galli, G.; Schaller, R. D.; Talapin, D. V. *Chemistry of Materials* **2018**, *30*, 6957–6960.
- [65] Nasilowski, M.; Mahler, B.; Lhuillier, E.; Ithurria, S.; Dubertret, B. *Chemical Reviews* **2016**, *116*, 10934–10982.

- [66] Castro, N.; Bouet, C.; Ithurria, S.; Lequeux, N.; Constantin, D.; Levitz, P.; Pontoni, D.; Abécassis, B. *Nano Letters* **2019**, *19*, 6466–6474.
- [67] Chen, Y.; Chen, D.; Li, Z.; Peng, X. *Journal of the American Chemical Society* **2017**, *139*, 10009–10019.
- [68] Wang, Y.; Zhou, Y.; Zhang, Y.; Buhro, W. E. *Inorganic Chemistry* **2015**, *54*, 1165–1177.
- [69] Dufour, M.; Qu, J.; Greboval, C.; Méthivier, C.; Lhuillier, E.; Ithurria, S. *ACS Nano* **2019**, *13*, 5326–5334.
- [70] Hutter, E. M.; Bladt, E.; Goris, B.; Pietra, F.; van der Bok, J. C.; Boneschanscher, M. P.; de Mello Donegá, C.; Bals, S.; Vanmaekelbergh, D. *Nano Letters* **2014**, *14*, 6257–6262.
- [71] Meulenbergh, R. W.; Jennings, T.; Strouse, G. F. *Physical Review B* **2004**, *70*, 235311.
- [72] Ghafouri, R.; Bruinsma, R. *Physical Review Letters* **2005**, *94*, 138101.
- [73] Liu, Y.; Rowell, N.; Willis, M.; Zhang, M.; Wang, S.; Fan, H.; Huang, W.; Chen, X.; Yu, K. *The Journal of Physical Chemistry Letters* **2019**, *10*, 2794–2801.
- [74] Wang, P.-p.; Yang, Y.; Zhuang, J.; Wang, X. *Journal of the American Chemical Society* **2013**, *135*, 6834–6837.
- [75] Ni, B.; Liu, H.; Wang, P.-p.; He, J.; Wang, X. *Nature Communications* **2015**, *6*, 8756.
- [76] Acharya, S.; Sarkar, S.; Pradhan, N. *The Journal of Physical Chemistry Letters* **2012**, *3*, 3812–3817.
- [77] Berger, R.; Delamarche, E.; Lang, H. P.; Gerber, C.; Gimzewski, J. K.; Meyer, E.; Güntherodt, H.-J. *Science* **1997**, *276*, 2021–2024.
- [78] Armon, S.; Efrati, E.; Kupferman, R.; Sharon, E. *Science* **2011**, *333*, 1726–1730.
- [79] Antanovich, A.; Achtstein, A. W.; Matsukovich, A.; Prudnikau, A.; Bhaskar, P.; Gurin, V.; Molinari, M.; Artemyev, M. *Nanoscale* **2017**, *9*, 18042–18053.
- [80] Tepliakov, N. V.; Baimuratov, A. S.; Vovk, I. A.; Leonov, M. Y.; Baranov, A. V.; Fedorov, A. V.; Rukhlenko, I. D. *ACS Nano* **2017**, *11*, 7508–7515.
- [81] Baimuratov, A. S.; Gun'ko, Y. K.; Shalkovskiy, A. G.; Baranov, A. V.; Fedorov, A. V.; Rukhlenko, I. D. *Advanced Optical Materials* **2017**, *5*, 1600982.
- [82] Baimuratov, A. S.; Pereziabova, T. P.; Leonov, M. Y.; Zhu, W.; Baranov, A. V.; Fedorov, A. V.; Gun'ko, Y. K.; Rukhlenko, I. D. *ACS Nano* **2018**, *12*, 6203–6209.
- [83] Bai, P.; Hu, A.; Liu, Y.; Jin, Y.; Gao, Y. *The Journal of Physical Chemistry Letters* **2020**, *11*, 4524–4529.
- [84] Abécassis, B. *ChemPhysChem* **2016**, *17*, 618–631.
- [85] Batista, C. A. S.; Larson, R. G.; Kotov, N. A. *Science* **2015**, *350*, 1242477.
- [86] Widmer-Cooper, A.; Geissler, P. *Nano Letters* **2014**, *14*, 57–65.
- [87] Widmer-Cooper, A.; Geissler, P. L. *ACS Nano* **2016**, *10*, 1877–1887.
- [88] Winslow, S. W.; Swan, J. W.; Tisdale, W. A. *Journal of the American Chemical Society* **2020**, *142*, 9675–9685.
- [89] Jana, S.; Phan, T. N. T.; Bouet, C.; Tessier, M. D.; Davidson, P.; Dubertret, B.; Abécassis, B. *Langmuir* **2015**, *31*, 10532–10539.

- [90] Kim, D.; Lee, D. C. *The Journal of Physical Chemistry Letters* **2020**, *11*, 2647–2657.
- [91] Antanovich, A.; Prudnikau, A.; Matsukovich, A.; Achtstein, A.; Artemyev, M. *The Journal of Physical Chemistry C* **2016**, *120*, 5764–5775.
- [92] Monego, D.; Kister, T.; Kirkwood, N.; Mulvaney, P.; Widmer-Cooper, A.; Kraus, T. *Langmuir* **2018**, *34*, 12982–12989.
- [93] Kister, T.; Monego, D.; Mulvaney, P.; Widmer-Cooper, A.; Kraus, T. *ACS Nano* **2018**, *12*, 5969–5977.
- [94] Monego, D.; Kister, T.; Kirkwood, N.; Doblus, D.; Mulvaney, P.; Kraus, T.; Widmer-Cooper, A. *ACS Nano* **2020**, *14*, 5278–5287.
- [95] Dong, A.; Chen, J.; Vora, P. M.; Kikkawa, J. M.; Murray, C. B. *Nature* **2010**, *466*, 474–477.
- [96] Erdem, O.; Foroutan, S.; Gheshlaghi, N.; Guzelturk, B.; Altintas, Y.; Demir, H. V. *Nano Letters* **2020**, *20*, 6459–6465.
- [97] Gao, Y.; Weidman, M. C.; Tisdale, W. A. *Nano Letters* **2017**, *17*, 3837–3843.
- [98] Momper, R.; Zhang, H.; Chen, S.; Halim, H.; Johannes, E.; Yordanov, S.; Braga, D.; Blülle, B.; Doblus, D.; Kraus, T.; Bonn, M.; Wang, H. I.; Riedinger, A. *Nano Letters* **2020**, *20*, 4102–4110.
- [99] Guzelturk, B.; Erdem, O.; Olutas, M.; Kelestemur, Y.; Demir, H. V. *ACS Nano* **2014**, *8*, 12524–12533.
- [100] Erdem, O.; Olutas, M.; Guzelturk, B.; Kelestemur, Y.; Demir, H. V. *The Journal of Physical Chemistry Letters* **2016**, *7*, 548–554.
- [101] Dalas, E.; Sakkopoulos, S.; Vitoratos, E.; Maroulis, G.; Kobotiatis, L. *Journal of Materials Science* **1993**, *28*, 5456–5460.
- [102] Choe, S.-H.; Bang, T.-H.; Kim, N.-O.; Kim, H.-G.; Lee, C.-I.; Jin, M.-S.; Oh, S.-K.; Kim, W.-T. *Semiconductor Science and Technology* **2001**, *16*, 98–102.
- [103] Gorai, S.; Guha, P.; Ganguli, D.; Chaudhuri, S. *Materials Chemistry and Physics* **2003**, *82*, 974–979.
- [104] Tang, J.; Konstantatos, G.; Hinds, S.; Myrskog, S.; Pattantyus-Abraham, A. G.; Clifford, J.; Sargent, E. H. *ACS Nano* **2009**, *3*, 331–338.
- [105] Acharya, S.; Dutta, M.; Sarkar, S.; Basak, D.; Chakraborty, S.; Pradhan, N. *Chemistry of Materials* **2012**, *24*, 1779–1785.
- [106] Li, M.; Tu, X.; Su, Y.; Lu, J.; Hu, J.; Cai, B.; Zhou, Z.; Yang, Z.; Zhang, Y. *Nanoscale* **2018**, *10*, 1153–1161.
- [107] Kim, Y. H.; Lee, J. H.; Shin, D.-W.; Park, S. M.; Moon, J. S.; Nam, J. G.; Yoo, J.-B. *Chemical Communications* **2010**, *46*, 2292–2294.
- [108] Franzman, M. A.; Brutchey, R. L. *Chemistry of Materials* **2009**, *21*, 1790–1792.
- [109] Sarkar, S.; Leach, A. D. P.; Macdonald, J. E. *Chemistry of Materials* **2016**, *28*, 4324–4330.
- [110] Du, W.; Zhu, J.; Li, S.; Qian, X. *Crystal Growth & Design* **2008**, *8*, 2130–2136.
- [111] Liu, G.; Jiao, X.; Qin, Z.; Chen, D. *CrystEngComm* **2010**, *13*, 182–187.
- [112] Tian, Y.; Wang, L.; Tang, H.; Zhou, W. *Journal of Materials Chemistry A* **2015**, *3*, 11294–11301.
- [113] Wang, H.-Y.; Li, X.-F.; Xu, L.; Li, X.-S.; Hu, Q.-K. *Communications in Theoretical Physics* **2018**, *69*, 211.

- [114] Kushwaha, P.; Patra, A.; Anjali, E.; Surdi, H.; Singh, A.; Gurada, C.; Ramakrishnan, S.; Prabhu, S.; Venu Gopal, A.; Thamizhavel, A. *Optical Materials* **2014**, *36*, 616–620.
- [115] Datta, A.; Gorai, S.; Panda, S. K.; Chaudhuri, S. *Crystal Growth & Design* **2006**, *6*, 1010–1013.
- [116] Gorai, S.; Datta, A.; Chaudhuri, S. *Materials Letters* **2005**, *59*, 3050–3053.
- [117] Holder, C. F.; Schaak, R. E. *ACS Nano* **2019**, *13*, 7359–7365.
- [118] Pistor, P.; Merino Álvarez, J. M.; León, M.; di Michiel, M.; Schorr, S.; Klenk, R.; Lehmann, S. *Acta Crystallographica Section B Structural Science, Crystal Engineering and Materials* **2016**, *72*, 410–415.
- [119] Diehl, R.; Carpentier, C.-D.; Nitsche, R. *Acta Crystallographica Section B: Structural Crystallography and Crystal Chemistry* **1976**, *32*, 1257–1260.
- [120] Barreau, N. *Solar Energy* **2009**, *83*, 363–371.
- [121] Turan, E.; Zor, M.; Kul, M.; Aybek, A. S.; Taskopru, T. *Philosophical Magazine* **2012**, *92*, 1716–1726.
- [122] Sharma, Y.; Srivastava, P. *Materials Chemistry and Physics* **2012**, *135*, 385–394.
- [123] Singh, S.; Tomar, R.; ten Brinck, S.; De Roo, J.; Geiregat, P.; Martins, J. C.; Infante, I.; Hens, Z. *Journal of the American Chemical Society* **2018**, *140*, 13292–13300.
- [124] Mayer, M. “SIMNRA User’s Guide”, 1997.
- [125] Ye, F.; Wang, C.; Du, G.; Chen, X.; Zhong, Y.; Jiang, J. Z. *Journal of Materials Chemistry* **2011**, *21*, 17063–17065.
- [126] Xing, Y.; Zhang, H.; Song, S.; Feng, J.; Lei, Y.; Zhao, L.; Li, M. *Chemical Communications* **2008**, 1476–1478.
- [127] Lutfi Abdelhady, A.; Ramasamy, K.; Malik, M. A.; O’Brien, P. *Materials Letters* **2013**, *99*, 138–141.
- [128] Zhou, Y.; Wang, F.; Buhro, W. E. *Journal of the American Chemical Society* **2015**, *137*, 15198–15208.
- [129] Zhou, Y.; Buhro, W. E. *Journal of the American Chemical Society* **2017**, *139*, 12887–12890.
- [130] Hens, Z.; Martins, J. C. *Chemistry of Materials* **2013**, *25*, 1211–1221.
- [131] Fritzing, B.; Capek, R. K.; Lambert, K.; Martins, J. C.; Hens, Z. *Journal of the American Chemical Society* **2010**, *132*, 10195–10201.
- [132] Horani, F.; Lifshitz, E. *Chemistry of Materials* **2019**, *31*, 1784–1793.
- [133] Abécassis, B.; Bouet, C.; Garnero, C.; Constantin, D.; Lequeux, N.; Ithurria, S.; Dubertret, B.; Pauw, B. R.; Pontoni, D. *Nano Letters* **2015**, *15*, 2620–2626.
- [134] Maes, J.; Castro, N.; De Nolf, K.; Walravens, W.; Abécassis, B.; Hens, Z. *Chemistry of Materials* **2018**, *30*, 3952–3962.
- [135] Kikhney, A. G.; Svergun, D. I. *FEBS Letters* **2015**, *589*, 2570–2577.
- [136] Als-Nielsen, J. A.; McMorro, D. - Section 4.5. Small-angle X-ray scattering (SAXS), pp.134-146. In *Elements of Modern X-ray Physics*; John Wiley & Sons: 2011.
- [137] “What is measured in a Small Angle X-ray Scattering (SAXS) ?”, http://iramis.cea.fr/Phocea/Vie_des_labos/Ast/ast_sstechnique.php?id_ast=1065.

- [138] Gao, H.; Bettscheider, S.; Kraus, T.; Müser, M. H. *Nano Letters* **2019**, *19*, 6993–6999.
- [139] Narayanan, T.; Sztucki, M.; Van Vaerenbergh, P.; Léonardon, J.; Gorini, J.; Claustre, L.; Sever, F.; Morse, J.; Boesecke, P. *Journal of Applied Crystallography* **2018**, *51*, 1511–1524.
- [140] Mary, H.; Brouhard, G. J. *bioRxiv* **2019**, 852772.
- [141] Constantin, D. *Journal of Applied Crystallography* **2015**, *48*, 1901–1906.
- [142] Grossmann, A.; Erley, W.; Ibach, H. *Surface Science* **1994**, *313*, 209–214.
- [143] Ibach, H. *Journal of Vacuum Science & Technology A: Vacuum, Surfaces, and Films* **1998**, *12*, 2240.
- [144] Moloney, M. P.; Gun'ko, Y. K.; Kelly, J. M. *Chemical Communications (Cambridge, England)* **2007**, 3900–3902.
- [145] Elliott, S. D.; Moloney, M. P.; Gun'ko, Y. K. *Nano Letters* **2008**, *8*, 2452–2457.
- [146] Tohgha, U.; Varga, K.; Balaz, M. *Chemical Communications* **2013**, *49*, 1844–1846.
- [147] Purcell-Milton, F.; McKenna, R.; Brennan, L. J.; Cullen, C. P.; Guillemeney, L.; Tepliakov, N. V.; Baimuratov, A. S.; Rukhlenko, I. D.; Perova, T. S.; Duesberg, G. S.; Baranov, A. V.; Fedorov, A. V.; Gun'ko, Y. K. *ACS Nano* **2018**, *12*, 954–964.
- [148] Moloney, M. P.; Govan, J.; Loudon, A.; Mukhina, M.; Gun'ko, Y. K. *Nature Protocols* **2015**, *10*, 558.
- [149] Tohgha, U.; Deol, K. K.; Porter, A. G.; Bartko, S. G.; Choi, J. K.; Leonard, B. M.; Varga, K.; Kubelka, J.; Muller, G.; Balaz, M. *ACS Nano* **2013**, *7*, 11094–11102.
- [150] Ma, W.; Xu, L.; de Moura, A. F.; Wu, X.; Kuang, H.; Xu, C.; Kotov, N. A. *Chemical Reviews* **2017**, *117*, 8041–8093.
- [151] Hendricks, M. P.; Campos, M. P.; Cleveland, G. T.; Plante, I. J.-L.; Owen, J. S. *Science* **2015**, *348*, 1226–1230.
- [152] Kim, W. D.; Yoon, D.-E.; Kim, D.; Koh, S.; Bae, W. K.; Chae, W.-S.; Lee, D. C. *The Journal of Physical Chemistry C* **2019**, *123*, 9445–9453.
- [153] Akselrod, G. M.; Prins, F.; Poulikakos, L. V.; Lee, E. M. Y.; Weidman, M. C.; Mork, A. J.; Willard, A. P.; Bulović, V.; Tisdale, W. A. *Nano Letters* **2014**, *14*, 3556–3562.
- [154] Lee, E. M. Y.; Tisdale, W. A. *The Journal of Physical Chemistry C* **2015**, *119*, 9005–9015.
- [155] Liu, J.; Guillemeney, L.; Abécassis, B.; Coolen, L. *Nano Letters* **2020**, *20*, 3465–3470.
- [156] Guzelturk, B.; Demir, H. V. *Advanced Functional Materials* **2016**, *26*, 8158–8177.
- [157] Kholmicheva, N.; Moroz, P.; Bastola, E.; Razgoniaeva, N.; Bocanegra, J.; Shaughnessy, M.; Porach, Z.; Khon, D.; Zamkov, M. *ACS Nano* **2015**, *9*, 2926–2937.
- [158] Gilmore, R. H.; Lee, E. M. Y.; Weidman, M. C.; Willard, A. P.; Tisdale, W. A. *Nano Letters* **2017**, *17*, 893–901.
- [159] Mikhnenko, O. V.; Blom, P. W. M.; Nguyen, T.-Q. *Energy & Environmental Science* **2015**, *8*, 1867–1888.

BIBLIOGRAPHY

List of Figures

1	Number of publications with the key-word "nanoplatelets" per year, from ISI Web of Knowledge in May 2021, on a total of 8033 records since 1995.	xiv
1.1	Conversion of molecular orbitals (right) into bands (left) and size-dependence of the band-gap for a nanomaterial, here quantum dots (middle).	2
1.2	Band structures of insulator, conductor and semiconductor.	3
1.3	(A.) Transmission electron microscopy (TEM) image of CdSe nanocrystals from [16] - (B., C.) Transmission electron images of CdSe nanocrystals with hexagonal structure viewed down different crystallographic axes. From [9] - (D.) Colloidal suspension of CdSe QD with different sizes under UV illumination. The NC size decreases from left to right (6 to 2 nm) and the corresponding increase in the bandgap is reflected in the change of the photoluminescence color from red to blue. From [17] - (E.) Evolution of the fluorescence (left, f) and absorption (right, A) properties of CdSe nanocrystals with the reaction temperature and time. From reference [12].	4
1.4	Energy-level diagram showing promotion of an electron from the valence band to the conduction band and the existence of trap levels within the material, from [11].	5
1.5	Schematic representation of the density of states of a bulk semiconductor and of semiconductor nanostructures with reduced dimensionality, from 2D (step-like continuum) to 0D (discrete levels) by way of 1D (saw-like quasicontinuum). From [17].	7
1.6	TEM images of zinc blende (a.) CdSe, (b.) CdS, (c.) CdTe, wurtzite (d.) CdSe, and (e.) ZnS and rock salt (f.) PbS NPL - (g.) TEM images of (from left to right) CdSe/CdS core/crown NPL, core only CdSe NPL and core/shell CdSe/CdS NPL, from [38].	8
1.7	Schematic representation of the atomic arrangements of the thin edge of 4.5 ML zinc-blende (a.) and 4ML wurtzite CdX (X=Se, Te or S) NPL (b.) from [41]. Red solid lines identify the biatomic (Cd-X) monolayers ML. d_{ML} (in a.) represents the thickness of a ML, d is the one of the nanocrystals. d_{ML-ML} (in b.) is defined as the inter-ML distance. a is the lattice parameter for the cubic (a.) or hexagonal (b.) unit cell. .	8

1.8	(a) TEM image of rectangular (22 nm x 7nm x 1.5 nm) zinc-blende 5.5 ML CdSe NPL, from [43] - (b) TEM image of 18 nm ² square 4.5 ML zinc-blende CdSe NPL, from [44], of a thickness of 1.2 nm from [4] -(c.) Absorption and emission spectra of 4- and 5-ML CdSe NPL illustrate the red-shifting of the spectra when the NPL get thicker. From [8] . . .	9
1.9	Schematic illustration of the LaMer model, plotting the monomer concentration through the reaction time. Step I, II and III are described in the text above. Graph from ref [55].	12
1.10	Possible mechanisms for CdSe NPL lateral extension, from [5]. Initially, isotropic seeds with dimensions < 2 nm are formed from reaction between Cd and Se precursors - <i>Path 1 and path 3</i> : Self-organization of seeds (oriented attachments) at seed level (path 1) or in patches (path 3) - <i>Path 2</i> : Anisotropic growth through the continuous incorporation of soluble monomers onto existing NPL.	14
1.11	Procedure to synthesize CdSe nanoplatelets from a templating method, from [40].	15
1.12	(a.) Characteristic ribbon configuration, from left to right : helicoid, isometric spiral and intermediate configuration, from [72] - (b.) Ribbon energy minimum E(w) as a function of the ribbon width w (schematic). The curve marked A corresponds to a larger value of the Foppl-von Karman γ and B to a lower value. From [72].	17
1.13	(a.). HAADF-STEM images of twisted NPL (helicoid) after addition of oleic acid on a solution of flat NPL, from [43] - (b.) HAADF-STEM images of helical NPL (isometric spiral) which conformation in solution is fixed by a coating with silica, from [70] - TEM images of : (c.) In ₂ S ₃ coiled nanoribbons [74] and (d.) Hexagonal In ₂ Se ₃ NPL [36] - (e.) PbS rectangular nanosheets [33] - (f.) ZnSe quantum belts [31] - (g.) CdSe nanotubes [45] - (h.) SEM image of CdSe multiwalled nanotubes [61].	18
1.14	(a.) Scheme of a NPL which undergoes a spontaneous folding to release stress imposed on its surfaces, symbolized by brown arrows - TEM images of 3ML-CdSe capped with (b.) oleic acid, (c.) chloride, (d.) bromide ,(e.) iodide, from [69] - (f.) Closed and open seed pods, from [78].	20
1.15	a. Scheme of lattice transformation on 4ML-CdSe NPL upon ligand exchange of oleic acid (OA) by hexadecylphosphonic acid (HDPa) - b. Variation of lattice parameters of 4ML-CdSe NPL capped with OA, HDPa or hexadecanethiol (HDT) - c. Evolution of absorption and photoluminescence of 4ML-CdSe NPL with the surface ligand, from [79].	21
1.16	(a.) Virtual unrolling of tapered nanoscroll into flat but topologically distorted NPL by a coordinate replacement and (b.) Absorption spectrum and CD spectra of the two optical isomers of the nanoscroll. Dashed curves in absorption spectrum feature the distinctive absorption bands of the transitions with the same quantum number of electron and hole. From [80].	22
1.17	(a.) Compression or stretching of CdSe nanosprings modifies their (b.) absorption and CD peaks at 260 meV, as well as the entire absorption, CD, and dissymmetry factor spectra. From [82].	22

1.18	Ligand density (top) and solvent density (bottom) around CdS core of isolated nanorods in hexane at 300 K (left) and 340 K (right). x and y scales are in nanometers, contour scale in g/cm^3 . The black hexagon indicates the position of the CdS core. Ligands order at low temperature, making the ligand-solvent interface more sharply and aligning the solvent molecules into layers: self-assembly between two rods is then favoured in this configuration. At higher temperature, the decrease in ligand ordering create entropic repulsions between ligand chains and disfavoured self-assembly. From [86].	24
1.19	Interfacial self-assembly of CdSe nanoplatelet monolayer films. Left panel: Illustration of the equipment used for self-assembly and schematic of the face-down and edge-up configurations. (a,b) TEM images of the face-down and edge-up assemblies, respectively. From [97]	26
1.20	Evaporation driven self-assembly of 4ML-CdSe NPL using a liquid-liquid interface. (a) TEM images illustrating the change of the dispersing solvent of the NPL on the assembly configuration: While reducing the vapor pressure (from hexane to heptane and octane at 20°C), the assembly configuration is tuned from a face-down (left) to an edge-up (right) configuration by way of a mixture of both (middle). (b) TEM images of assemblies realised at 5°C : edge-up assemblies are obtained in all cases. From [98].	27
1.21	Self-assembly of 4ML-CdSe NPL in solution. (A,B) TEM images of threads of face-to-face stacked CdSe NPL. (C) Fluorescence microscopy images of the same threads deposited from solution on a cover slip. From [44].	28
1.22	(A to D) TEM images of twisted threads of CdSe NPL of various lengths. (E, F) HAADF-STEM images of the same threads. (G) SAXS pattern of a dispersion of twisted ribbons. The two scattering peaks, at 1.0075 and 2.0141 nm^{-1} , respectively, are the first and second orders of diffraction from the NPL stacking and give the stacking period $d = 5.84 \text{ nm}$. From this period, it is deduced that there are around 70 NPLs within one pitch and that the mean rotation angle between two adjacent NPL is 5° . (H) Electron tomographic reconstruction of a twisted ribbon. From [43].	29
1.23	(a) FRET principle. Among other factors, non-radiative FRET between donor (blue circle) and acceptor chromophores (red circle) requires non-zero spectral overlap between the donor emission spectrum and the acceptor absorption spectrum. The donor species absorbs at blue wavelengths (blue solid line) and emits in the green (green dashed line). It exhibits spectral overlap (shaded green) with an energy acceptor species that absorbs in the green (solid green line) and emits in the red (dashed red line). Absorption and emission spectra of 4ML- and 5ML-CdSe NPL reveal the potential for energy transfer from 4ML- to 5ML-NPL. From [8] - (b) Long range exciton hopping in stacked NPL through homo-FRET. The nonemissive NPL in the stack causes trapping of the excitons which recombine nonradiatively, resulting in a decrease on the overall quantum yield and on fluorescence lifetime. From [99].	31

2.1	TEM images of: (a.) 63 nm-hexagonal In_2S_3 nanoplates [37] - (b.) In_2S_3 nanorods [108] - (c.) In_2S_3 nanotubes, The inset shows a high-resolution TEM image of a nanotube with a wall thickness of 0.79 nm. [107] - (d.) In_2S_3 wrinkled sheets [76] - (e.) In_2S_3 nanotubes [111] - (f.) In_2S_3 nanocoils [75, 74] that assemble in (g.) single-walled nanotubes through oriented attachment [75] - (h.) In_2S_3 nanobelts [110].	35
2.2	Map of temperature-dependent X-ray diffractograms for In_2S_3 powder, from [118]. The colours indicate the XRD intensity in logarithmic scale (dark blue: low intensity, red: high density).	36
2.3	(a.). Scheme of the experimental conditions - (b.). Left: Colloidal solution of nanoribbons dispersed in toluene, Right: Nanoribbons in the powder form.	37
2.4	(a., b., c.) TEM images of In_2S_3 NR lying flat. Insert in (a.) is a gray scale histogram of the underlying image, showing the uniform thickness of the NR as only two peaks are seen (background and NR) - (d., e., f.) HAADF-STEM images of the same NR, viewed both lying flat and on edge, acquired with the help of Benoit Mahler from the Institut Lumière Matière of Lyon.	37
2.5	RBS spectrum for In_2S_3 NR: the experimental data are fitted in order to obtain the chemical composition of the sample, written below the spectrum. The results leads to In_2S_3 empirical formula for NR. The spectrum and its interpretation were realized with the help of Bruno Canut from the Institute of Nanotechnologies of Lyon.	38
2.6	X-ray diffractogram of In_2S_3 NR (blue) along the one of oleylamine (red) from which originates the peak at 19.5°	39
2.7	(a., b.) HAADF-STEM images of In_2S_3 NR lying respectively flat and on edge, acquired with the help of Benoit Mahler from the ILM Lyon. Inserts are Fourier transforms of yellow boxes. These patterns match with computed electron diffractograms of $\gamma\text{-In}_2\text{S}_3$ for an observation of the modelled structure respectively along the normal vectors of (001) and (100) planes - (b., d.) Modelling of $\gamma\text{-In}_2\text{S}_3$ NR with a thickness along the c-axis of a single unit cell length. The crystallographic model is viewed along the normal to the (001) (b.) or (100) (d.) planes. The different figures are measurements realized on HAADF-STEM images and modelled NR, and are discussed in the main text - (e.) Trigonal ($P\bar{3}m1$) $\gamma\text{-In}_2\text{S}_3$ unit-cell crystallographic representation, along with cell parameters.	41
2.8	X-ray diffractogram of In_2S_3 NR along computed ones for γ -trigonal In_2S_3 . We have firstly simulated NPL with the γ phase (green lines) and the theoretical diffractogram looks in agreement with the experimental one (blue curve), but the orientation needs to be sorted out. We thus generate NPL with a 1, 10, 100 aspect ratios in the three crystallographic orientations. Over those six possibilities, only three yield a different diffraction pattern since the a and b axis are equivalent. For example, the 1x10x100 NPL and the 10x1x100 NPL will yield the same diffraction pattern. These simulations and plots were realized by Benjamin Abécassis.	42
2.9	XPS analyses: (a.) XPS patterns for survey of NR, proving the atomic presence of In(12.2%), S(18.6%), O(0.5%), C(65.9%), N(2.8%) - High-resolution spectra highlighting the presence of: (b.) In in the form of sulfide (peak centred at 444.7-444.9 eV), (c.) S in the form of sulfide (peak centred at 162.5 eV).	44

2.10	UV-visible absorption spectrum of In_2S_3 long NR in cyclohexane. . . .	45
2.11	Shape-control induced by the variation of the quantity of water in the reaction medium: TEM images of In_2S_3 hexagonal nanoplates (a., b.), and of In_2S_3 nanoribbons (c., d.).	45
2.12	TEM images of In_2S_3 hexagonal NPL, obtained when no water is present in the initial reaction mixture.	46
2.13	TEM image of products of syntheses where only the amount of water is varied with respect to the amount of indium (III) chloride. Characteristic dimensions of the various nano-objects obtained in each synthesis are given: below each image is given the measurement of the average apothem for regular hexagons, the average altitude for equilateral triangles or the average dimension of rectangular nanoplates and nanoribbons.	47
2.14	XR diffractograms of products from syntheses of In_2S_3 nanomaterials, where only the amount of water compared to the one of indium(III) chloride is varied.	48
2.15	Experimental setup for the synthesis optimization of NR using a Linkam stage. Left: heating stage - Right: general setup.	49
2.16	TEMPERATURE-DEPENDENCE. TEM images of the products of In_2S_3 NR reaction at different temperatures: (a.) 180°C , (b.) 200°C , (c.) 230°C , (d.) 250°C . The quantity and length of NR increase with the reaction temperature.	50
2.17	CHANGE IN IN:S RATIO. TEM images of the products of NR reaction at different stoichiometric ratios between indium and sulfur : (a.) In:S=1:0.5, (b.) In:S=1:1, (c.) In:S=1:1.5 (usual condition), (d.) In:S=1:3. The quantity and length of NR increase with the ratio In:S.	51
2.18	Time-resolved in situ SAXS/WAXS measurements for the synthesis of hexagonal NPL (top, path (a.) no water added in the reaction mixture) along the data for the synthesis of nanoribbons (bottom, path (b.) in grey, water added in the reaction mixture). In each case, the scattered intensity is plotted in function of the scattering vector for different reaction times, as the reaction temperature is increased. These plots were realized by Laurent Lermusiaux. At the end of each paths (a.) or (b.) is a TEM image of the resulting as-synthesized nano-objects (i.e. respectively flat hexagons, which can stack one upon each other, or nanoribbons).	54
2.19	Mechanism suggested for hexagonal NPL growth after preliminary interpretations of time-resolved in-situ SAXS. 1. First occur the nucleation of small spheres. 2. These spheres interact to form nuclei that stack one upon each other. 3. This lamellar phase could serve as a template to the formation of NPL. Oleylamine molecules are not represented in steps 1 and 2 for clarity reasons.	55
2.20	COLLOIDAL STABILITY OF NR (a.) From left to right, pictures of In_2S_3 NR solutions in: toluene, cyclohexane, cyclohexene, chloroform, cyclooctane, cyclopentane, cyclopentylmethyl ether, THF, cyclohexane with 2-ethylhexylamine (to try to stabilize the solution), toluene with 2-ethylhexylamine, DMSO, DMF, ethanol, acetone, pentane, hexane, diethyl ether, ethyl acetate - (b.) In_2S_3 NR solution in toluene when NR concentration is varied, with dilution factors of 0.1, 1 and 10 from left to right - (c.) In_2S_3 NR solution in THF when NR concentration is varied, with dilution factors of 0.1, 1 and 10 from left to right. . . .	56

2.21	COLLOIDAL SOLUTION OF NR IN APOLAR OR WEAKLY POLAR SOLVENTS. TEM images of the redispersion of a same amount of In ₂ S ₃ NR in a same volume of the following solvents: (a.) toluene, (b.) cyclohexane, (c.) hexane, (d.) chloroform, (e.) cyclopentane, (f.) pentane, (g.) cyclooctane, (h.) diethyl ether, (i.) cyclohexene. Inserts are pictures of the colloidal dispersions. Green boxes indicate solvents that allow a good dispersion of NR, as seen on TEM grids.	58
2.22	COLLOIDAL SOLUTION OF NR IN POLAR SOLVENTS. TEM images of the redispersion of a same amount of In ₂ S ₃ NR in a same volume of the following solvents: (a.) dimethyl sulfoxide (DMSO), (b.) dimethylformamide (DMF), (d.) cyclopentylmethyl ether, (e.) tetrahydrofurane (THF). Inserts are pictures of the colloidal dispersions. Green boxes indicate solvent that allows a good dispersion of NR, as seen on TEM grids. (c.) and (f.) are magnification on a bundle in respectively DMF and diethyl ether. NR are stack together side by side in the direction of their length, forming bundles that can reach several micrometers in length and several hundreds of nanometers in width, according to the solvent of dispersion used.	58
2.23	SAXS/WAXS patterns of a NR dispersion respectively in (a.) non-bundling solvents (THF, cyclohexene) and (b.) bundling solvents (toluene, DMSO, Et ₂ O, DMF). Theses plots were realized by Laurent Lermusiaux.	59
3.1	A. Scheme of the experimental conditions - B. Top: Nanoribbons in the powder form, Bottom: Colloidal solution of nanoribbons dispersed in toluene.	66
3.2	(a.) TEM image of coiled InS NR lying edge-on - (b.) TEM image of coiled InS NR lying flat - (c., d.) HR-STEM images of a coiled InS NR lying edge-on (c.) and flat (d.). Acquired with the help of Benoit Mahler from the ILM Lyon. - (e., f.) TEM images of on-edge coiled NR, illustrating by the violet curve the “in-out” conformation (e.) and the “in-in” conformation (f.).	67
3.3	XR diffractograms of coiled octylamine-capped indium sulfide nanoribbons. Attributed peaks are the ones inherent to InS NR (see next paragraph) and are in agreement with diffraction peaks positions of orthorhombic <i>Pnnm</i> InS crystallographic structure (ICDD card n°01-072-0551).	67
3.4	RBS spectrum for NR: the experimental data are fitted in order to obtain the chemical composition of the sample, written below the spectrum. The spectrum and its interpretation were realized with the help of Bruno Canut from the Institute of Nanotechnologies of Lyon.	68
3.5	XPS analyses: (a.) XPS patterns for survey of NR, proving the atomic presence of In(16.3%), S(14.7%), O(18.9%), C(45.3%), N(4.8%) - High-resolution spectra highlighting the presence of: (b.) In in the form of sulfide and/or oxide ; (c.) O in the form of oxide (~ 50%) and ligand (~ 50%) ; (d.) S mainly in the form of sulfide (peak at 162 eV). Some is founded to be in a sulfate or sulfonate form (< 10%, peak at 169 eV)	69
3.6	TEM images showing blurry areas of unshaped large material along NR that might be attributed to indium oxide. The presence of this material, mainly along NR agglomerates, is highlighted in red in (c.) and (d.).	70

3.7	Elemental mapping of a coiled NR sample by Energy Dispersive X-Ray Spectroscopy (EDX): (a) HAADF-STEM image showing the area of the sample selected for EDX elemental mapping - (b.) Indium and sulfur elemental mapping - (c.) Oxygen mapping. These analyses were conducted by Gilles Patriarche at the Centre de Nanosciences et de Nanotechnologies of Paris-Saclay.	70
3.8	Selected-Area Electron Diffraction (SAED) experiments.	71
3.9	(a.) HAADF-STEM image of a NR lying flat. Insert: Fourier transform of this image that corresponds to the modelled electron diffraction of orthorhombic InS whose indexation is given in red figures - (b.) View of a modelled orthorhombic InS NR along the [010] zone axis. In the model and in the HAADF-STEM images, atoms are aligned in rows, oriented at approximately 45° from the edge (see highlighting). - (c.) Bright-field STEM image of a NR viewed edge-on. Insert: Fourier transform of this image that corresponds to the modelled electron diffraction of orthorhombic InS whose indexation is given in red figures - (d.) View of a modelled orthorhombic InS NR along the [001] zone axis. In the model and in the HAADF-STEM images, atoms are both aligned in rows, oriented at approximately 40° from the edge (see highlighting). - (f.) Scheme of an orthorhombic Pnmn InS conventional cell, from ICDD card n°01-072-0551. STEM images were realized with the help of Benoit Mahler from the ILM Lyon, Marta de Frutos from the LPS Orsay and Gilles Patriarche from C2N Palaiseau.	72
3.10	Conformational control of nanoribbons by ligand exchange. Left: TEM images of coiled octylamine-capped NR viewed lying flat or (insert) on edge - Right: TEM images of uncoiled oleylamine-capped NR viewed lying flat.	74
3.11	(a.), (b.), (c.) TEM image of unfolded oleylamine capped indium sulfide NR lying flat at different magnifications - (d., e., f., g.) HAADF-STEM images of unfolded NR lying flat. The observed folding here is just due to drying effect on TEM grid. The holes observed in the structure of the NR is due to a fast degradation of the ultrathin NR under electron beam. Inserts (f.) is the enlargement of the yellow box of (e.). HAADF-STEM images were realized with the help of Benoit Mahler from the ILM Lyon.	75
3.12	XR diffractograms of: (a.) Coiled octylamine-capped InS nanoribbons - (b.) Uncoiled oleylamine-capped InS nanoribbons. Peak shifting as regards bulk orthorhombic <i>Pnmn</i> InS diffraction peak (ICDD card n°01-072-0551) positions is highlighted by red lines and arrows.	76
3.13	(a., b.) HAADF-STEM images of octylamine-capped coiled InS NR lying on-edge, highlighting the high degree of curvature of these nano-objects. Inserts (b.) is the enlargement of the yellow box of (a.). Acquired with the help of Benoit Mahler from the ILM Lyon. - (c) Screenshot of Kappa plugin interface: in purple is represented the fit curve obtained from an initialization curve created by a point-click method and which follow the observed curve of the NR.	79
3.14	TEM images of indium sulfide NR TEM capped with : (a.) butylamine - (b.) octylamine - (c.) dodecylamine - (d.) tetradecylamine - (e.) hexadecylamine.	79
3.15	TEM images of indium sulfide NR TEM capped with : (a.) butylamine - (b.) dodecylamine - (c.) tetradecylamine - (d.) hexadecylamine - (e.) native-octylamine	80

3.16	TEM image of indium sulfide NR capped with octadecylamine (overall view : (a., b.), twisting : (c.)) and oleylamine (d., e.).	80
3.17	SAXS results : (a.) $I \cdot q^2$ as a function of q , with I the SAXS intensity and q the scattering vector, for amino-ligand capped indium sulfide NR in glass capillaries. This graphic representation allows an enhancement of the variation of intensity with q . Corresponding SAXS pattern is available in Fig S8. (b.) Correlation between the calculated distance in SAXS $2\pi/q_{min}$, with q_{min} the position of the first intensity minima, and the TEM measured curvature radius of amino-ligand capped indium sulfide NR. (c.) SAXS patterns of amino-ligand capped indium sulfide NR in glass capillaries.	82
3.18	(a.) UV-visible absorption spectra of coiled indium sulfide NR and uncoiled indium sulfide NR in cyclohexane - (b.) Picture of octylamine-capped coiled indium sulfide NR powder - (c.) Picture of oleylamine-capped uncoiled indium sulfide NR powder.	82
3.19	Circular Dichroism spectrum of L- or D-penicillamine (Pen) functionalized indium sulfide NR	85
3.20	TEM images of nano-objects obtained following the protocol of synthesis of coiled indium sulfide NR, by replacing sulfur powder by (a.) 1-(4-trifluorophenyl)-3-phenylthiourea and (b.) 1-hexyl-3-dodecylthiourea.	87
4.1	(a.) Scheme of the experimental procedure to synthesize 4ML-CdSe NPL - (b.) Picture of the corresponding experimental setup.	92
4.2	(a.) TEM image of 4ML-CdSe NPL synthesized according to the protocol described in the experimental section. The insert is a schematic representation of the atomic arrangement inside a NPL, highlighting the different ML and the capping ligands (not at scale) - (b.) UV-visible absorption spectra of these 4ML-CdSe NPL with a characteristic feature at 510 nm - (c., d.) Pictures of 4ML-CdSe solution in hexane under visible light (c.) and illumination under UV light, showing the light green fluorescence of the NPL (d.).	93
4.3	TEM images of 4ML-CdSe NPL synthesized with the injection of: (a.) 1 equivalent or (b.) 0.6 equivalent of cadmium acetate as regards the equivalent of cadmium myristate. The former case gives rise to square NPL, the latter to rectangular NPL.	94
4.4	TEM IMAGES OF 4ML-CdSe NPL ASSEMBLIES. (a., b.) Assemblies obtained after evaporation of a hexane solution of 4ML-CdSe NPL containing 0.02M of oleic acid. The assemblies get an average length of (565 ± 49) nm and could reach the micrometer. The insert is a TEM image of the 4ML-CdSe NPL used for the assembly, that get lateral dimensions of (31.8 ± 0.6) nm \times (12.9 ± 0.5) nm, that is to say an aspect ratio of 2.5. - (c.) Assemblies of 4ML-CdSe NPL obtained without any evaporation of the system, of an average length of (258 ± 22) nm. This length is similar to the one obtained with a same sample subjected to evaporation ((222 ± 19) nm). The NPL get an aspect ratio of 3.4 as they are (37 ± 1) nm long and (10.9 ± 0.6) nm wide. - (d., e.) Magnification on 4ML-CdSe assemblies, showing the strong distortion occurring inside assemblies, leading to a horseshoe (d.) or a bow-tie (e.) shape.	95

4.5	(a., b.) HAADF-STEM images of 4ML-CdSe NPL before any assembly process. Some NPL are already strongly twisted in the sample - (c., d.) HAADF-STEM images of distorted 4ML-CdSe NPL within an assembly. These images were acquired with the help of Marta de Frutos from the Laboratoire de Physique des Solides in Orsay.	95
4.6	Scheme of the experimental procedure to synthesize 5ML-CdSe NPL. .	97
4.7	(a.) TEM image of 5ML-CdSe NPL synthesized according to the protocol described in the experimental section. - (b.) UV-visible absorption spectra of these 5ML-CdSe NPL with a characteristic feature at 550 nm - (c., d.) Pictures of 5ML-CdSe solution in hexane under visible light (c.) and illumination under UV (d.), showing the green fluorescence of the NPL.	97
4.8	TEM IMAGES OF 5ML-CdSe NPL ASSEMBLIES AT DIFFERENT MAGNIFICATIONS. (a., b.) Assemblies obtained after evaporation of a same NPL dispersion in an oleic acid solution in hexane of (a.) 0.036 M and (b.) 0.8 M - (e., f.) Two kinds of assemblies respectively (e.) straight (obtained after evaporation, [OA] = 0.018M) and twisted (no evaporation, [OA] = 0.025 M). Details of these straight or twisted assemblies are given respectively in inserts (c.) and (d.).	98
4.9	FLUORESCENCE MICROSCOPY: Images of three platelets chains (a.) under wide field excitation and (b.) excited locally by a laser spot - (c.) Schematic of the proposed FRET migration mechanism. These optical measurements were realized by Jiawen Liu and Laurent Coolen from the INSP.	101
4.10	Decay curves of single platelets (red) and stacked NPLs (blue). The grey dashed line indicates the instrument response function. These optical measurements were realized by Jiawen Liu and Laurent Coolen.	103

LIST OF FIGURES

List of Tables

2.1	Average measured dimensions of In_2S_3 as a function of the reaction temperature.	49
2.2	TEM measurements on bundles of NR in various solvents.	57
3.1	Shifts of diffraction peaks between coiled octylamine-capped NR and uncoiled oleylamine-capped NR.	77
3.2	Average curvature radius according to the length of the carbon chain of the amino-ligand exchanged with native octylamine.	79
4.1	CADMIUM ACETATE: Average lateral dimensions of 4ML-CdSe NPL synthesized with a varied amount of cadmium acetate injected, expressed in equivalents (eq) of $\text{Cd}(\text{myr})_2$	93
4.2	OLEIC ACID CONCENTRATION: Average length of 4ML-CdSe NPL assemblies for different oleic acid concentrations.	96
4.3	OLEIC ACID CONCENTRATION: Average length of 5ML-CdSe NPL assemblies for different oleic acid concentrations.	99

Nomenclature

0, 1, 2, 3D : 0, 1, 2, 3 dimensions

AO : Atomic Orbitals

CD : Circular Dichroism

DFT : Density Functional Theory

DFT : Density-Functionnal Theory

DLVO theory : Derjaguin-Landau-Verwey-Overbeek theory

DMF : Dimethylformamide

DMSO : Dimethyl sulfoxide

ED : Electron Diffraction

FRET : Förster Resonance Energy Transfer

HAADF-STEM : High-Angle Annular Dark-Field - Scanning Transmission Electron
Microscopy

LED : Light-Emitting Diode

ML : Monolayers

MO : Molecular Orbitals

NC : Nanocrystals

NPL : Nanoplatelets

NR : Nanoribbons

NS : Nanosheets

OA : Oleic Acid

ODE : 1-octadecene

PL : Photoluminescence

QB : Quantum Belts

QD : Quantum Dots

RBS : Rutherford Backscattering Spectrometry

NOMENCLATURE

SAXS : Small-Angle X-ray Scattering

STEM : Scanning Transmission Electron Microscopy

TEM : Transmission Electron Microscopy

THF : Tetrahydrofurane

UV-vis : Ultraviolet-visible (spectroscopy)

WAXS : Wide-Angle X-ray Scattering

XPS : X-Ray Photoelectron Spectroscopy

XR : X-Rays

XRD : X-Ray Diffraction